Chapter 9

Numerical Study on the 3–1 Spheroid

The preliminary part of this chapter discusses the: solver, turbulence models, model geometry, mesh structure, and grid density. Section 9.1 explains a number of user defined functions (UDF) and some other software. One of these UDFs overcomes a perceived problem with the calculation of the distance between wall surfaces and the cell centre; two others are used to implement laminar regions for two turbulence models. Software was also written to allow boundary layer properties to be calculated external to the finite volume code but using its results; this code is discussed in this section. The following three sections examine the results from the computations and compare them to the previously obtained experimental data. Section 9.2 examines the results for the 3–1 spheroid at an incidence of $-0.2°$ for two Reynolds numbers and details some difficulties that arise with the implementation of the laminar regions. In Sections 9.3 and 9.4 the numerical and measured results are compared for the spheroid at an incidence of $-10.2°$ with and without the trip strip respectively.

The measurements presented in the preceding chapters show that for the range of Reynolds numbers tested the boundary layer exhibits significant regions of both laminar and turbulent flow with a relatively short transitional region between them. The turbulence models in common use do not model the physical phenomena that are present in the boundary layer transition process. For the simple case of a smooth flat plate at zero incidence in a low turbulence environment this process is complicated. White [87] summarises the stages between laminar and turbulent boundary layers as: the amplification of small disturbances into unstable two-dimensional Tollmein-Schlichting waves; the development of these into three-dimensional waves and hairpin eddies; localised vortex breakdown; three-dimensional fluctuations formed

by cascading vortex breakdown; formation of turbulent spots. The importance of the scale [88] and frequency [89] of turbulent structures has long been recognised as playing an important role in boundary layer transition, so it will be difficult for any model that does not account for these to predict boundary layer transition accurately.

Arguably the most successful technique for modelling boundary layer transition has been based on the amplification of disturbances in the boundary layer. This e^n method has been used by Cebeci to calculate the location of transition on a 6–1 spheroid at a incidences of 10° [42] and incorporated into the widely used X-foil isolated aerofoil code [90]. Stock [91] has successfully used the e^n method to predict the transition on a 6–1 spheroid at incidences between 0° and 30°. While the local correlation-based transition model of Menter et al. [92] and Langtry et al. [93] has been introduced into the commercial CFD code CFX, this technique does not attempt to model the actual physics of boundary layer transition.

The goal of this numerical study however is not to examine the techniques of predicting transition. This study examines how well the flow around the body is modelled if the experimentally obtained transition locations are used to activate the turbulence models in the locations where the boundary layer is measured as turbulent. The results with these measured laminar and turbulent regions implemented are then compared with experimental data detailed in the earlier chapters.

The commercial CFD code Fluent 6.2 was used to model these tests. The Fluent preprocessor Gambit was used to create the mesh. The spheroid, sting, foil support and upper limb of the tunnel were modelled using a hybrid mesh with a predominance of hexahedral elements. The volume close to wall faces was meshed with hexahedral elements. The spheroid, sting and foil support were surrounded with an offset volume that allowed fine control of the hexahedral element skewness and grading (Fig. 9.1). An O-type grid exists around the combined spheroid, sting and foil support; this in effect results in a C-type grid around the spheroid and sting which are of primary interest. The adjacent offset volumes allowed elements of high quality to be produced in regions were the fluid was subject to large gradients. The normal distance from the wall of the first element was selected to give $y^+ < 1$ for the spheroid, sting and foil at the maximum $Re_l = 4.0 \times 10^6$. y^+ values between 30 and 80 were used for the cells adjacent to the tunnel walls at the maximum Reynolds Number. The grading normal to the wall was generally 1.12 or less. Tetrahedral elements were used to link the offset volume and the hexahedral elements used in the majority of the upper limb including the test section. A symmetry plane was used on the vertical x-z plane for the majority of the numerical studies.

Table 9.1 details the grid resolution of a number of meshes used to examine the grid sensitivity of the calculations on the spheroid. This table also displays calculated loads that are

grid name	normal intervals	azimuthal intervals[a]	longitudinal intervals		C_D [b]	C_L [b]	C_M [b]
			front half	rear half			
Sph_Grid-10A	56	54	54	48	0.0601	0.0951	0.1341
Sph_Grid-10B	70	70	79	100	0.0594	0.0949	0.1343
Sph_Grid-10C	56	54	54	146	0.0593	0.0953	0.1340
Sph_Grid-10D	84	70	86	200	0.0597	0.0943	0.1342
Sph_Grid-10C-Adapt	112	108	108	292	0.0597	0.0968	0.1338
Sph_Grid-10B[c]	70	70	79	84	0.0609	0.0942	0.1343
Sph_Grid-10B-Gap	70	70	79	84	0.0608	0.0936	0.1345

[a] These intervals distributed over $180°$.

[b] Force and moments calculated over $360°$.

[c] The intervals and loads reported are from *Sph_Grid-10B*. This grid has no spheroid-sting gap; however, the surface region over which these values have been determined in this row is restricted so it excludes the region where the spheroid-sting gap exists in *Sph_Grid-10B-Gap*. This allows comparison between the results of *Sph_Grid-10B* and *Sph_Grid-10B-Gap* in order to determine the influence of this gap on the calculated loads.

Table 9.1: Grid resolution on and normal to spheroid surface and loads calculated using realisable k-ε turbulence model for 3–1 spheroid at 10° incidence with $Re_l = 4.0 \times 10^6$.

one part-measure of the grid sensitivity. The grid sensitivity was checked at the maximum Reynolds number under examination ($Re_l = 4.0 \times 10^6$) at the maximum incidence of 10° with the realisable k-ε turbulence model. The minimal difference in the calculated loads between the two lowest density meshes *Sph_Grid-10A* and *Sph_Grid-10B* suggest that these results are independent of the mesh density for the case under test. This is confirmed by the higher density meshes and by the consistent ratio of form to viscous drag across all grids.

The negligible impact of the $0.5\,mm$ gap between spheroid and sting, along with the associated internal volume, is demonstrated by the minimal change in loads between the results of *Sph_Grid-10B* and *Sph_Grid-10B-Gap*, where the loads calculated from *Sph_Grid-10B* are restricted to exclude the surface of the spheroid were the spheroid-sting gap exists in *Sph_Grid-10B-Gap* (last two entries in Table 9.1). This small change in loads is reasonable as the entire spheroid-sting gap is in a single region of separated flow. The slight increase in drag resulting from the inclusion of the spheroid-sting gap is consistent with the increased surface area at the rear of the model in a region of positive pressure. The extra resolution provided by *Sph_Grid-10C*, *Sph_Grid-10C-Adapt* and *Sph_Grid-10D* is of relevance when computing the flow with areas of laminar and turbulent boundary layer when laminar separation (and turbulent reattachment) occurs; as discussed in the follow subsections.

The three-dimensional incompressible formulation of the Reynolds-Averaged Navier-Stokes

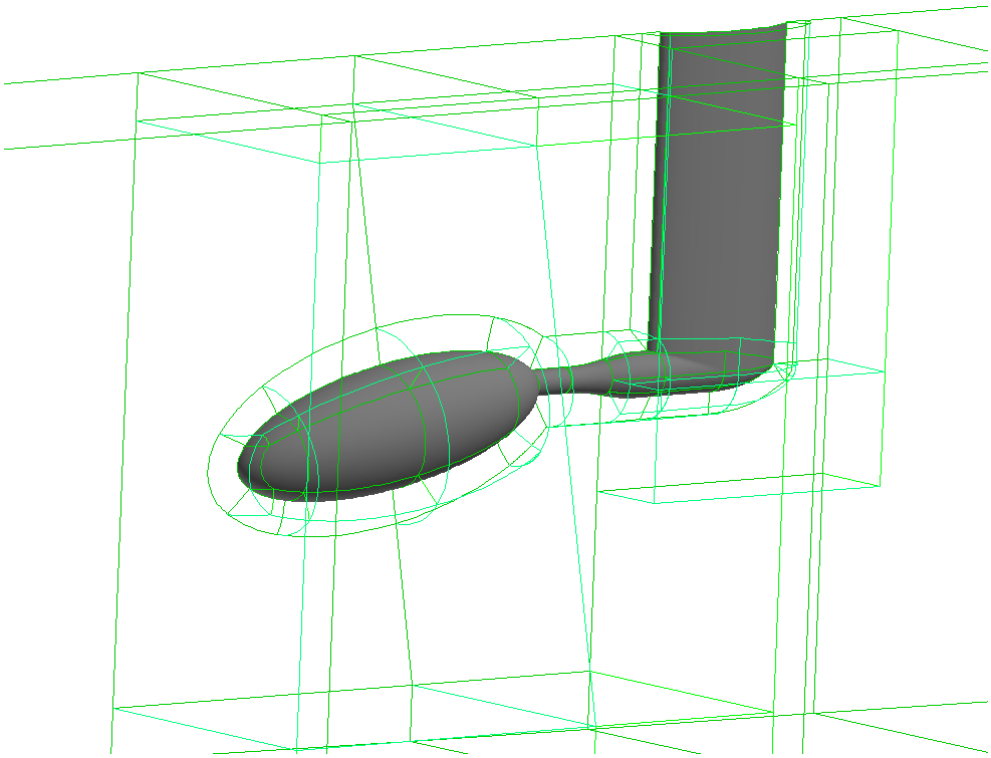

Figure 9.1: Volume geometry for spheroid at $\alpha = -10.2°$. Hexahedral cells are used near the surfaces and in the majority of test section. Tetrahedral cells are used to create a conformal mesh between the offset volumes and the hexahedral cells in the test section.

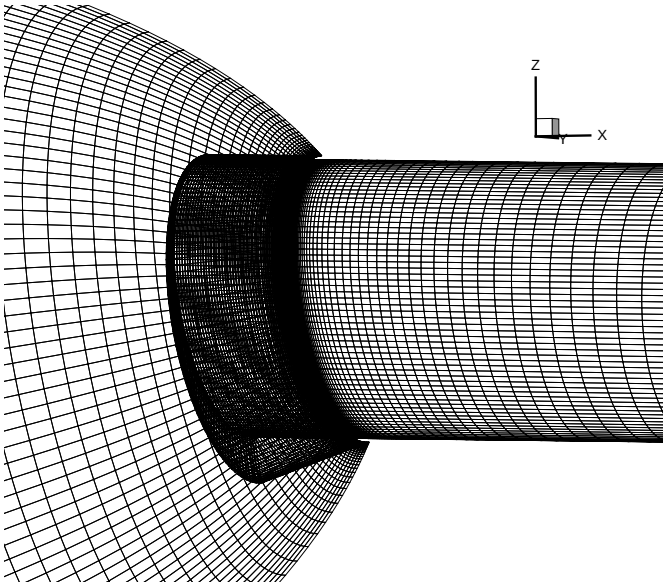

Figure 9.2: Surface mesh around the rear of the spheroid showing spheroid-sting gap, *Sph_Grid-10B-Gap*, $\alpha = -10.2°$.

(RANS) equations were solved with the segregated solver. Second-order discretisation was selected for the continuity, momentum and turbulent variables. The SIMPLE algorithm was used for pressure-velocity coupling. Gradient evaluation was performed with a cell-based method.

The enhanced wall function uses a two layer approach with a blending function. If y^+ for the cell nearest the wall is low enough to be inside the (linear) viscous sublayer, the flow is modelled to the wall; if y^+ for the cell places it in the log-law region, wall functions are used. A blending function provides a smooth transition for the calculations when the height of the cell adjacent to the wall is such that it is too great to fall within the viscous sublayer but too short for the law of the wall to be applicable. The enhanced wall treatment was used for these computations, as it allows for modelling to the wall on the spheroid, sting and support foil. The more economical wall functions were used on the walls of the upper limb.

The realisable k-ε model was selected, as it is reported to be the most suitable of the k-ε turbulence models for handling streamline curvature, separation and vorticity [94][95]. An added advantage of this model is it has no singularity in the ε equation if k is zero. Given the positive performance of the low Reynolds number k-ω model reported by Kim et al. [48] this was trialled, but produced non-physical results in the stagnation pressure. This problem appeared to be related to the freestream turbulence and was apparent even if the freestream turbulent intensity was approximately 0.1% in the test section; the results are not presented for this model. The results of the Fluent implementation of the SST model are also compared with experiment: this model blends (with the function *F1*) the k-ε and k-ω model with the later of these operating in the low Reynolds number region of the flow. The developer of the SST model tested it in adverse pressure gradients [96] and reported favourable performance in predicting separation.

If a small turbulent length scale was selected at the inlet the turbulence intensity decreased rapidly downstream of the inlet. However, if the length scale was set large enough so that the turbulent kinetic energy did not dissipate rapidly, the resulting turbulent viscosity ratio was outside the range generally used for external flows (1-10). Fortunately the calculated loads and flow close to the body using the realisable k-ε and the SST turbulence model displayed little sensitivity to the range of length scales required to vary the turbulent intensity in the test section between 0.1% and 0.6%. (The lift showed the greatest variation of approximately 3%.) Thus it is possible to use a turbulent viscosity ratio of 10 with minimal change in the calculated results. It was also noted with the SST turbulence model that if larger length scales were used the *F1* blending function would activate the k-ω portion of the model too far into the freestream. It is physically reasonable that the length scale suitable for modelling the flow in the upper limb of the cavitation tunnel should be much larger than the one used to model

the flow around the body in the test section.

9.1 User defined functions and other code

The Fluent code allows a large degree of flexibility via the implementation of UDFs. A number of UDFs were created for use with the numerical studies of flow about the spheroid. The reason for, and details of these UDFs are discussed with reference to the numerical studies performed on the spheroid and ellipsoid.

9.1.1 UDF - Cell Wall Distance

Examination of initial results showed unusual y^+ and wall shear stress values on the surface of the spheroid (Fig. 9.3). These results show grid sensitivity when the cell closest to the wall was thin in order to obtain a low y^+; it was not apparent on the tunnel walls. This sensitivity was traced to the dependency of these functions on the cell wall distance. The cell wall distance is defined as "the normal distance of each cell centroid from the wall boundaries". The mesh for the spheroid was created in Gambit with the height of the first cell layer set to $2.25\,\mu m$ so the height of the centroid is expected to be close to half this value. Fluent however showed the height for the cell wall distance over the front half of the spheroid varying between 1.1×10^{-10} and $6.5 \times 10^{-6}\,m$ (Fig. 9.4(a)). Discussions with the code manufacturer failed to provide a satisfactory explanation (as far as this user was concerned) so a UDF was written to calculate the distance from the cell centroid to the nearest wall (Fig. 9.4(b)). With the cell wall calculated using this UDF the y^+ and wall stress values on the surface of the spheroid no longer display grid sensitivity (Fig. 9.5). The equiangle skew of the cells near the region showing grid sensitivity is up to almost 0.7 in a few cells (Fig. 9.6(a)); however, the areas where unusual cell wall distances were calculated extends significantly beyond these regions. The angle of the faces of a hexahedral cell is ideally perpendicular to their connecting faces. Fig. 9.6(b) shows the maximum deviation from this ideal angle is less than 13° for all faces adjacent to the surface faces over the front of the spheroid.

An alternative method for calculating the cell wall distance was later found on the Fluent web site that produced almost identical results (Fig. 9.7(a)) to the cell wall distance UDF. This alternative Fluent method was used for the CFD on the spheroid due to its greater efficiency and general availability. When Version 6.3 of Fluent was released this alternative method no longer behaved as it did in Version 6.2 (Fig. 9.7(a)), so the studies on the ellipsoid were performed using the earlier developed UDF. The results of the cell wall calculations for the ellipsoid using the default Fluent method and the UDF are shown in Fig. 9.8. The standard methods of calculating the cell wall distance in Fluent Version 6.2 and 6.3 produced almost

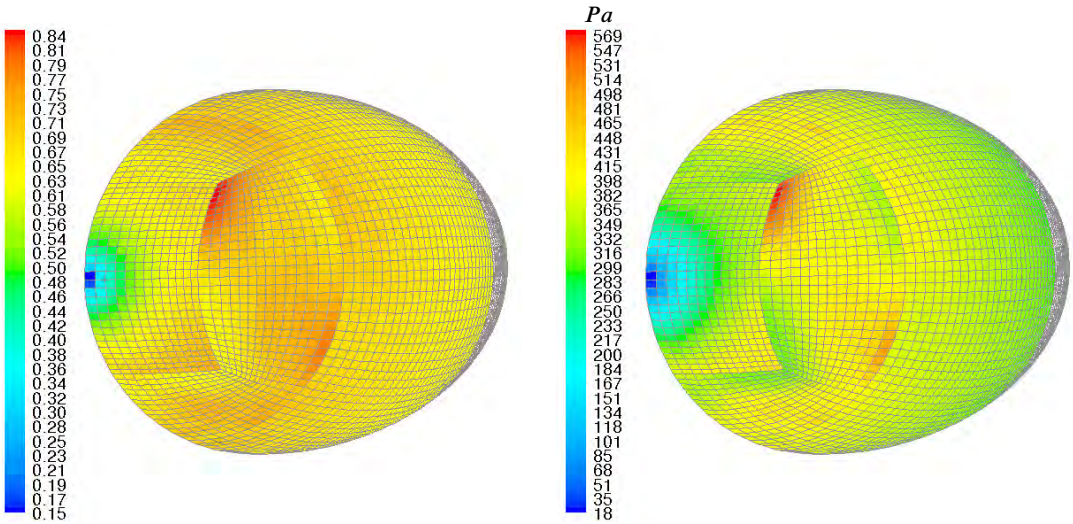

(a) y^+ (b) wall shear stress (Pa)

Figure 9.3: Sensitivity of y^+ and wall shear stress to grid with the default method of calculating the distance between the cell centroid and the nearest wall. $\alpha = -0.2°$, $Re_l = 4.0 \times 10^6$, *Sph_Grid-A*

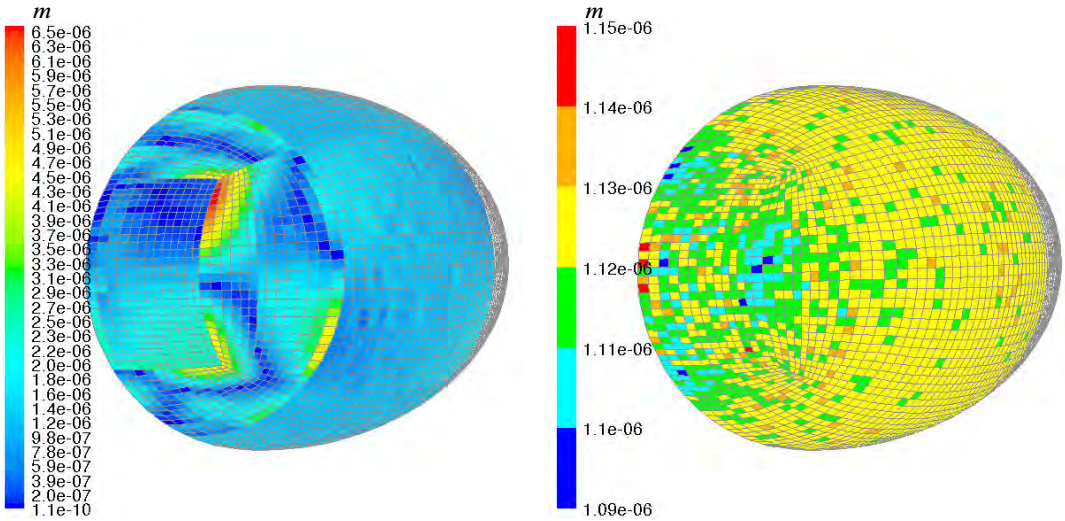

(a) Default Fluent method (b) UDF

Figure 9.4: Comparison of distance between centroid of cell adjacent to the wall and the wall surface calculated using the default methods and the developed UDF. $\alpha = -0.2°$, *Sph_Grid-A*

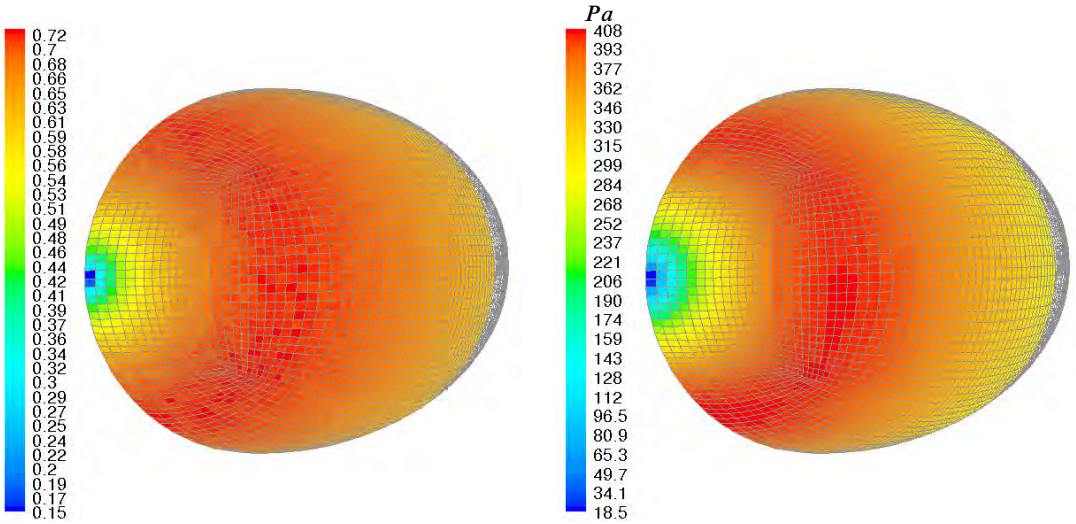

(a) y^+ (b) wall shear stress (Pa)

Figure 9.5: Sensitivity of y^+ and wall shear stress to grid with the developed UDF method for calculating the distance between the cell centroid and the nearest wall. $\alpha = -0.2°$, $Re_l = 4.0 \times 10^6$, *Sph_Grid-A*

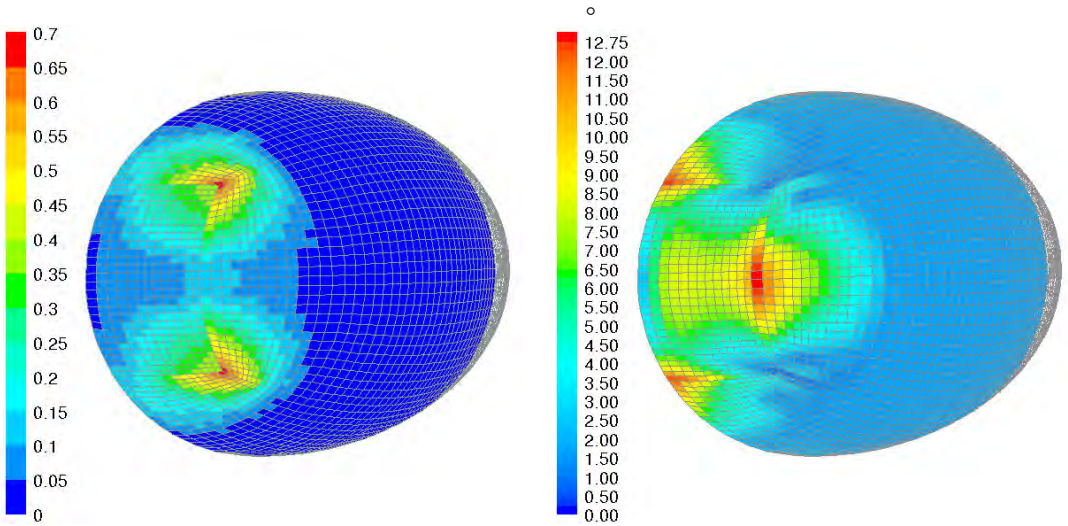

(a) Cell equiangle skew (b) Maximum deviation of cell sides from perpendicular to spheroid surface, (°)

Figure 9.6: Cell quality, $\alpha = -0.2°$, *Sph_Grid-A*

identical results. The results for the ellipsoid model without a symmetry plane with the default Fluent method and the UDF calculation of the cell wall distance is shown in Fig. 9.8. The mesh for the ellipsoid without the symmetry plane was created by reflecting the mesh about the symmetry plane in Gambit, so it is worth noting the lack of symmetry about this plane shown in Fig. 9.8.

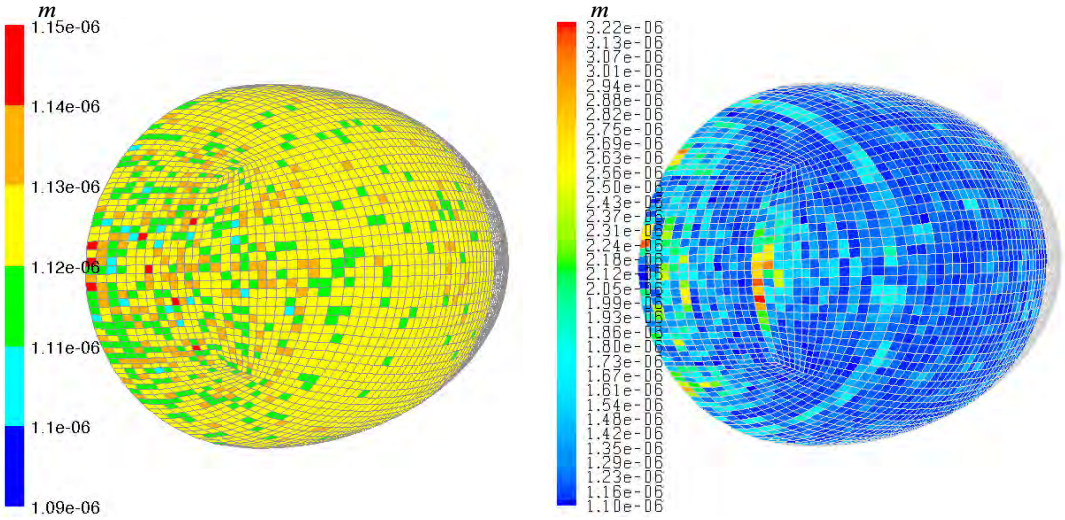

(a) Version 6.2 (b) Version 6.3

Figure 9.7: Distance from centroid of cell adjacent to the wall to the closest wall surface calculated using the alternative Fluent method. $\alpha = -0.2°$, *Sph_Grid-A*

It is important to stress that the calculated forces and flow field showed negligible difference except for those properties directly dependent on the cell wall distance. However, given the focus of this work on implementing regions with boundary layer transition where a sudden increase in wall shear stress is expected, it is undesirable to have sudden jumps in this property due to the calculation of mesh properties.

9.1.2 UDF - Laminar Zones

UDFs were written to allow the flow in a cell to be designated as laminar, turbulent or transitional via a value in a User Defined Memory (UDM) being set to zero, unity or between respectively. The UDM provides a location to store a value associated with each cell or face in the mesh. The laminar or transitional regions were created by multiplying the turbulent viscosity, μ_t, via the value in the designated UDM. To allow this to occur the equations for the turbulent viscosity for the realizable k-ε and the SST turbulence models were coded in separate UDF functions and multiplied by the UDM with the set intermittency value. The equations and constants used to calculate the turbulent viscosity are specified in the Fluent User Manual [94] with the following clarifications. The nomenclature in this section closely follows that of

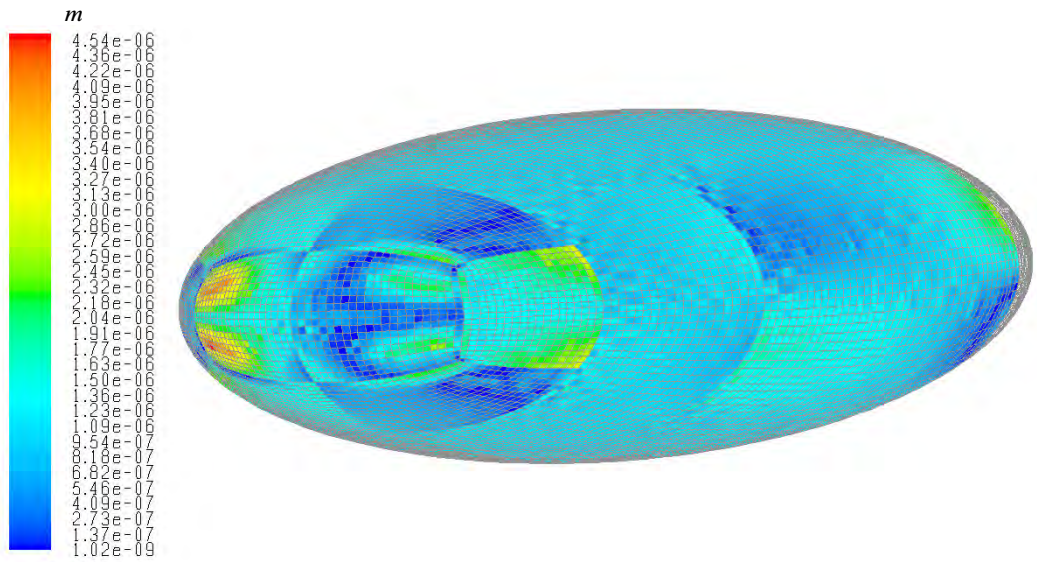

(a) Default cell wall calculation, Version 6.3

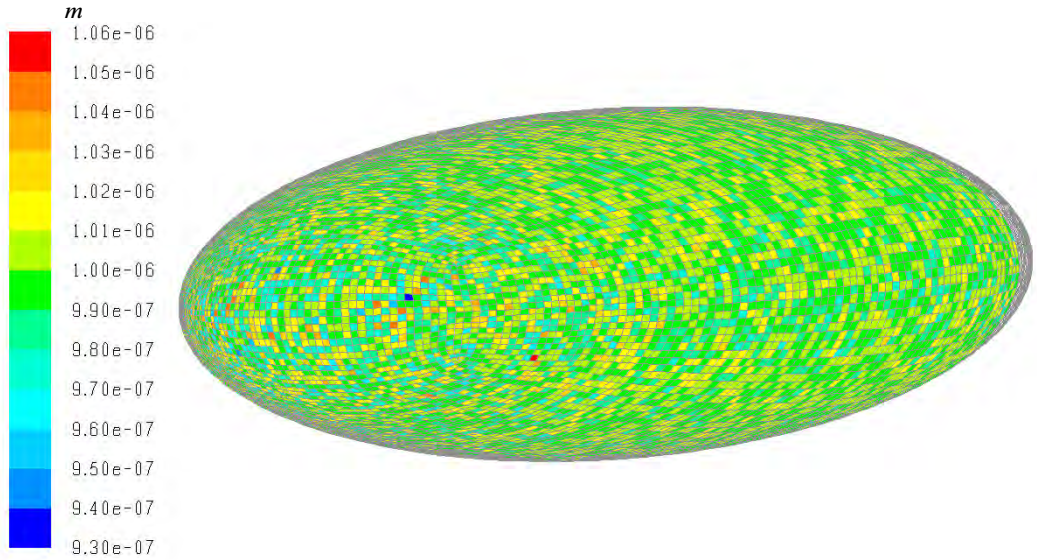

(b) UDF cell wall calculation, Version 6.3

Figure 9.8: Comparison of distance between centroid of cell adjacent to the wall and the wall surface calculated using the default method and the developed UDF for the 4.2–2–1 ellipsoid at $\alpha = -10.2°$. The mesh on the far side of the vertical symmetry plane was created using a reflection.

the Fluent User Manual.

- The enhanced wall treatment's two layer model uses a blending function when calculating the turbulent viscosity, $\mu_{t,enh}$, between the fully turbulent region and viscosity-affected region near the wall. The turbulent viscosity in the near wall region, $\mu_{t,2layer}$, is blended with the turbulent viscosity in the fully turbulent region resulting in

$$\mu_{t,enh} = \lambda_e \, \mu_t + (1 - \lambda_e) \, \mu_{t,2layer} \tag{9.1}$$

The blending function, λ_e is given by

$$\lambda_e = \frac{1}{2}\left[1 + tanh\left(\frac{Re_y - Re_y^*}{A_{blend}}\right)\right] \tag{9.2}$$

where Re_y is the turbulent Reynolds number, $Re_y^*(= 200)$ determines the centre of the blend, and A_{blend} is a constant that determines the sharpness of the blend. Re_y is determined from

$$Re_y = \frac{\rho \, y_P \sqrt{k}}{\mu} \tag{9.3}$$

where y_P is the distance from the nearest wall, k is the turbulent kinetic energy, and μ is the molecular viscosity. The Fluent manual provides

$$A_{blend} = \frac{|\Delta Re_y|}{tanh(0.98)} \tag{9.4}$$

where $|\Delta Re_y|$ is a constant used to determine A_{blend}. However the text states that "the value λ_e will be within 1% of its far field value given a variation of $|\Delta Re_y|$ "(from Re_y^*); this is only the case if

$$A_{blend} = \frac{|\Delta Re_y|}{tanh^{-1}(0.98)} \tag{9.5}$$

The original work on this blending by Jongen [97][98] does not extend to either Eq. 9.4 or 9.5.

Given that the purpose of this blending function is to facilitate convergence, this error is of negligible physical significance. The value for ΔRe_y is not specifically stated, but given as a range between 5% and 20% of Re_y^*. In the UDF a value of ΔRe_y of 13 is chosen if Eq. 9.4 is used, which equates to 39.7 if using Eq. 9.5, both within the range of 5% to 20% of Re_y^*.

- The calculation of the μ_t for the SST turbulence model in Fluent changed between Version

6.1 and 6.2 of Fluent. Version 6.1 uses

$$\mu_t = \frac{\rho\, k}{\omega} \frac{1}{max\left[\frac{1}{\alpha^*}, \frac{\Omega\, F_2}{a_1 \omega}\right]} \tag{9.6}$$

where ω is the specific dissipation rate of k; α^* is a low Reynolds number correction that is not used (set to 1) with this UDF nor is it part of the original Menter SST model [96]. Wilcox [49] provides an in depth development of this low Reynolds number correction. F_2 is a second blending function of the SST turbulence model, and Ω is the absolute value of the vorticity. $a1$ is a constant set to 0.31. Version 6.2 substitutes the modulus of the mean rate-of-strain tensor, S, for Ω:

$$\mu_t = \frac{\rho\, k}{\omega} \frac{1}{max\left[\frac{1}{\alpha^*}, \frac{S\, F_2}{a_1 \omega}\right]} \tag{9.7}$$

The UDF used to calculate μ_t for the SST turbulence model follows the formulation in Eq. 9.7.

Menter et al. [92] when implementing their transition model modify the F1 blending function of the SST turbulence model to prevent the k-ε model activating in low Reynolds number transitional or laminar regions. This modification to the blending function could not be implemented; however, the F1 blending function was monitored and not seen to activate the k-ε model in these low Reynolds number regions. Laminar zones are created in this UDF by setting the turbulent viscosity to zero, rather than using the technique of Menter et al. [92] where turbulence production is set to zero. This means that only in transitional regions should the concern with the F1 blending function be of significance. (The technique of setting the production to zero in laminar zones is preferable as it does not result in the loss of the turbulent kinetic energy entering the laminar region, and is of importance if a turbulent wake is impinging on a boundary layer of interest; but it is more difficult to implement via UDF.)

Fluent does allow individual zones to be set as laminar using the technique of setting the turbulent viscosity to zero. This has the advantage of not having to write the above code, but has the disadvantages that no boundary layer transition region is possible, and the pre/post processing is more difficult with the additional zones that change with each incidence and Reynolds number. This UDF also has the possibility of allowing the region of turbulent flow to move forward if a separation is detected upstream of the predetermined transition region, and allowing the region of turbulent flow to be adjusted with time in an unsteady simulation.

9.1.3 Calculation of Boundary Layer Properties

The boundary layer properties: displacement thickness (δ^*), momentum thickness (θ), and shape factor (H) are used extensively in the analysis of two-dimensional boundary layer behaviour. These properties are not generally available from CFD codes using a volume mesh.

The calculation of displacement thickness in three-dimensional boundary layers is examined by Lighthill [99] using four different methods. In two-dimensional flow the flow reduction method is the most commonly recognised method. In three-dimensions Lighthill considers the flow between two streamlines a distance $h_{y_\Lambda}\, dy_\Lambda$ apart in an orthogonal coordinate system with x_Λ aligned with the external streamline, z_Λ normal to the surface and y_Λ in the crossflow direction. $h_{x_\Lambda}\, dx_\Lambda$ is the distance between a point at x_Λ and $x_\Lambda + dx_\Lambda$. For the flow reduction method in three-dimensions, Eq.19 of Lighthill [99] gives the displacement thickness as

$$\begin{aligned}\delta^* &= \frac{1}{U_\Lambda}\int_0^\infty \left(U_\Lambda - u_\Lambda\right) dz - \frac{1}{U_\Lambda h_{y_\Lambda}}\frac{\partial}{\partial y_\Lambda}\int_0^x h_{x_\Lambda}\, dx_\Lambda \int_0^\infty v_\Lambda\, dz_\Lambda \\ &= \delta^*_{x_\Lambda} + \delta^*_{y_\Lambda}\end{aligned} \tag{9.8}$$

where U_Λ is the velocity along the streamline at the edge of the boundary layer; u_Λ and v_Λ are the velocity components in the x_Λ and y_Λ directions respectively. The first term in Eq. 9.8, $\delta^*_{x_\Lambda}$, accounts for the displacement thickness in the direction of flow parallel to the flow at the boundary layer edge, consequently called the streamwise displacement thickness. The second term, $\delta^*_{y_\Lambda}$, calculates the accumulation or dispersion of fluid due to flow in the y_Λ direction for a volume bounded in the streamwise direction by two streamlines a distance $h_{y_\Lambda}\, dy_\Lambda$ apart at the boundary layer edge and another two lines formed by projecting these lines onto the surface in the direction normal to the surface. These streamlines extend upstream to the stagnation point, $x_\Lambda = 0$. This second term is consequently called the crossflow displacement thickness.

Three variations to the three-dimensional flow reduction method presented by Lighthill were used in the present study:

- As the inviscid velocity was available across the boundary layer the difference between the component of the inviscid and viscous velocity in the direction of the viscous flow at the boundary layer edge was used. This should more accurately capture the influence of viscosity on the boundary layer than using the velocity at the boundary layer edge as it will account for any variation in inviscid velocity due to surface curvature.

- The integration of the crosswise velocity component, v_Λ, normal to the surface in the equation presented by Lighthill [99] does not allow for v_Λ being a function of x_Λ. The software described allows for v_Λ being a function of x_Λ by using Eq. 9.9, which is consistent

with Lighthill's description and his Eq.21.

- The integration in the direction normal to the surface was limited to the edge of the boundary layer as determined from the location where the velocity is 99% of the inviscid velocity.

$$\delta^* = \frac{1}{U_\Lambda}\int_0^\infty \left(U_\Lambda - u_\Lambda\right) dz - \frac{1}{U_\Lambda h_{y_\Lambda}}\frac{\partial}{\partial y_\Lambda}\int_0^x \int_0^\infty h_{x_\Lambda} v_\Lambda \, dz_\Lambda \, dx_\Lambda \tag{9.9}$$

The software to calculate the displacement thickness was run separately from Fluent. It reads the Fluent case file and recreates the nodes, faces and cells. The reconstructed faces are quadrilateral hyperboloidal elements as described by Morino et al. [100]. Velocities from a viscous (either laminar or turbulent) and an inviscid solution are read for each node.

At each wall face where it is desired to calculate the streamwise displacement thickness, a normal to the surface is calculated. At each intersection of this normal with a face of the volume mesh, the inviscid and viscous velocity is calculated by interpolating on the face using the values at its four nodes. This normal to the surface is extended out to well beyond the expected edge of the boundary layer. The edge of the boundary layer is determined from where the viscous velocity is 99% of the inviscid velocity. The value for the inviscid velocity is adjusted marginally ($\approx 1.4\%$ at $Re_l = 2.0 \times 10^6$) to allow for the difference in velocity at the centre of the test section due to boundary layer growth on the walls of the tunnel's upper limb.

For a curved surface these surface normals are not parallel. The normal to the wall face, and normal of the adjacent wall faces, are used along with the dimensions of the wall face to determine the effective curvature of the face. This effective curvature can be used to calculate the volume between the normal projection of this face from the surface at distances z_Λ and $z_\Lambda + dz_\Lambda$. The faces on the surface of the spheroid and ellipsoid are doubly curved. This change in volume of a fixed height cell formed by the projection of the wall face from z_Λ and $z_\Lambda + dz_\Lambda$ must be accounted for twice when determining the boundary layer properties: initially when calculating the integral of the difference between the inviscid and viscous values normal to the face, and again when determining the equivalent height of the calculated deficit.

The use of the total pressure to determine the edge of the boundary layer was also investigated. This was unreliable as the total pressure was found to vary across the interface of the hexahedral and tetrahedral cells in some locations by more than 2%.

The crossflow displacement thickness accounts for the accumulation or dispersion of fluid due to gradients in the crossflow along a plane normal to the surface and parallel to a streamline from the edge of the boundary layer above the point of interest to the attachment point. In these calculations the accumulation or dispersion of fluid due to crossflow is determined from

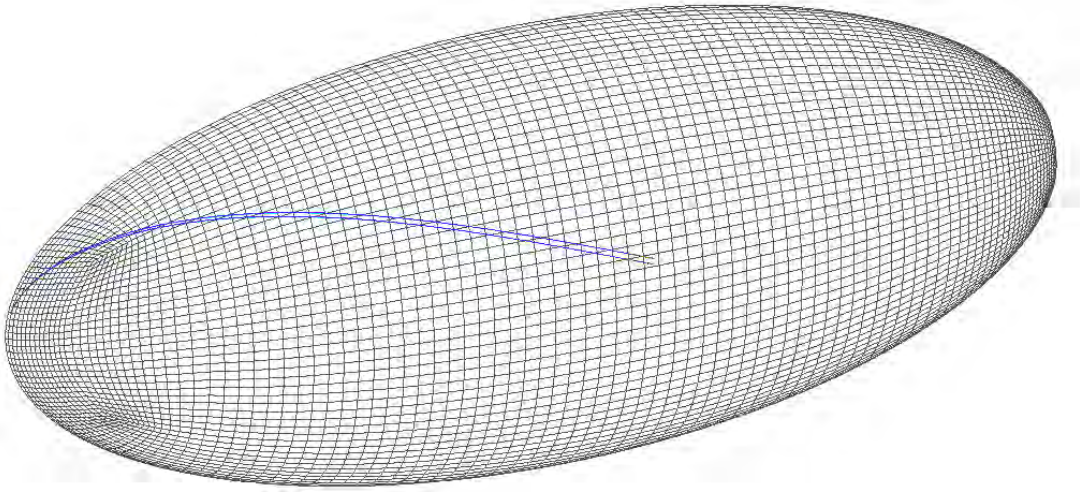

(a) Streamlines for Crossflow Displacement Thickness Calculations

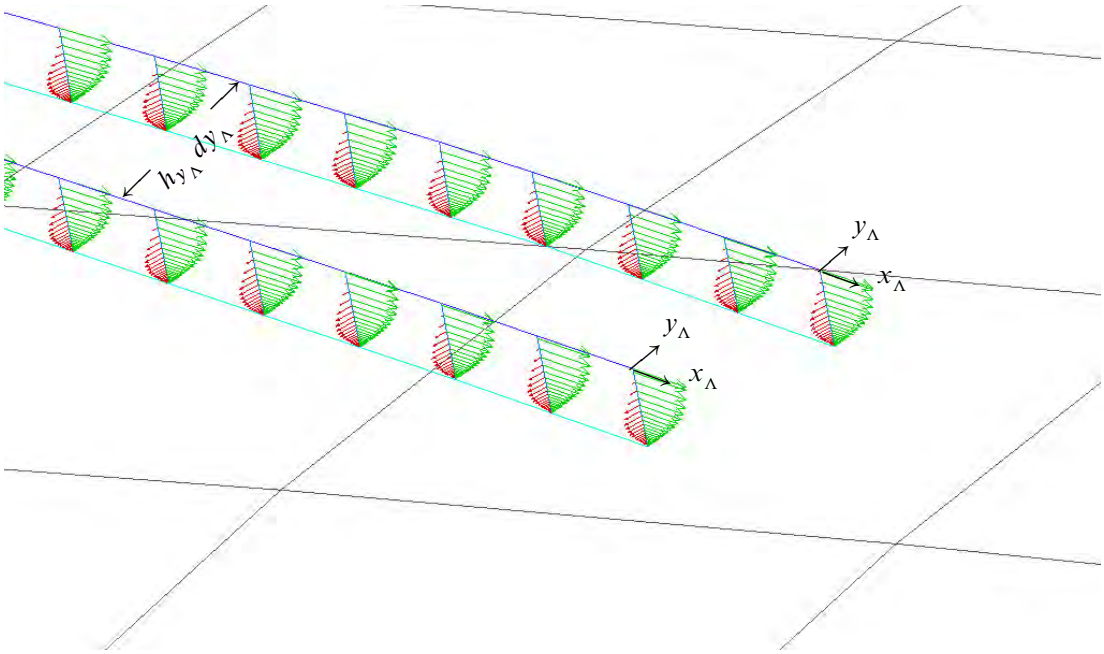

(b) Closeup of two planes normal to surface and parallel to streamline at the boundary layer edge. The relative length of crossflow velocity vectors (red) increased by ten times that of streamwise velocity vector (green).

Figure 9.9: Crossflow Displacement Thickness. The streamlines and velocity vectors shown are for a laminar section of flow with the spheroid at $\alpha = -10.2°$, $Re_l = 4.0 \times 10^6$.

the difference in crossflow between two of these planes aligned with the external streamline started a small distance apart. The starting point is offset a distance based on the size of the wall face, parallel with this wall face and perpendicular to the velocity at the boundary layer edge. The accumulation or dispersion of fluid is calculated from the difference in crossflow volume between these two planes. Fig. 9.9 shows two of these planes aligned with the external streamline and the velocity vectors used in determining the crossflow volume for a wall face located near the streamwise midpoint of the spheroid. Once the accumulation or dispersion of fluid on the streamline upstream of a wall face is known, the influence of crossflow on the displacement thickness at that wall face may be calculated.

9.2 Results and Discussion for $\alpha = -0.2°$

9.2.1 $Re_l = 2.0 \times 10^6$

Sph_Grid_0A is used in the initial studies at this incidence; its resolution is the same as *Sph_Grid-10A* (Table 9.1). In Subsection 4.4.1 a pressure differential between $\varphi = 0°$ and $180°$ was measured; the classical potential solution for the spheroid in isolation showed this difference was not accounted for by the slight incidence, $\alpha = -0.2°$, of the model. Fig. 9.10 compares the measured C_p values with the results of computation using Fluent employing the realisable k-ε turbulence model for $Re_l = 2.0 \times 10^6$. The difference between the measured and computed C_p distributions for $\varphi = 0°$ and $180°$ is approximately constant over the front 60% of the model: at $x_{bc}/l = -0.046$ the difference is 0.010 for both. The measured C_p at $x_{bc}/l = -0.046$ is approximately 0.004 greater than the calculated values for the three azimuths shown in Fig. 9.10. This difference is not of immediate concern as:

- this computation treats the entire spheroid boundary layer as turbulent, while the boundary layer survey (Section 8.5) shows boundary layer transition for $Re_l = 2.0 \times 10^6$ occurring downstream of the centre, in the vicinity of $x_{bc}/l \approx -0.35$.
- a small shift in C_p was observed between laminar and turbulent regions in the measured results.
- the surface pressure distribution over the rear of the body displays an earlier boundary layer separation, and consequently smaller base pressure, for the computed results. This is reasonable as the thicker boundary layer produced by modelling the entire boundary layer of the spheroid as turbulent is expected to separate earlier.

In summary, the difference between the measured and computed surface static pressure at $\varphi = 0°$ and $180°$ near the mid-body is similar. The absolute values of the measured and

computed static surface pressure at this location are slightly different. Contour plots of static pressure on the plane $y_{bc} = 0$ confirm an increase in static pressure extends well upstream of the support foil. This results in a lack of symmetry of the contour lines about the $z_{bc} = 0$ plane.

The major aim of this computational work was to examine the performance of the computational modelling when the turbulence models are applied only in regions where the boundary layer has been measured as turbulent. The reasonable place to start this investigation is at zero incidence (almost) with an axisymmetric body. Fig. 9.11 shows a comparison between the C_p distribution calculated at $Re_l = 2.0 \times 10^6$ for: an inviscid solution; a body with the front half of the model laminar and the rest of the domain turbulent; an entirely turbulent domain; and the measured data. The minimal difference in the computed C_p distribution between the solution that allowed for the laminar forebody and the fully turbulent solution was unexpected given the experimental observations. The C_p measurements displayed a small increase in pressure downstream of the boundary layer transition, with the curves for the Reynolds numbers downstream of boundary layer transition typically[1] creating a new grouping as discussed in Subsection 4.4.2.

It is worth examining results from a coupled inviscid-viscous solver at this point to examine the calculated surface pressure distributions when boundary layer transition is forced at different locations. The two-dimensional X-foil code [90] was used on a 6.67–1 elliptical cylinder for this comparison as it provides a similar range in C_p. At $\alpha = 0°$, $Re_l = 1.0 \times 10^6$ the X-foil results show the C_p curves for the laminar group approximately 0.01 less than the curves for the turbulent boundary layer (Fig. 9.12(a)). The insert in Fig. 9.12(a) shows only a minor difference in base pressure when the location of the forced transition is between $x_{bc}/l = -0.4$ and 0.1. Repeating the calculations using Fluent on the same elliptical cylinder results in a similar magnitude shift in C_p between the laminar and turbulent curves, although a greater range in base pressure (Fig. 9.12(b)). The calculations with Fluent used the realisable k-ε turbulence model with a boundary layer transition region of length $x_{bc}/l = 0.03$. In contrast the X-foil calculations assume an immediate commencement of a turbulent boundary layer. The realisable k-ε turbulence model displays a rapid increase in surface shear stress once the transition zone has commenced, as evidenced by the location and sharpness of the perturbation observed in Fig. 9.12(b). Later in this chapter it is observed that the increase in surface shear stress with the SST turbulence model is more gradual.

The next step was to examine the calculated surface pressure on the spheroid in axisymmetric ($\alpha = -0.2°$) flow with boundary layer transition forced at set locations. This allows

[1] A significantly earlier boundary layer transition may result in earlier boundary layer separation with reduced base C_p having an influence upstream.

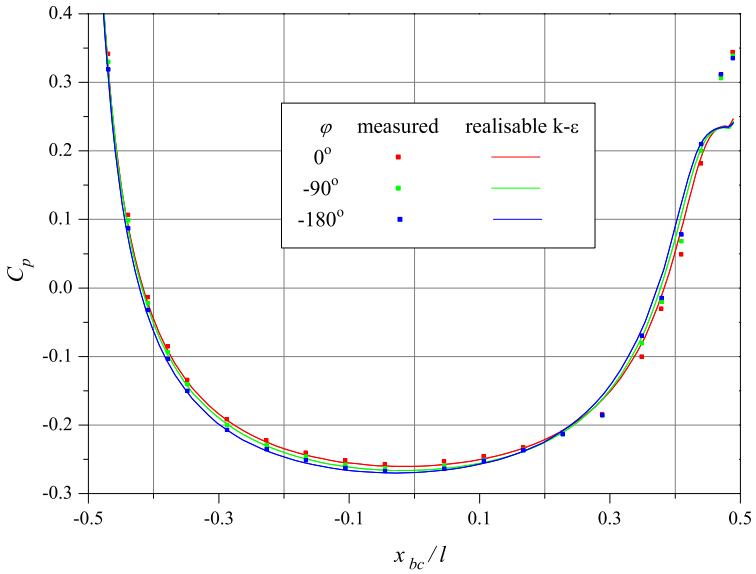

	average base C_p
measured	0.341
fully turbulent	**0.235**

Figure 9.10: Comparison of surface pressure measurements with numerical results, $Re_l = 2.0 \times 10^6$, $\alpha = -0.2°$. The difference between the surface pressure distribution for $\varphi = 0°$ and 180° is attributed to blockage caused by the support foil. There is a significant difference between the calculated and measured base pressure.

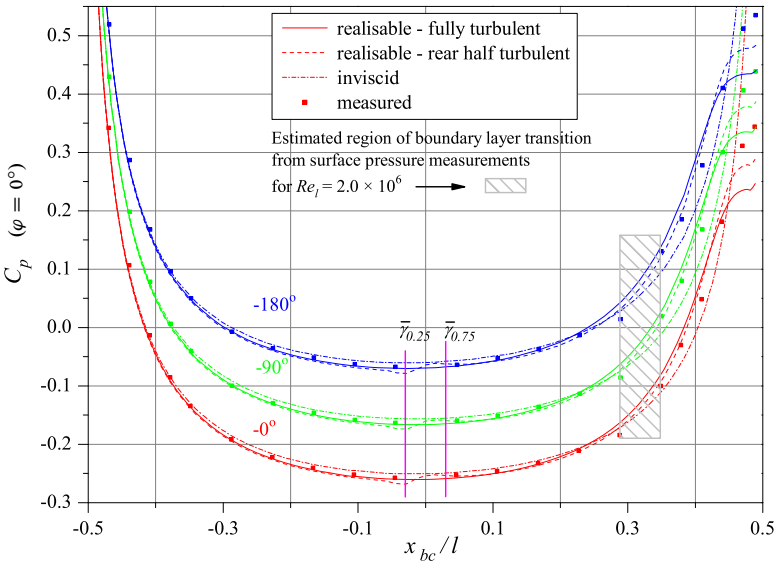

	average base C_p
measured	0.341
rear half turbulent	**0.274**
fully turbulent	**0.235**

Figure 9.11: Comparison between measured and numerical surface pressure distributions with boundary layer transition set to occur at $x_{bc}/l \approx 0$ for one set of the numerical results, $Re_l = 2.0 \times 10^6$, $\alpha = -0.2°$, *Sph_Grid_0A*. Values for $\varphi = -90°$ and $-180°$ offset in the vertical direction 0.1 and 0.2 respectively. There is minimal difference in C_p between the fully turbulent solution and the solution that allows for the front half being laminar over the upstream 75% of the body, except in the boundary layer transition region. The difference between the inviscid and other computed solutions shows that the boundary layer is influencing the C_p values. C_p values for each azimuth progressively displaced by 0.1 for $\varphi < 0°$.

examination of the surface pressure distributions to observe if they form two sets of curves, with a switch from one group to the other occurring around the location of transition. Fig. 9.13 shows this does not occur: after a short perturbation at the location of boundary layer transition the curves tend to return to a single set of curves. The single set of curves starts to diverge towards the rear of the model.

While examining the influence of boundary layer transition on surface pressure it is worth noting that Popov et al. [101] used X-foil in the validation of a technique to locate boundary layer transition by using the maximum curvature of the surface pressure distribution. It is of some interest that at almost the same time Clarke et al. [102] were noting the disparity between measured surface pressure distributions on a spheroid in three-dimensional flow and those obtained using a modern finite volume code for a boundary layer in transitional flow Popov et al. were using the surface pressure distribution from a coupled inviscid-viscous solver to determine the location of transition. The solution from the finite volume code on the spheroid may still have a maximum curvature in the surface pressure distribution in the region of boundary layer transition; however, the overall shift in surface pressure distribution between the laminar and turbulent curves seen in the X-foil and Fluent results on an elliptical cylinder and in the measurements on the spheroid is not apparent in the calculations obtained using the Fluent code with the realisable k-ε turbulence model on the spheroid (Fig. 9.11).

Due to the disparity between the measured and computed surface pressure distributions on the spheroid at $\alpha = -0.2°$ an examination of the boundary layer properties from the finite volume solution is performed. In this (almost) axisymmetric case it is possible to compare the momentum thickness obtained using the previously mentioned Mangler transformation of Thwaites' method [73] in Subsection 8.2.1 with those of the finite volume solution using the code described in Subsection 9.1.3. Except near the stagnation region ($x_{bc}/l = -0.5$) Fig. 9.14 shows good agreement for the momentum thickness in the region of laminar flow. This agreement suggests that in the absence of crossflow the momentum thickness calculation is reasonable. The momentum thickness obtained with the finite volume solution shows a considerable increase in its rate of change downstream of the boundary layer transition region. This is expected with a turbulent boundary layer.

The calculated boundary layer properties using Fluent on the *Sph_Grid_0A* mesh for a fully turbulent case and one with boundary layer transition implemented at the measured location, when no trip was used, is shown in Fig. 9.15(a) for $Re_l = 2.0 \times 10^6$, $\varphi = -90°$. The turbulence was modelled using the realisable k-ε model. For the case with the transitional boundary layer:

- The wall shear stress coefficient approaches zero, indicating laminar boundary layer separation in this approximately axisymmetric case, near $x_{bc}/l = 0.25$; no subsequent reat-

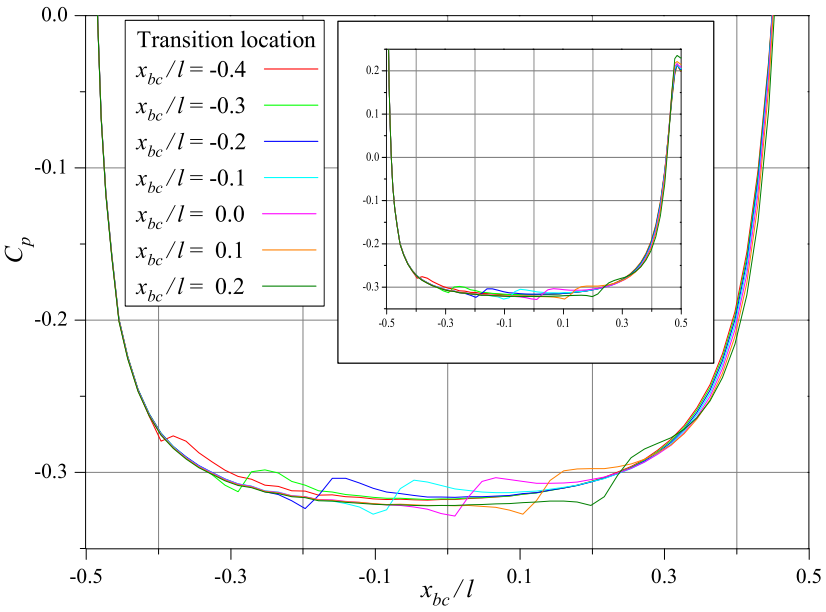

transition location x_{bc}/l	base C_p
-0.4	0.200
-0.3	0.201
-0.2	0.203
-0.1	0.205
0.0	0.209
0.1	0.215
0.2	0.230

(a) C_p calculated using X-foil with boundary layer transition set to occur between $x_{bc}/l = -0.4$ and 0.2 inclusive at $x_{bc}/l = 0.1$ intervals. The X-foil calculations assume an immediate switch from laminar to turbulent boundary layer.

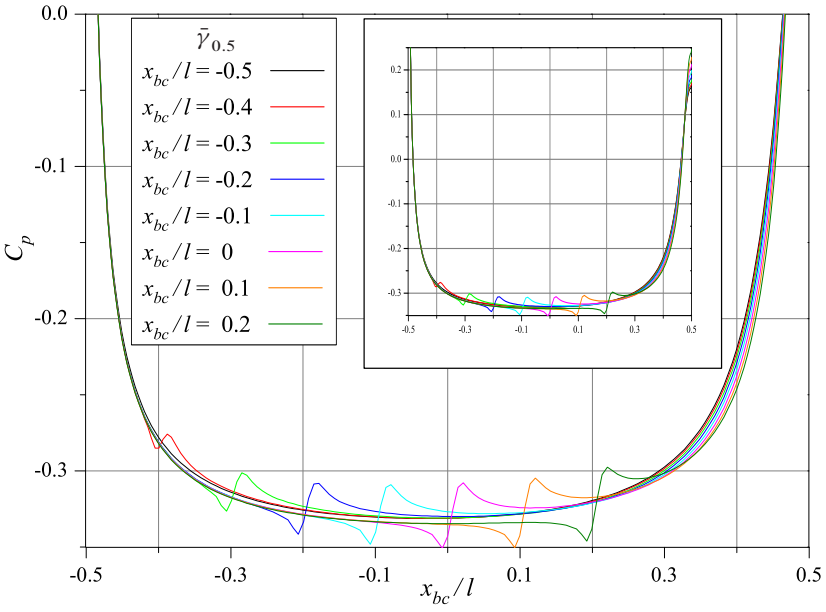

$\bar{\gamma}_{0.5}$ x_{bc}/l	base C_p
-0.5	0.167
-0.4	0.171
-0.3	0.179
-0.2	0.188
-0.1	0.199
0.0	0.212
0.1	0.228
0.2	0.246

(b) C_p calculated using Fluent with realisable k-ε turbulence model with boundary layer transition set to occur between $x_{bc}/l = -0.5$ and 0.2 inclusive at $x_{bc}/l = 0.1$ intervals. A length of the transition region was set to $x_{bc}/l = 0.03$.

Figure 9.12: Surface pressure calculations on a 6.67-1 elliptical cylinder at $\alpha = 0.0°$, $Re_l = 1.0 \times 10^6$. The coupled inviscid-viscous solver and the finite volume code both show a similar size shift in C_p after the transition region. The perturbation of the curves in the transition region is slightly larger with the finite volume code; this may in part be due to the greater resolution employed with the finite volume code.

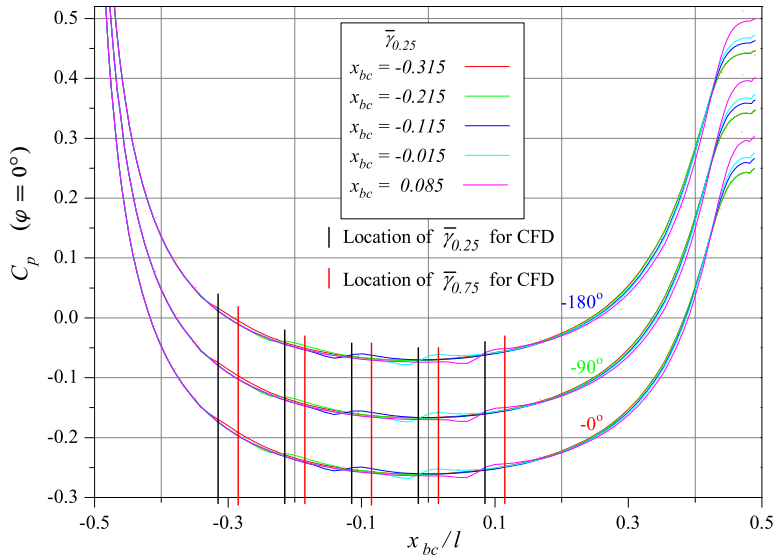

$\bar{\gamma}_{0.25}$ x_{bc}/l	base C_p
-0.315	0.247
-0.215	0.248
-0.115	0.264
-0.015	0.274
0.085	0.301

Figure 9.13: Comparison of calculated surface pressure distributions with boundary layer transition set to occur at $x_{bc}/l = 0.1$ intervals between -0.3 and 0.1 inclusive using the realisable k-ε turbulence model, $Re_l = 2.0 \times 10^6$, $\alpha = -0.2°$, *Sph_Grid_0A*. Values for $\varphi = -90°$ and $-180°$ offset in the vertical direction 0.1 and 0.2 respectively. There is minimal difference in C_p between the distributions except near the location of the boundary layer transition and towards the rear of the body. The base pressure displays a range of 0.06 showing the greater length of turbulent boundary layer results in a noticeable reduction in the pressure recovery. C_p values for each azimuth progressively displaced by 0.1 for $\varphi < 0°$.

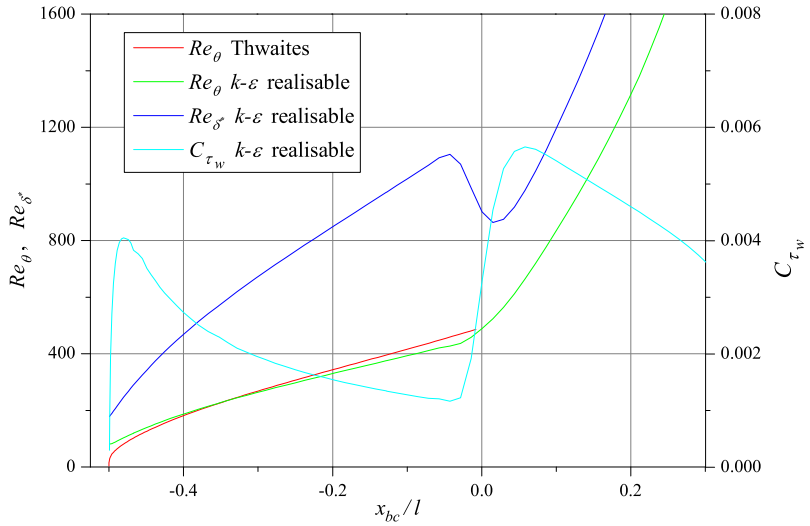

Figure 9.14: Boundary layer properties for approximately axisymmetric flow on 3–1 spheroid calculated using *Sph_Grid_0A* with a realisable k-ε turbulence model, $\alpha = -0.2°$, $Re_l = 2.0 \times 10^6$, $\varphi = -90°$. Mangler transformation of Thwaites method solved for axisymmetric flow using velocity distribution from classical potential theory on ideal spheroid at $Re_l = 2.0 \times 10^6$.

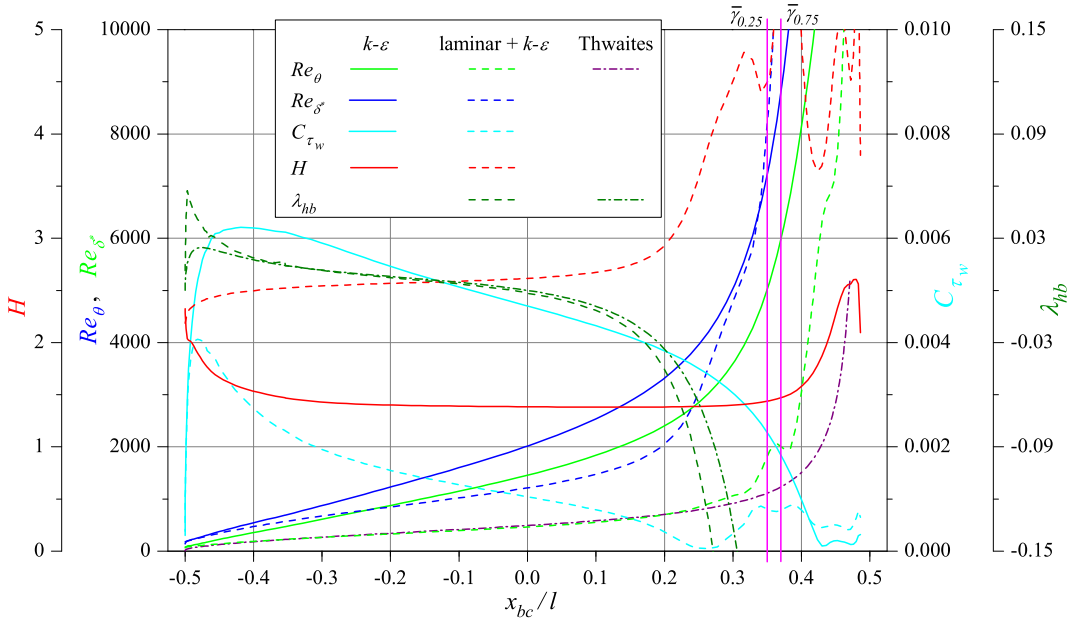

(a) Comparison of results from *Sph_Grid_0A* with and without laminar regions being set.

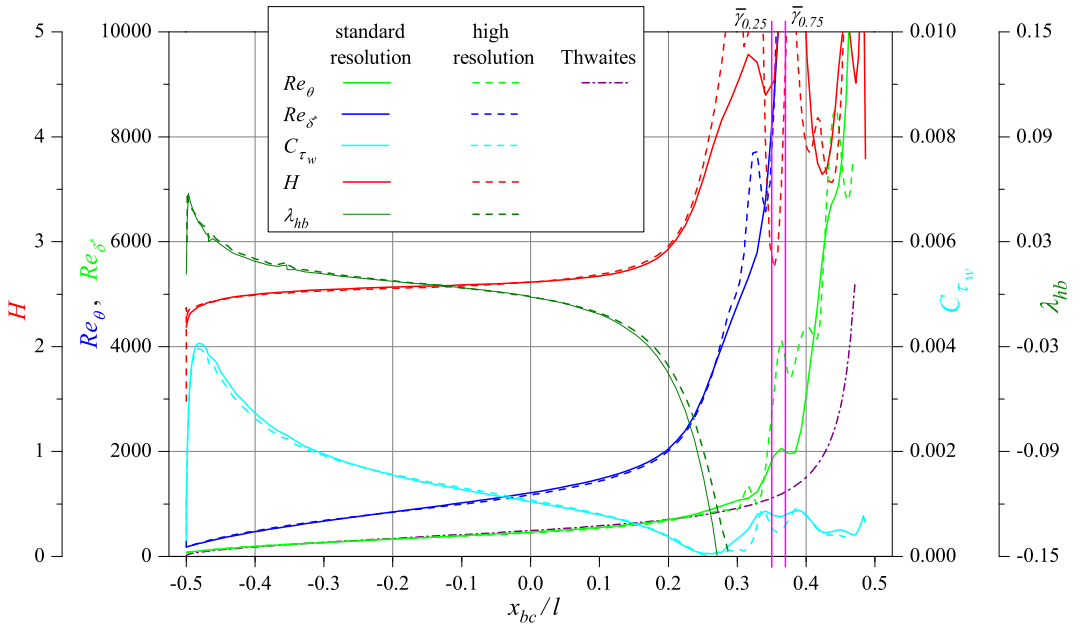

(b) Comparison of boundary layer properties from *Sph_Grid_0A* and *Sph_Grid_0A-Adapt* with laminar regions implemented from measured results. This result shows that *Sph_Grid_0A* has not achieved grid independence in the region after laminar separation even though the results on the equivalent density mesh in the fully turbulent case at $\alpha = -10.2°$ were grid independent.

Figure 9.15: Boundary layer properties for approximately axisymmetric flow on 3–1 spheroid using realisable k-ε turbulence model with and without laminar regions, $Re_l = 2.0 \times 10^6$, $\alpha = -0.2°$, $\varphi = -90°$. Mangler transformation of Thwaites method solved for axisymmetric flow using velocity distribution from classical potential calculation on ideal spheroid at $Re_l = 2.0 \times 10^6$.

tachment to the body is predicted. Laminar separation, near $x_{bc}/l = 0.25$; without reattachment, is predicted for all azimuths except for a thin region $0° \geqslant \varphi \gtrapprox -10°$ where reattachment occurs. The laminar separation is well upstream of both the measured boundary layer transition location of $x_{bc}/l \approx 0.35$ (Table 8.3) and the location of the measured turbulent boundary layer separation at $x_{bc}/l \approx 0.46$ shown in the flow visualisation (Fig. 7.14).

- The shape factor value of approximately 2.5 near the centre of the model where there is minimal pressure gradient would appear reasonable, as does its value of approximately 3.6 at laminar separation. Re_θ calculated by Thwaites' method from the classical potential solution is close to that calculated with the transitional boundary layer until just prior to boundary layer separation.

To investigate the discrepancy between the measured location of boundary layer separation and that predicted by the CFD methods, an integral method based on the boundary layer equations was used. The Holstein-Bohlen parameter (also called Thwaites' pressure gradient coefficient), λ_{hb}, is given by

$$\lambda_{hb} = \frac{\theta^2}{\nu} \frac{dU_e}{dx} \tag{9.10}$$

where U_e is the velocity outside the boundary layer.

A value for this parameter of -0.09 is often used to indicate separation in two-dimensional flows (and possible axisymmetric flows [87]). With the aim of bracketing the range of expected separation locations this technique was applied to both: the values calculated from the CFD when premature laminar separation has occurred resulting in reduced pressure recovery; and the results from the classical potential solution with no sting and full pressure recovery. Using the results from the realisable k-ε turbulence model for $Re_l = 2.0 \times 10^6$ gave $\lambda_{hb} = -0.09$ at $x_{bc}/l \approx 0.24$. Repeating this calculation using the velocity distribution of the classical potential solution and Thwaites' estimate of the momentum thickness $\lambda_{hb} = -0.09$ at $x_{bc}/l \approx 0.27$; this result is invariant with Reynolds number. For a linearly decelerating flow Thwaites found $\lambda_{hb} = -0.082$ at separation; for the spheroid with its initially increasing then decreasing streamwise velocity Thwaites method is expected to slightly underpredict θ and thus λ_{hb}, which would tend to indicate a later laminar separation. Curle [103] graphed λ_{hb} at separation against his second parameter μ_C where

$$\mu_C = \left(\lambda_{hb}/\frac{dU_e}{dx}\right)^2 U_e \frac{d^2U_e}{dx^2} = \frac{\theta^4}{\nu^2} \frac{d^2U_e}{dx^2} \tag{9.11}$$

This plot shows that the value of λ_{hb} at separation decreases in a increasingly adverse pressure gradient ($\frac{d^2U_e}{dx^2} < 0$) to a minimum of $\lambda_{hb} \approx -0.11$, with a corresponding value of $H \approx 3.55$. However, as the slope λ_{hb} against x_{bc}/l is steep in Fig. 9.15 a change in λ_{hb} at separation from -0.08 to -0.11 will have only a minor influence on the location of separation determined using this technique. The surface streamlines show the predicted flow using the CFD is far from axisymmetric. These methods of predicting the location of separation were developed for two-dimensional flow and were applied via the Mangler transformation for axisymmetric flow. The significant degree of non-axisymmetric flow in the current CFD result suggests that it is unlikely that these integral methods will assist in examining the discrepancy between the calculated and measured location of separation. The value of λ_{hb} will also be influenced by the boundary layer transition zone as the transition causes a perturbation in the surface pressure distribution. This perturbation extends for approximately $x_{bc}/l = 0.07$ upstream of $\bar{\gamma}_{0.25}$ for the spheroid in Fig. 9.13. The perturbation results in an initially more favourable pressure gradient upstream of the transition region and then a less favourable pressure gradient shortly into it than would exist without the transition region. This influence is examined in more detail on a finer mesh with a measured transition length later in the subsection. However, in this case (Fig. 9.15) λ_{hb} becomes less than -0.11 far enough upstream of the transition region so it should not have a significant influence.

Boundary layer transition may occur via a short laminar separation bubble; this was observed in Fig. 7.10 on the spheroid at this Reynolds number when $\alpha = -10.2°$ for φ between $0°$ and approximately $-60°$. This mode of boundary layer transition highlights a deficiency in the present method of presetting the laminar and turbulent regions. If a laminar separation is calculated to occur upstream of the measured turbulent region the flow is less likely to reattach in a predefined laminar zone. Ideally the computed shear layer should transition to turbulence shortly downstream of the laminar separation. A general problem with a short laminar separation bubble is that a significant local increase in mesh resolution is required in its vicinity to resolve the flow accurately. The turbulent reattachment also requires an appropriate switching on of the turbulence model. Stock and Haase [104] in some of their calculations fix boundary layer transition just upstream of where laminar separation would otherwise occur. Menter et al. [92] in their transition model encourage more rapid reattachment of laminar separations by allowing the intermittency factor to become greater than unity in a region of separated flow.

The lack of grid independence in the computed results downstream of the laminar separation (Fig. 9.15(b)) suggests an increase in grid density is required in this region. The resolution of the meshes used for this incidence are listed in Table 9.2. The surface streamlines shown in Fig. 9.16 display grid independence for the pattern of surface streamlines between *Sph_Grid_0B-*

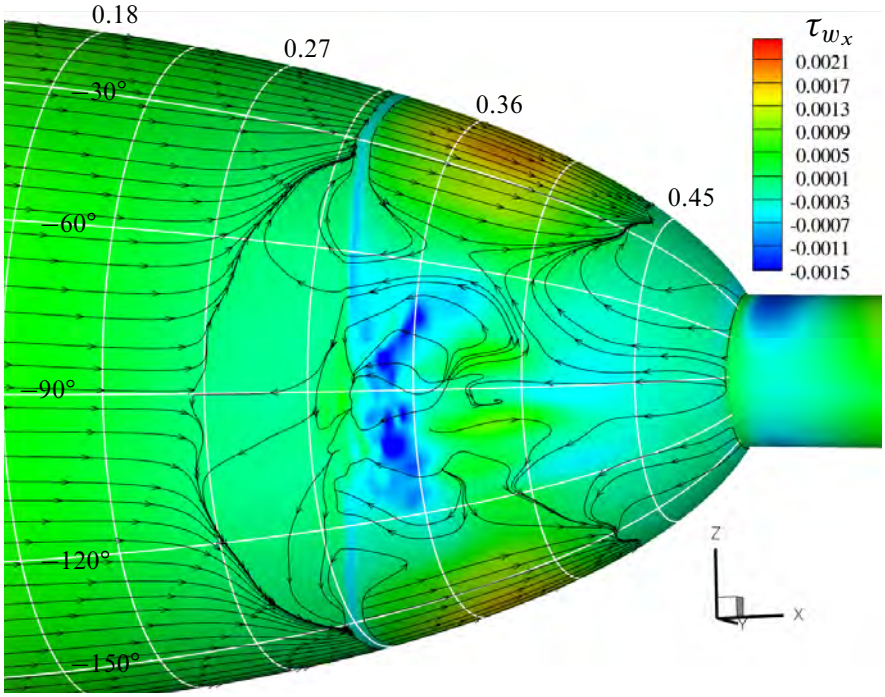

(a) *Sph_Grid_0B-Adapt*, approximately 6 streamwise intervals across the laminar separation bubble near $x_{bc}/l \approx 0.32$, $\varphi \approx -30°$

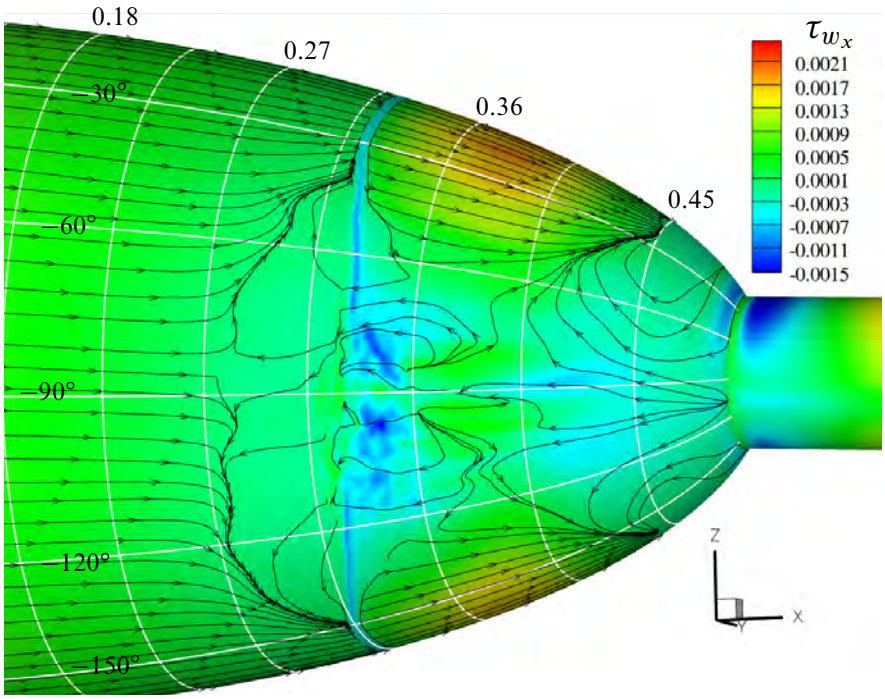

(b) *Sph_Grid_0C-Adapt*, approximately 9 streamwise intervals across the laminar separation bubble near $x_{bc}/l \approx 0.32$, $\varphi \approx -30°$

Figure 9.16: Computed surface streamlines on 3–1 spheroid using realisable k-ε turbulence model with laminar regions, $Re_l = 2.0 \times 10^6$, $\alpha = -0.2°$. Comparison between the streamlines shows a relatively high level of grid independence in the pattern of the surface streamlines between *Sph_Grid_0B-Adapt* and *Sph_Grid_0C-Adapt*. Contours of wall shear stress in the x_{bc} direction show similar results except on the flank.

grid name	normal intervals	azimuthal intervals[a]	longitudinal intervals	
			front half	rear half
Sph_Grid_0A	56	54	54	48
Sph_Grid_0A-Adapt	112	108	108	96
Sph_Grid_0B	56	54	54	146
Sph_Grid_0C	56	80	74	252
Sph_Grid_0B-Adapt	112	108	108	292
Sph_Grid_0C-Adapt	112	160	148	504

[a] These intervals distributed over 180°.

Table 9.2: Grid resolution on and normal to spheroid surface for 3–1 spheroid at $-0.2°$ incidence.

Adapt and *Sph_Grid_0C-Adapt*, though a small variation in the streamwise location of the flow separation is apparent near $x_{bc}/l \approx 0.32$, $-60° \geqslant \varphi \geqslant -120°$.

The results from the two high resolution meshes show a separation bubble at $x_{bc}/l \approx 0.32$ (Fig. 9.16) for $0° \geqslant \varphi \geqslant -40°$ and $-150° \geqslant \varphi \geqslant -180°$; for these azimuth angles the turbulent separation has moved downstream to $x_{bc}/l \approx 0.44$. The separation bubble, however, is calculated to start shortly downstream of the start of the predefined turbulent region ($\bar{\gamma} \lessapprox 0.4$) rather than shortly upstream of it. On the flank of the model, where the location of boundary layer transition was measured to occur at $x_{bc}/l \approx 0.35$, fractionally further downstream than for the upper and lower surfaces ($x_{bc}/l \approx 0.315$, Table 8.3), flow separation occurs upstream at $x_{bc}/l \approx 0.29$ with no reattachment of the separated flow on the flank.

Measured and calculated surface pressure distributions are shown in Fig. 9.17. A significant difference exists between the distributions calculated using *Sph_Grid_0A* and *Sph_Grid_0C-Adapt* both upstream and downstream of the location of boundary layer transition. The corresponding difference is smaller between *Sph_Grid_0B* and *Sph_Grid_0C-Adapt* and negligible between *Sph_Grid_0B-Adapt* and *Sph_Grid_0C-Adapt*. The pressure distribution calculated using the higher resolution meshes on the azimuths where the flow has reattached compare favourably with measured values; with the exception of the most downstream surface measurement adjacent to the flank which is influenced by the flank separation. On the flank of the model calculated pressure distributions have unrealistic oscillations. The free shear layer above the surface where the oscillations are observed may be more susceptible to numeric instabilities. Further refinement was not attempted due to the minimal difference between the results obtained using *Sph_Grid_0B-Adapt* and *Sph_Grid_0C-Adapt* despite the significant increase in grid resolution.

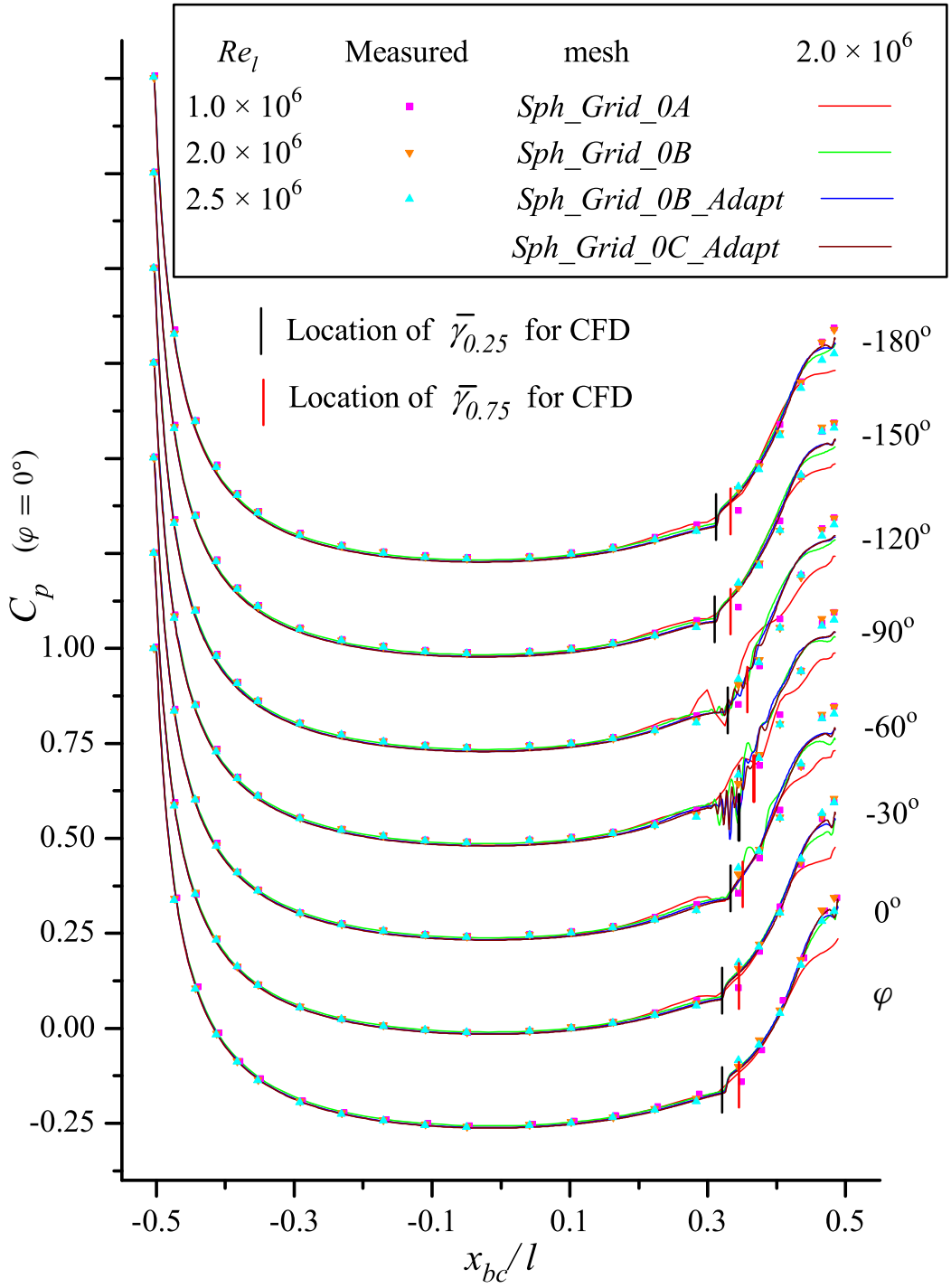

Figure 9.17: Computed and measured surface pressure distribution on spheroid, $\alpha = -0.2°$, realisable k-ε turbulence model. C_p values for each azimuth progressively displaced by 0.25 for $\varphi < 0°$. Results for the lower resolution mesh display a reduced base pressure.

Boundary layer properties calculated using the realisable k-ε turbulence model where the flow has reattached at $\varphi = -30°$ and where it has failed to reattach at $\varphi = -90°$ are shown in Fig. 9.18. For $\varphi = -30°$ the boundary layer properties are similar for the two highest resolution meshes. Possible values of H at the separation of a laminar boundary layer are plotted as a function of λ_{hb} by both Curle [103], and Head and Hayasi [105]. Curle suggests a minimum of $H \approx 3.55$ at $\lambda_{hb} \approx -0.11$. Head and Hayasi show a monotonically decreasing H with decreasing λ_{hb}, with a minimum of $H \approx 3.47$ at $\lambda_{hb} \approx -0.14$. The shape factor of 3.2 at separation obtained from the finest mesh, *Sph_Grid_0C-Adapt*, is less than the minimum of 3.5 suggested above for a laminar boundary layer. For the finest grid at $\varphi = -30°$ (Fig. 9.18Fig. (a)) separation has commenced inside the transition region so the decrease in H may be attributed to the expected decrease in H as the boundary layer becomes turbulent; the boundary layer still separates as insufficient momentum has been transferred towards the wall by the intermittent turbulence. The separation bubble is, at least partly, due to the implementation of the boundary layer transition region as the separation bubble occurs in the first part of the transition region; this separation bubble is discussed later in this subsection and at the end of this chapter. At $\varphi = -90°$ the boundary layer properties for the two highest resolution meshes display significant differences upstream and downstream of the laminar separation. Another complication in interpreting the results of the boundary layer properties is that once crossflow occurs the momentum thickness and thus shape factor must allow for convergence or divergence effects[2]; crossflow has not been accounted for in this almost axisymmetric case.

Measurements at $\alpha = -0.2°$ in some cases appeared to be sensitive to apparently minor (negligible) changes in the setup resulting in non-axisymmetric results. This sensitivity was attributed to the minimal azimuthal pressure gradients allowing small surface perturbations to influence the development of the boundary layer. The small variation with azimuth in the observed axial location of boundary layer transition may have a computational equivalent. In order to investigate this a calculation using *Sph_Grid_0C-Adapt* was repeated with constant axial locations of $x_{bc}/l = 0.315$ and 0.34 for $\bar{\gamma}_{0.25}$ and $\bar{\gamma}_{0.75}$ respectively. These figures were based on the average values at $\varphi = -30°$ and $-150°$. This modification resulted in a consistent streamwise location of the separation bubble (in the boundary layer transition region) for all azimuthal angles and a turbulent separation at $x_{bc}/l \approx 0.44$. Contours of shear stress and the calculated surface streamlines for this case are shown in Fig. 9.19. The calculated surface pressure distributions when the constant streamwise location for transition is applied show good agreement with calculated measured data (Fig. 9.20). The calculated base C_p in this case is a good match with the measured base C_p. Over the front half of the body minimal difference is

[2]The Mangler transformation will allow for convergence or divergence effects resulting from body radius changes in axisymmetric flow.

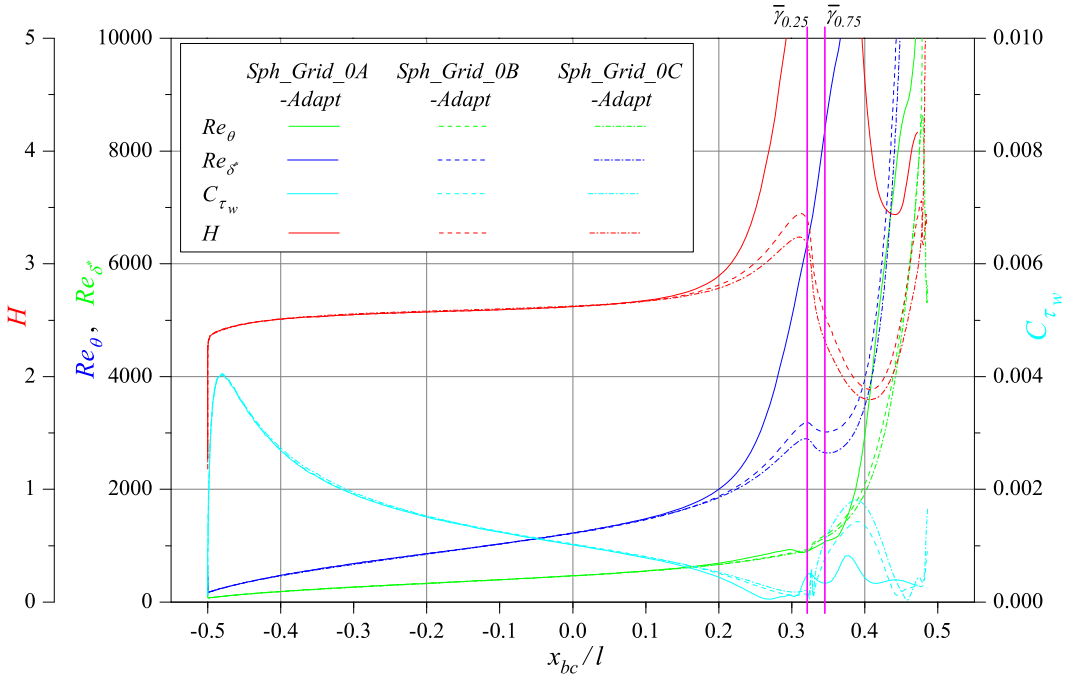

(a) $\varphi = -30°$, where the computed flow has reattached.

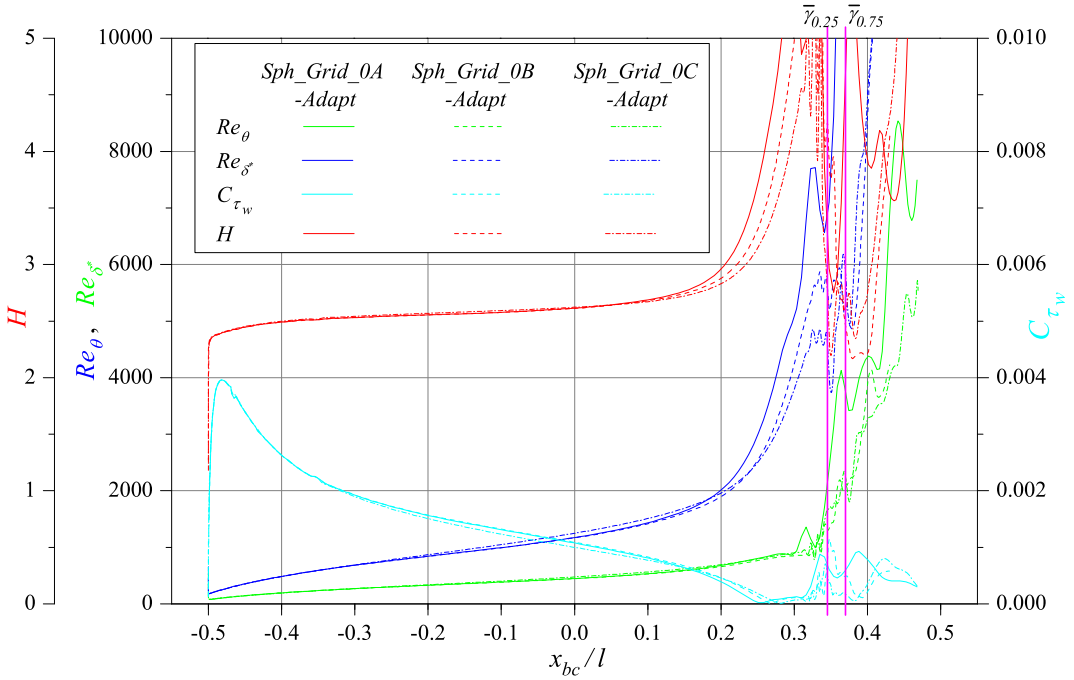

(b) $\varphi = -90°$, where the computed flow has not reattached.

Figure 9.18: Boundary layer properties for approximately axisymmetric flow on 3–1 spheroid using realisable k-ε turbulence model, $Re_l = 2.0 \times 10^6$, $\alpha = -0.2°$, $\varphi = -90°$. Location of $\bar{\gamma}_{0.25}$ and $\bar{\gamma}_{0.75}$ from FRTPP measurements.

seen in the calculated surface pressure distribution between the laminar and turbulent boundary layers in Fig. 9.21, this is at odds with the measured results and unexpected given the results computed using this finite volume code on the elliptical cylinder.[3]

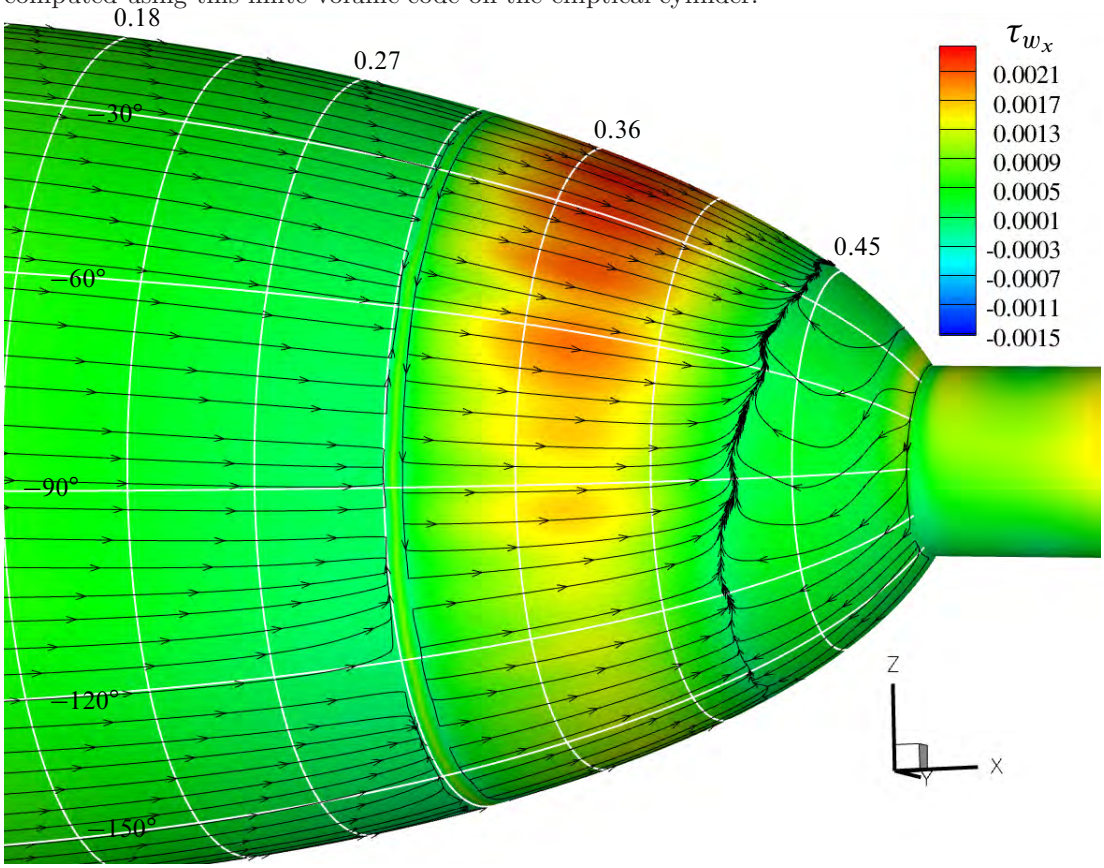

Figure 9.19: Computed surface streamlines on 3–1 spheroid using realisable k-ε turbulence model with laminar regions, $\alpha = -0.2°$, $Re_l = 2.0 \times 10^6$, $\varphi = -45°$. Replacing the measured transition region with an axisymmetric transition region in the vicinity of the measured transition region results in a significant change in the surface streamlines.

As noted in Subsection 8.5, intermittency values in the boundary layer transition region have been implemented using Dhawan and Narasimha's [85] distribution of intermittency and the measured location of $\bar{\gamma}_{0.25}$ and $\bar{\gamma}_{0.75}$. For *Sph_Grid_0C-Adapt* using the boundary layer survey results at $Re_l = 2.0 \times 10^6$, $\alpha = -0.2°$ this placed approximately 120 grid intervals in the streamwise direction between $x_{\bar{\gamma}_{0.01}}$ and $x_{\bar{\gamma}_{0.99}}$, with approximately 40 of these between $x_{\bar{\gamma}_{0.25}}$ and $x_{\bar{\gamma}_{0.75}}$. The large number of cells combined with Dhawan and Narasimha's [85] distribution of intermittency allows a smooth implementation of the turbulent region so the separation

[3]With the realisable k-ε turbulence model the turbulent boundary layer is rapidly established. This is evident from the significantly greater surface shear stress just downstream of the stagnation point observed for the fully turbulent solution when compared to the results with the measured laminar region implemented, Fig. 9.15(a).

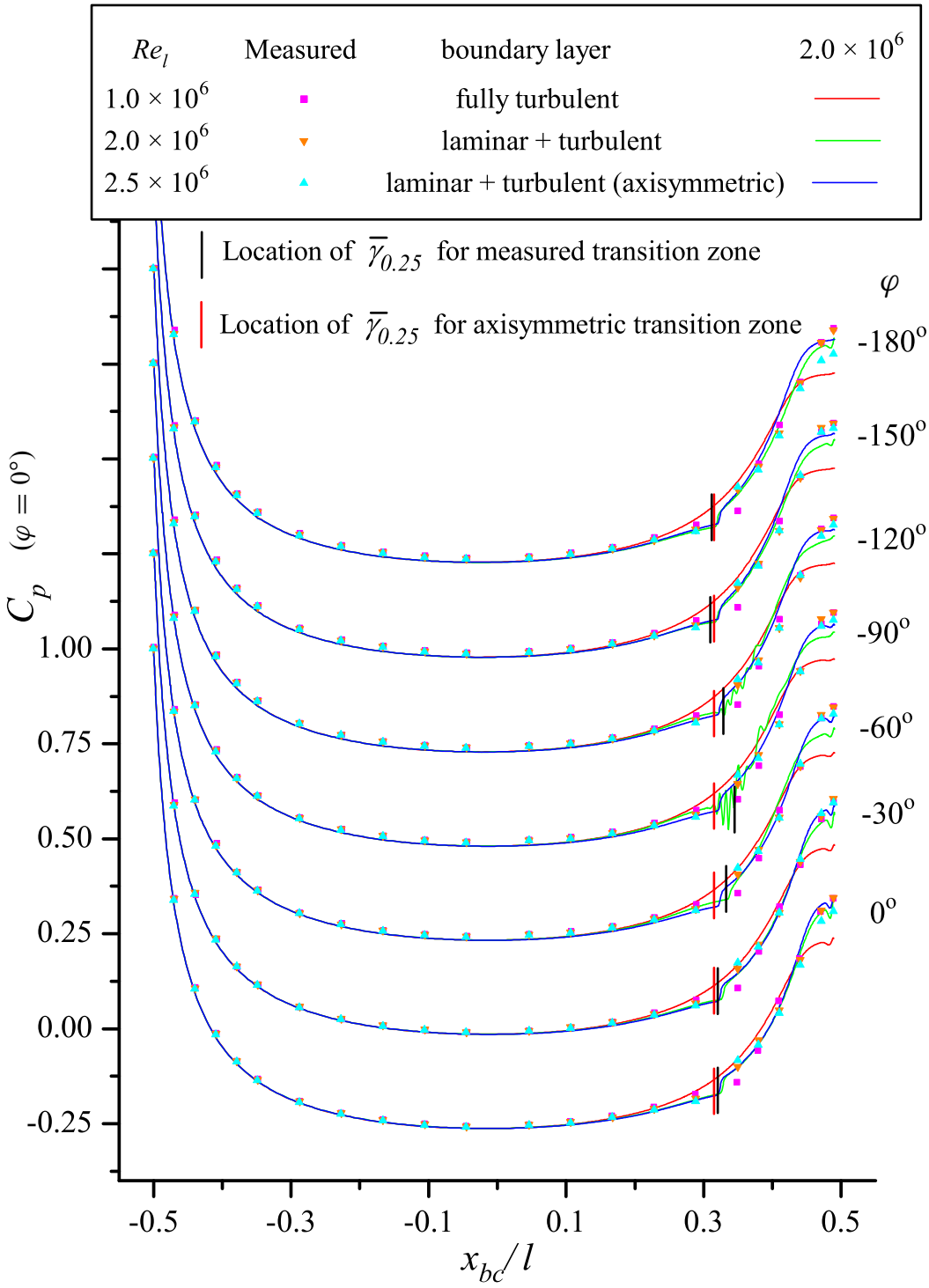

Figure 9.20: Computed and measured surface pressure distribution on spheroid, $\alpha = -0.2°$, realisable k-ε turbulence model, *Sph_Grid_0C-Adapt*. C_p values for each azimuth progressively displaced by 0.25 for $\varphi < 0°$. Use of a constant streamwise location prevented boundary layer separation on the flank of the spheroid. This highlights the sensitivity of this calculation to the implementation of the boundary layer transition region. It is also worth noting the minimal difference in the calculated surface C_p where the boundary layer is laminar or turbulent over the upstream 60% of the spheroid. Location of $\bar{\gamma}_{0.25}$ and $\bar{\gamma}_{0.75}$ from FRTPP measurements.

bubble should not be due to a discontinuity in the implementation of boundary layer transition region. This is not to suggest the a smooth shift from laminar to turbulent boundary layer exists in practice, as the spatial and temporal variations in the measured boundary layer transition region displayed in Fig. 8.9, but in a steady RANS simulation this is a reasonable approach both physically and numerically. The difference between the results with the axisymmetric implementation of boundary layer transition using the average of the measured values and the implementation with the slight variation in axial location highlight the sensitivity of the calculation at this incidence and Reynolds number to relatively minor variations in the boundary layer.

Now that the laminar separation without reattachment has been avoided the separation bubble in the transition region is examined in greater detail in Fig. 9.22. For inviscid flow over the rear half of the spheroid at zero incidence $dC_p/d(x_{bc}/l)$ will monotonically increase as x_{bc} approaches the rear stagnation region. Fig. 9.22 shows $dC_p/d(x_{bc}/l)$ increasing as expected for $0.20 < x_{bc} < 0.25$. However, after $x_{bc}/l = 0.25$ $dC_p/d(x_{bc}/l)$ starts decreasing through to about $x_{bc}/l \approx 0.315$, well inside the transition zone ($\bar{\gamma}_{0.20}$). A large peak in the adverse pressure gradient occurs at $x_{bc}/l \approx 0.32$; the boundary layer separates prior to this peak. This shows how the variation of displacement thickness through the transition region is influencing this separation bubble.

Calculations performed using *Sph_Grid_0C-Adapt* with the SST turbulence model displayed flow separation upstream of the predetermined boundary layer transition region and a failure of the flow to reattach for all azimuthal angles.

9.2.2 $Re_l = 3.5 \times 10^6$

For $\alpha = -0.2°$, $Re_l = 3.5 \times 10^6$ boundary layer transition was measured to occur after a relatively short length of adverse pressure gradient (Table 8.3). This is upstream of where the boundary layer may be expected to separate from examining either the shape factor or the Holstein-Bohlen parameter as apparent in Fig. 9.23. Using the realisable k-ε turbulence model with increased mesh resolution resulted in negligible change in the shear stress or boundary layer parameters outside the transition region. Near the start of the boundary layer transition zone increased resolution resulted in a sharper dip in the displacement thickness with similar values in the remainder of the transition zone (Fig. 9.24). The SST turbulence model is slower to switch on. This slower switch on when the SST turbulence model is used without a predefined upstream laminar region with a bluff body is desirable, as it avoids the excessive production of k in the upstream stagnation region due to the large shear stress. This behaviour is less desirable when attempting to commence turbulence modelling at a particular location (unless

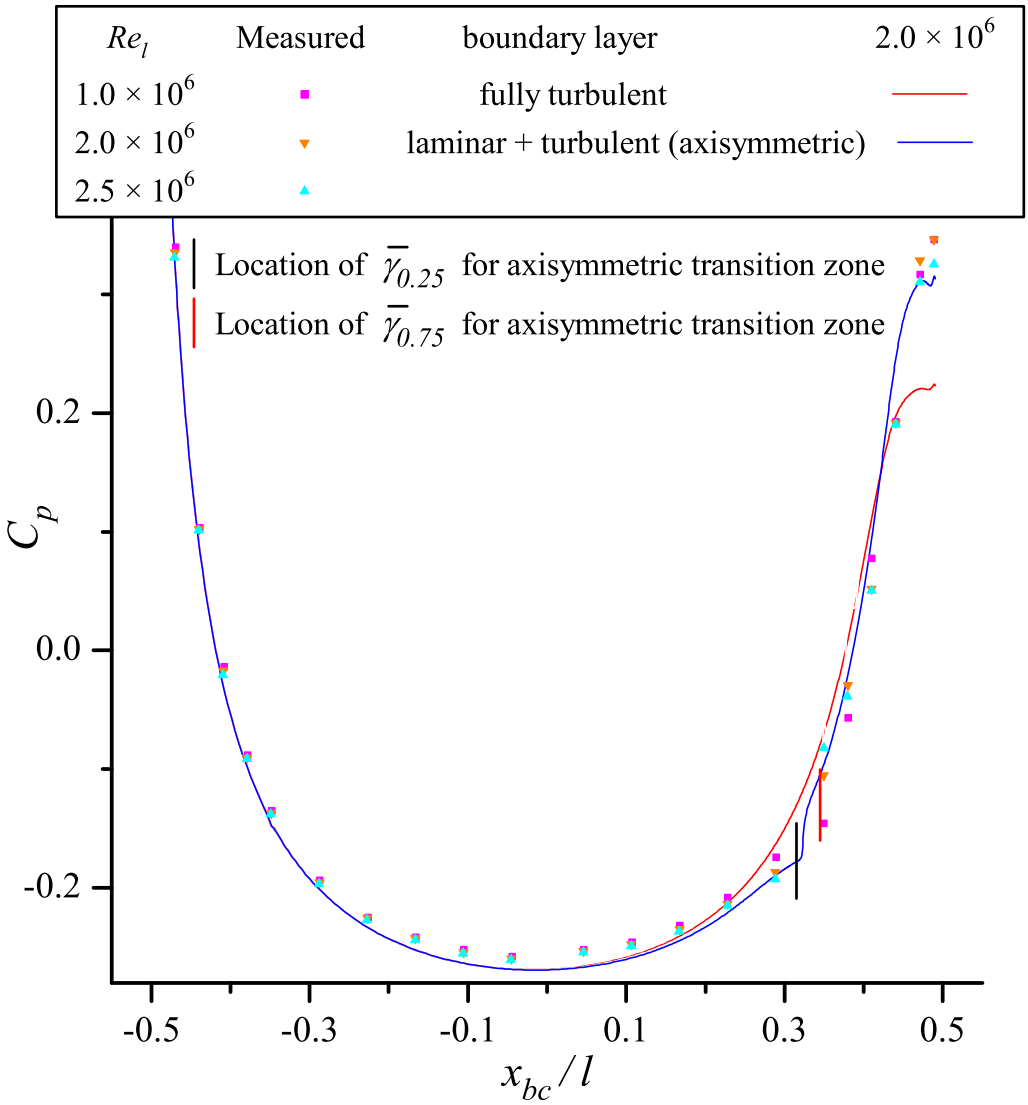

Figure 9.21: Close up of pressure distribution for approximately axisymmetric flow on 3–1 spheroid using realisable k-ε turbulence model and an axisymmetric implementation of the boundary layer transition region, $Re_l = 2.0{\times}10^6$, $\alpha = -0.2°$, $\varphi = -90°$, *Sph_Grid_0C-Adapt*. There is minimal difference between the computed pressure distribution for the laminar and turbulent boundary layer over the upstream 60% of the spheroid.

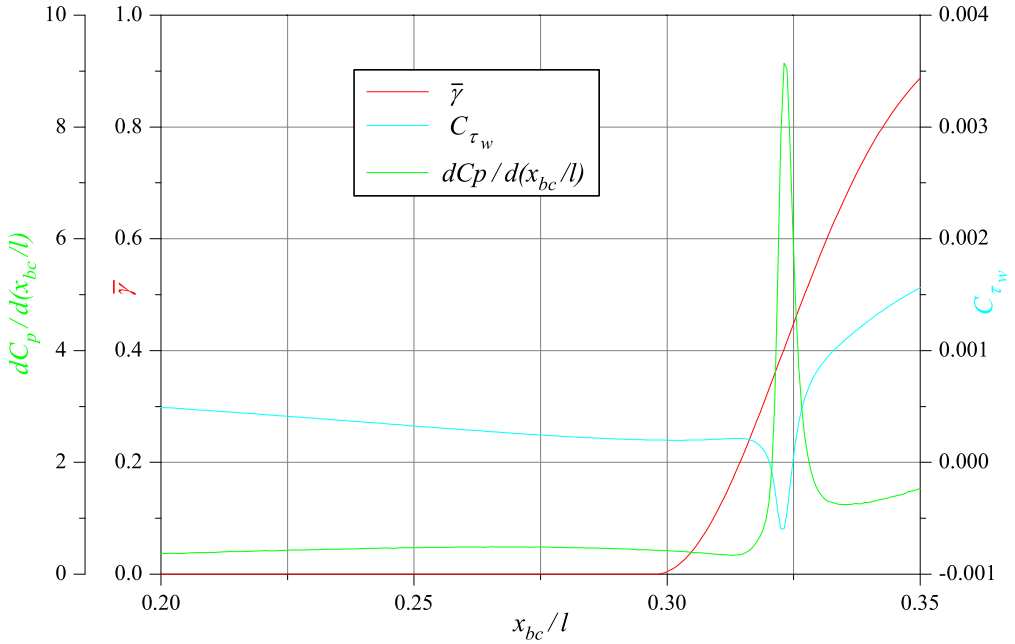

Figure 9.22: Computed wall shear stress and surface pressure gradient on the spheroid, $\alpha = -0.2°$, realisable k-ε turbulence model, *Sph_Grid_0C-Adapt*. The pressure gradient is seen to increase rapidly near $\bar{\gamma}_{0.20}$, separation occurs at approximately $\bar{\gamma}_{0.35}$.

it is some how accounted for). The slower commencement in the production of k with the SST turbulence model is likely associated with the failure of the boundary layer to reattach for this incidence for $Re_l = 2.0 \times 10^6$. The other notable difference between the results of the realizable k-ε and the SST turbulence models is the greater maximum shear stress calculated by the former with and without the implemented laminar transition (Figs. 9.23 and 9.24).

With boundary layer transition implemented the shear stress coefficient at $\varphi = -90°$ in Fig. 9.23 shows turbulent boundary layer separation occurs for the realisable $k-\varepsilon$ and the SST model at $x_{bc}/l \approx 0.45$, a short distance downstream from the location determined by both fully turbulent cases ($x_{bc}/l \approx 0.44$). Near the stagnation point ($x_{bc}/l = -0.5$) with the turbulence model implemented in this region the shape factor calculated from the boundary layer with the SST model behaves initially in a manner closer to that of the laminar region while the dissipation of turbulent kinetic energy exceeds its production. The location of turbulent boundary layer separation is within the range of $x_{bc}/l = 0.43$ to 0.46 seen in the surface flow visualisation (Fig. 7.15) at a similar Reynolds Number ($Re_l = 4.0 \times 10^6$). The results from the surface pressure measurement[4] at $Re_l = 3.0 \times 10^6$, for this incidence, show a separation in the

[4]The results of the surface pressure distribution for this incidence at $Re_l = 3.5 \times 10^6$ displayed boundary layer transition near the front of the body. This is believed to be due to perturbations from a pressure tapping hole.

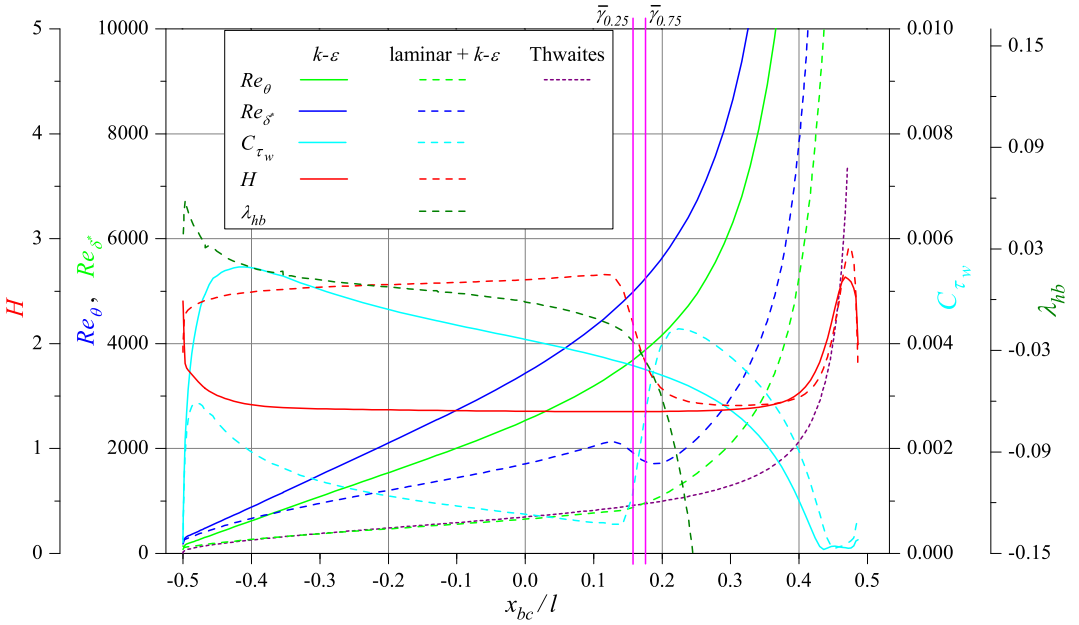

(a) realisable k-ε

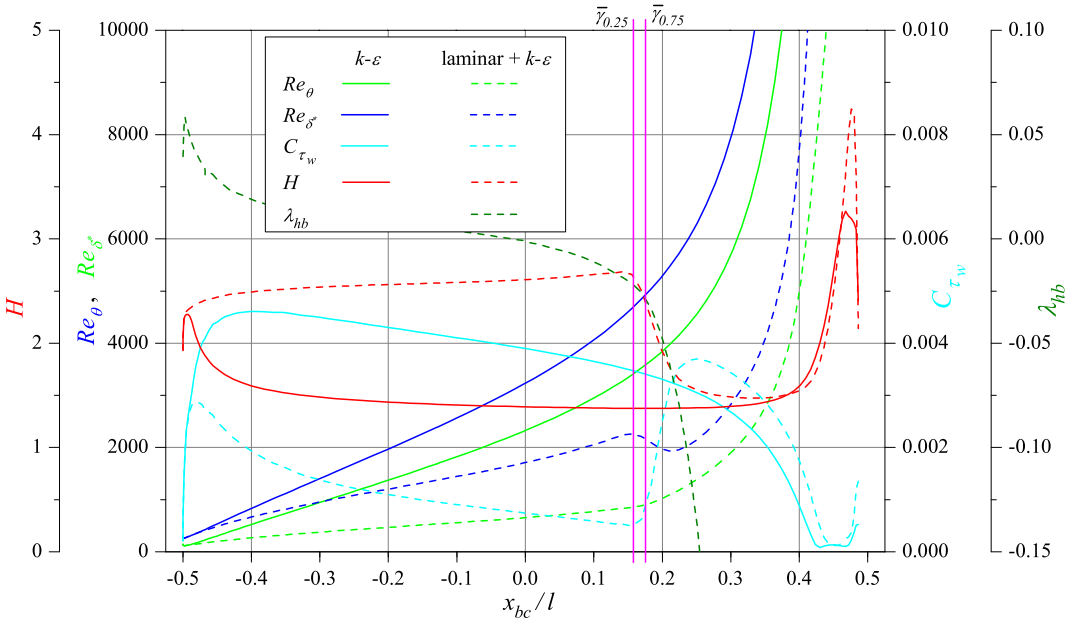

(b) SST

Figure 9.23: Boundary layer properties for approximately axisymmetric flow on 3–1 spheroid using two equation turbulence models with and without laminar regions using *Sph_Grid_0A* for $Re_l = 3.5 \times 10^6$, $\alpha = -0.2°$, $\varphi = -90°$. Mangler transformation of Thwaites method solved for axisymmetric flow using velocity distribution from classical potential theory on an ideal spheroid at $Re_l = 3.5 \times 10^6$. The values for momentum thickness obtained using Thwaites method and the finite volume code show good agreement in regions of laminar flow. The values of the shape factor appear reasonable. The wall shear stress is greater when using the realisable k-ε than it is when using the SST turbulence model. Location of $\bar{\gamma}_{0.25}$ and $\bar{\gamma}_{0.75}$ from FRTPP measurements.

range $0.44 < x_{bc}/l < 0.47$ (Fig. 4.5(c)).

Calculated surface streamlines and contours of shear stress coefficient are shown in Fig. 9.25. This figure shows the additional grid resolution required when a separation bubble was present has negligible influence on the surface streamlines when transition is implemented in the absence of boundary layer separation. The axial location of boundary layer separation is relatively axisymmetric, occurring slightly upstream when the boundary layer transition is also upstream as evidenced by the increase in wall shear stress in Fig. 9.25. The wall shear stress maximum along a streamline is less when boundary layer transition occurs further downstream in the region of flow deceleration due to the body curvature. The surface streamline and separation location calculated using the SST turbulence model with the same laminar region is very close to that calculated using the realizable k-ε at this Reynolds number. Surface pressure coefficient measurements for a range of Reynolds numbers and the calculated surface pressure coefficient at $Re_l = 3.5 \times 10^6$ are compared in Fig. 9.26. The location of the transition region used for the computations was determined from the boundary layer survey and was upstream of the location estimated from the surface pressure measurements at $Re_l = 2.5 \times 10^6$ and 3.0×10^6. The estimated transition region from the surface pressure measurements in Fig. 9.26 does not include the result for $Re_l = 3.5 \times 10^6$; however it is reasonable to expect transition to occur a relatively short distance upstream of the locations for $Re_l = 2.5 \times 10^6$ and $Re_l = 3.0 \times 10^6$.

Upstream of the region where boundary layer transition has been set for the computations the computed C_p values tends to be marginally less than the measured values (Fig. 9.26). Downstream of the transition region set for the computations (determined from the boundary layer survey), but still upstream of the region where the surface pressure measurements appear to show transition, the computed surface pressure values appear to be very close to those measured. The overall shift in computed surface pressure after transition is less than seen in the measurements; this is further examined in the following Subsection. As seen with the boundary layer properties in the transition region at this Reynolds number the surface pressure coefficient distribution for the two meshes using the realizable k-ε are similar, with the greater resolution of *Sph_Grid_0B-Adapt* showing a slightly larger perturbation. The results for the SST model show a more gradual shift.

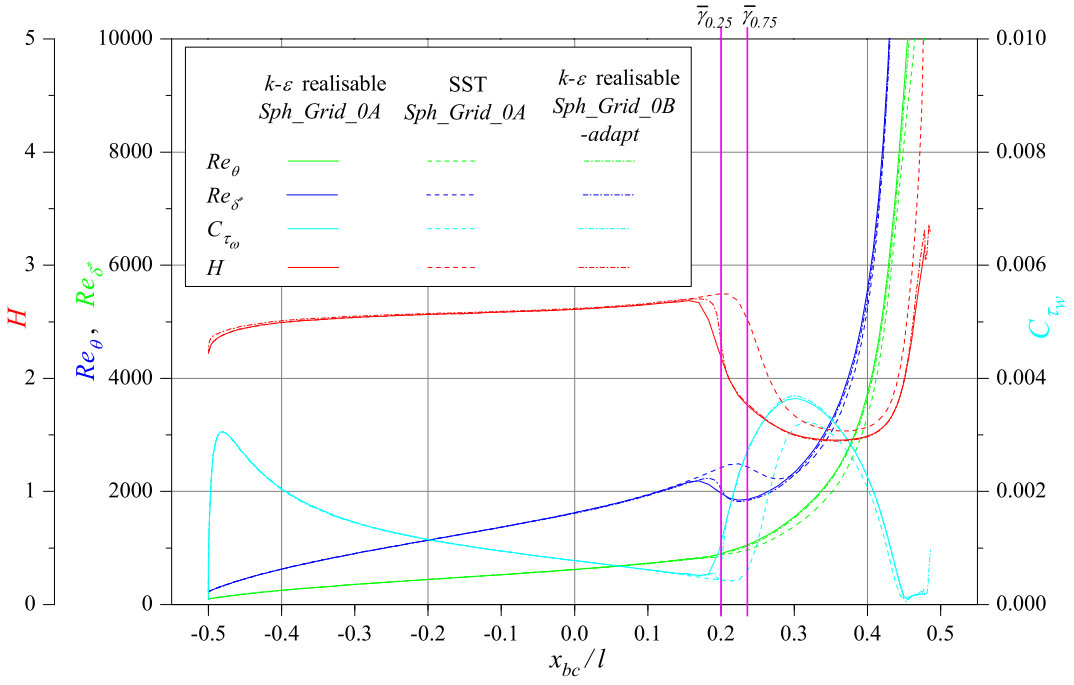

(a) $\varphi = -30°$

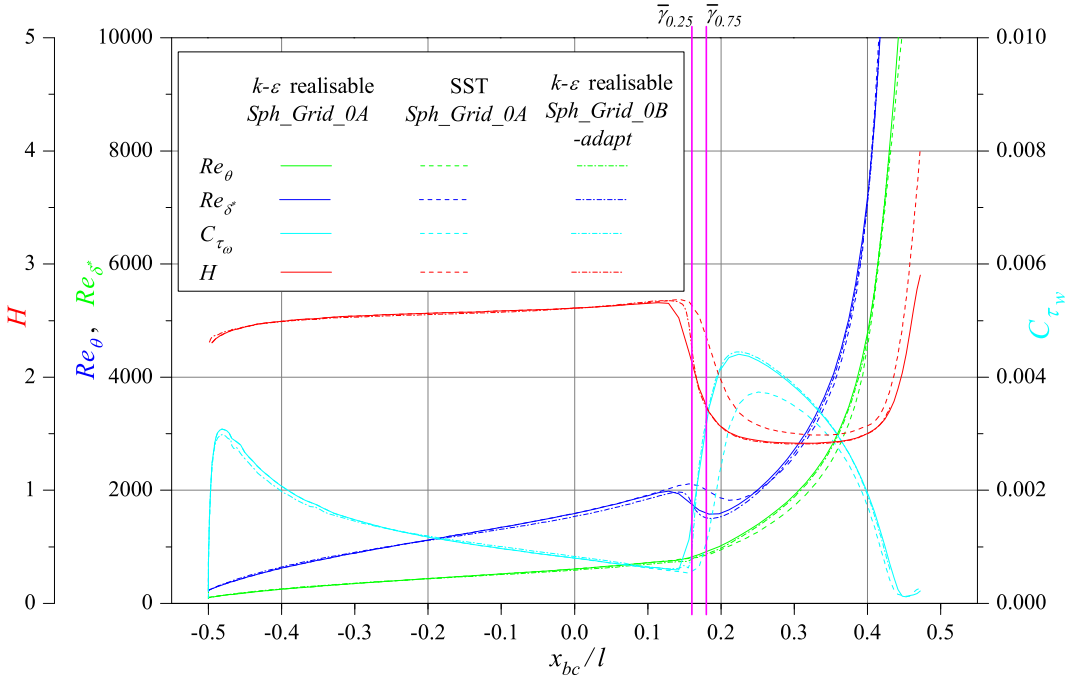

(b) $\varphi = -90°$

Figure 9.24: Boundary layer properties for approximately axisymmetric flow on 3–1 spheroid using realisable k-ε and SST turbulence models, $Re_l = 3.5 \times 10^6$, $\alpha = -0.2°$. Boundary layer properties at this Reynolds number are similar for both meshes and turbulence models. For the SST model compared to the realisable k-ε model the most notable differences are the lower wall stress in the turbulent region and its slower switch to the expected turbulent behaviour. (e.g. the increase in momentum thickness, the dip then increase in displacement thickness, the drop in H to approximately 1.5.) Location of $\bar{\gamma}_{0.25}$ and $\bar{\gamma}_{0.75}$ from FRTPP measurements.

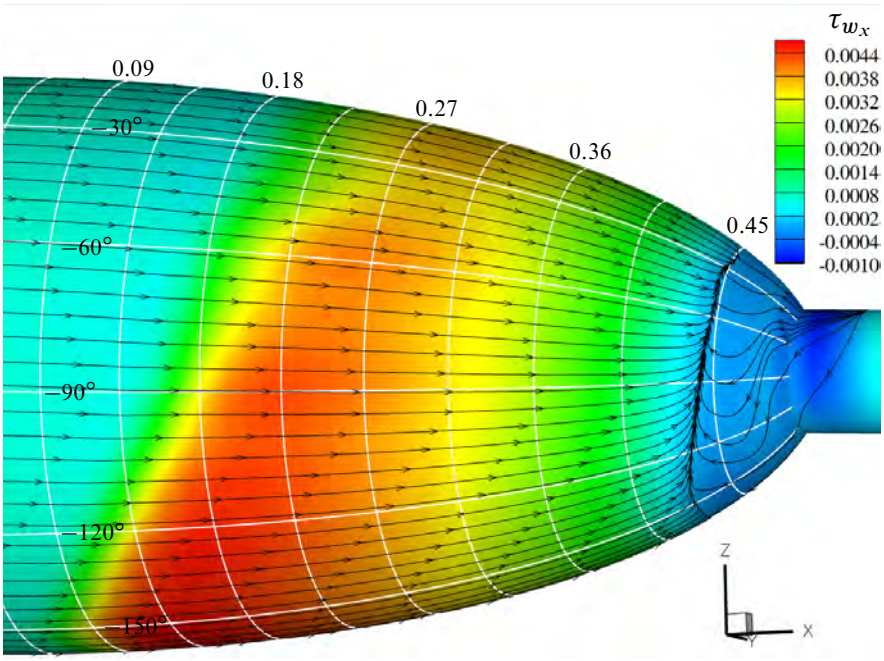

(a) *Sph_Grid_0A*

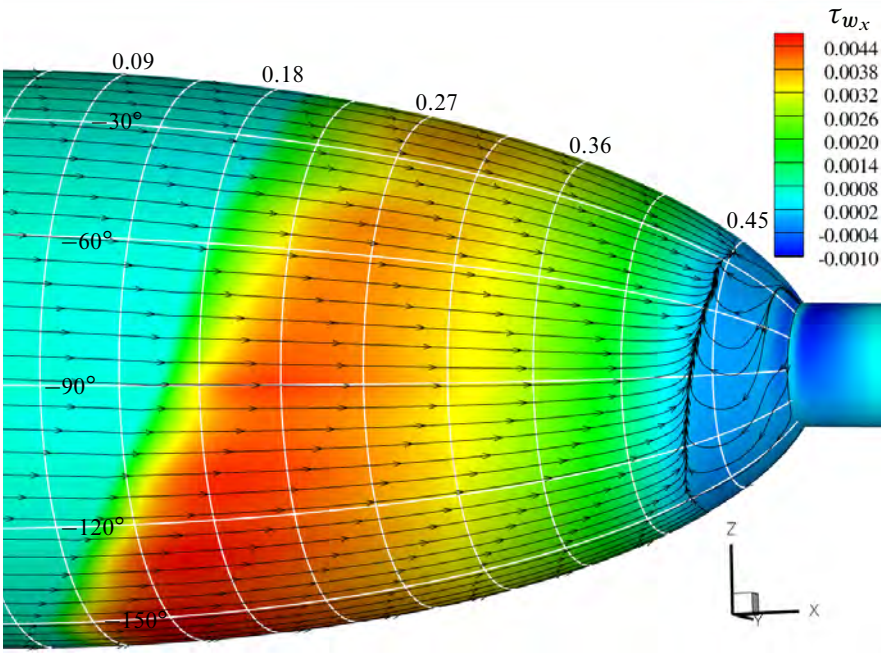

(b) *Sph_Grid_0B-Adapt*

Figure 9.25: Computed surface streamlines on 3–1 spheroid using realisable k-ε with laminar regions, $Re_l = 3.5 \times 10^6$, $\alpha = -0.2°$. Comparison between the streamlines shows grid independence in the location of boundary layer separation. Contours of wall shear stress in the x_{bc} direction show negligible difference between the solution obtained using grid *Sph_Grid_0A* and *Sph_Grid_0B-Adapt*.

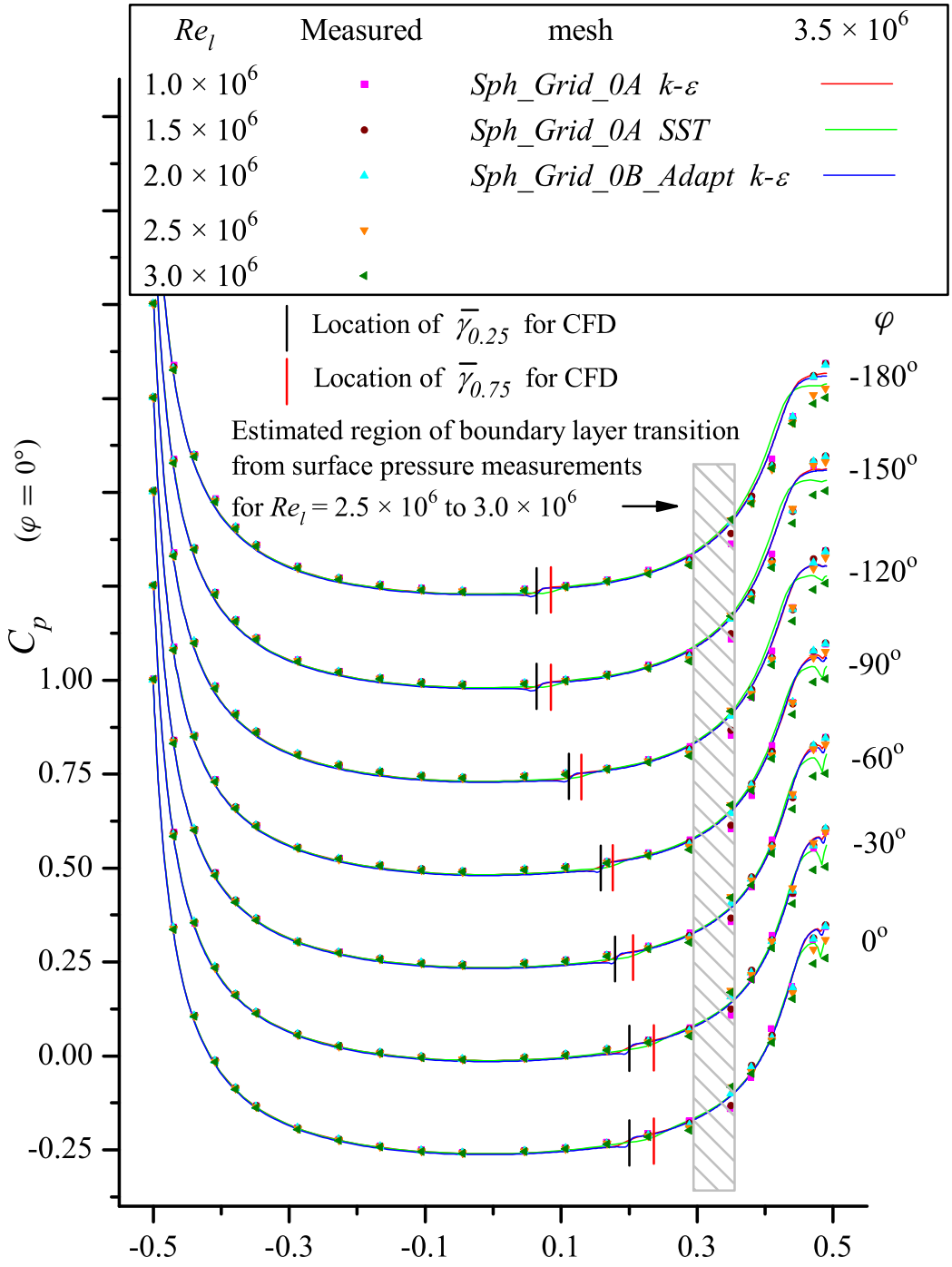

Figure 9.26: Computed and measured surface pressure distribution on spheroid, $\alpha = -0.2°$, realisable k-ε turbulence model. C_p values for each azimuth progressively displaced by 0.25 for $\varphi < 0°$. Results for the lower resolution mesh display a reduced base pressure. Location of $\bar{\gamma}_{0.25}$ and $\bar{\gamma}_{0.75}$ determined from boundary layer survey.

9.3 Results and Discussions $\alpha = -10.2°$

9.3.1 $Re_l = 2.0 \times 10^6$

Contamination of the spheroid surface for this Reynolds number resulted in the boundary layer survey being discarded. Fortunately for this Reynolds number the flow visualisation provides an indication of the boundary layer transition between $\varphi = 0°$ and $-90°$. The location of boundary layer transition was estimated from the increased scouring of the oil apparent in Fig. 7.9. The increased scouring in this case is associated with the greater wall shear present in a turbulent boundary layer. Other photos (Fig. 7.10) at this Reynolds number using a less viscous oil suggest that for φ between 0° and approximately $-45°$ a very short laminar separation bubble exists at the transition region. This laminar separation bubble is not picked up by the surface pressure measurements due to the relatively coarse placement of tappings. Excellent agreement between the flow visualisation and surface pressure measurements for the location of boundary layer transition is shown in Fig. 7.9. This provides confidence in the application of the transition location obtained from the surface pressure measurements to the computational work for this case. Neither the flow visualisation nor the surface pressure measurements allow the length of the transition region to be determined, which for the purpose of this computation was taken as $10\,mm$ between $\bar{\gamma}_{0.25}$ and $\bar{\gamma}_{0.75}$. This length is consistent with the short transition length seen at $\alpha = 6.2°$ for this Reynolds number.

The streamlines and wall shear stress calculated using the realisable k-ε turbulence model with mesh *Sph_Grid-10A* and *Sph_Grid-10C-Adapt* in Fig. 9.27 show very similar surface streamlines. The computed surface streamlines are visibly influenced by the location of boundary layer transition, most notably when the surface streamlines and the boundary layer transition zone meet at a glancing angle. Given these surface streamlines are calculated from the surface shear stress and this shear increases in the transition from a laminar to turbulent boundary layer (assuming the boundary layer stays attached) some level of interaction is expected. To examine the sensitivity of this interaction to the distance over which the transition is implemented the length of the transitional zone, $\bar{\gamma}_{0.25}$ to $\bar{\gamma}_{0.75}$, was increased from $10mm$ to $25mm$. This change resulted in negligible change in the surface streamlines. Unaccounted for is the temporal aspect of transition. The time averaged implementation of the transition process does not model the coherent structures that exist in intermittently and fully turbulent shear layer regions. The flow visualisation shows possible interaction between the surface streamlines and the estimated transition region near $x_{bc}/l = -0.2$ for φ between $-90°$ and $-105°$ in Fig. 7.9(a) and near $x_{bc}/l = -0.1$ for φ between $-105°$ and $-140°$ in Fig. 7.9(b).

Overall the computed surface streamlines on the flank and pressure side at the rear do not reflect those seen in the flow visualisation (Fig. 7.9 and 7.10). The surface streamlines

on the pressure side ($0° \geqslant \varphi \geqslant -60°$) show flow separation, without reattachment, occurring at $x_{bc}/l \approx 0.37$, upstream of the transition region. The flow visualisation shows a short separation bubble (Fig. 7.10) with the reattached flow finally separating at $x_{bc}/l \approx 0.48$ for $0° \geqslant \varphi \geqslant -60°$. This observation is supported by the surface pressure distributions that indicate that for $0° \geqslant \varphi \geqslant -45°$ the flow was still attached at the final on-body tapping ($x_{bc}/l \approx 0.47$). Increasing the mesh resolution in this case appeared to have minimal influence on the surface streamlines in contrast to the case for this Reynolds number at $\alpha = -0.2°$. The major computed vortical structure on the flank of the body rotates in the opposite direction to the structure in the photo; it is also positioned further upstream. The flow visualisation shows no funnelling of the flow into the vortical structure from fluid on the flank ($\varphi = -75°$ to $120°$) of the body as depicted in Fig. 9.27. Fig. 9.28 however shows that the increased mesh resolution did result in a change in surface pressure distribution on the pressure side at the rear of the body. Increasing the mesh density from *Sph_Grid-10C* to *Sph_Grid-10C-Adapt* resulted in minimal change in C_p, so further increase in resolution was not performed.

The difficulty that this technique of predefining the boundary layer transition region has with premature separation of the laminar boundary layer, apparent for this Reynolds number at $\alpha = -0.2°$, also occurs in these computations. Shifting the predefined turbulent region upstream for $0° \geqslant \varphi \geqslant -60°$ so $\bar{\gamma}_{0.25}$ occurs at $x_{bc}/l \approx 0.38$ instead of 0.43 prevents the laminar separation; the turbulent boundary layer for these azimuthal angles is attached until $x_{bc}/l \approx 0.45$ (Fig. 9.3.1). The surface C_p distributions for $0° \geqslant \varphi \geqslant -30°$ when the laminar separation is prevented provided a close match to the measured data. The pressure recovery calculated near the rear of the model on the suction side is greater than measured as the turbulent boundary layer is predicted to separate later than shown in the flow visualisation (Fig. 9.3.1) or inferred from the surface pressure measurements.

9.3.2 Flow Visualisation at $Re_l = 4.0 \times 10^6$

Surface flow visualisation of the spheroid at $\alpha = -10.2°$ and $Re_l = 4.0 \times 10^6$ is shown in Fig. 7.11. The surface streamlines calculated for the corresponding conditions using the realisable k-ε model and the SST model are displayed in Figs. 9.30. The calculated surface streamlines for both models predict the large separated region on the side of the model and the attached flow persisting to almost the base of the model on the suction side. The width of this attached flow appears to be more accurately calculated by the realisable model, which gives only a marginal over prediction. Neither model predicts the flow to stay attached until the base of the model for $0° \geqslant \varphi \geqslant -30°$, as seen in Fig. 7.11. On the pressure side the realisable model predicts the flow will stay attached in this region of strong adverse pressure gradient marginally longer

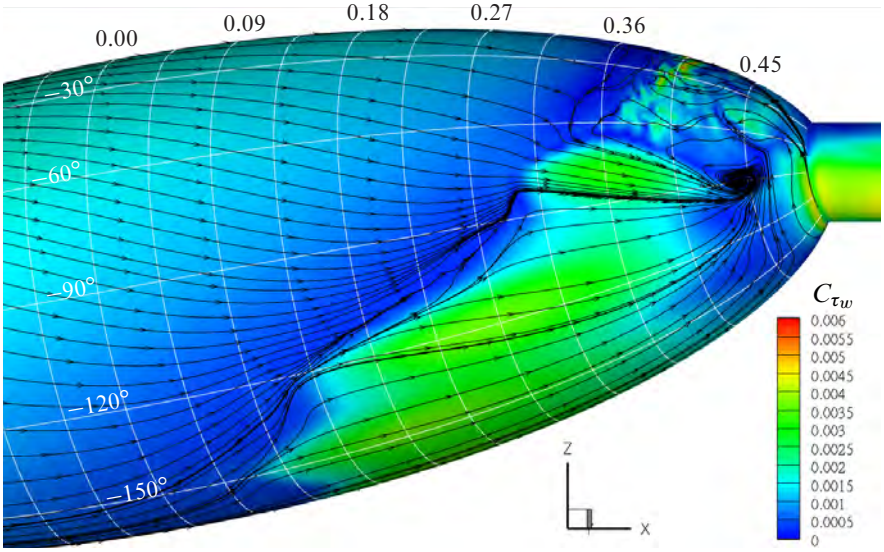

(a) *Sph_Grid-10A*, Contours of C_{τ_w}

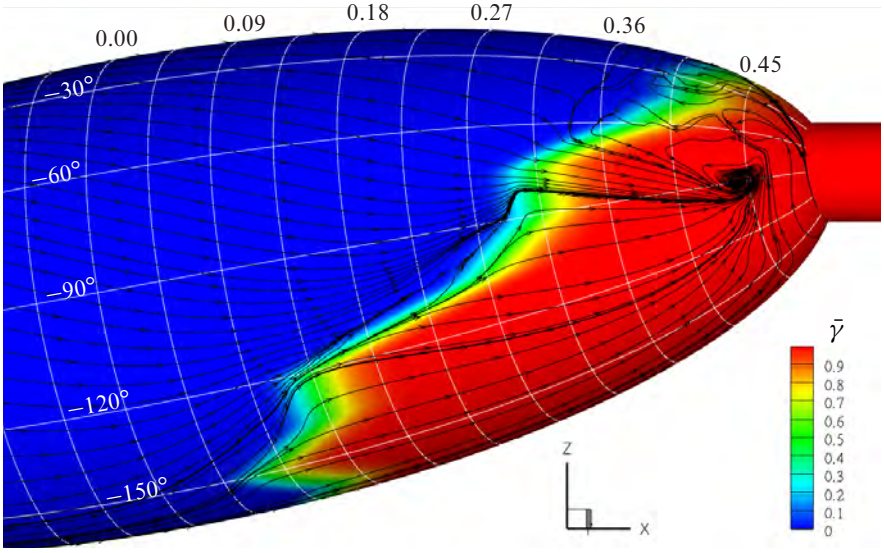

(b) *Sph_Grid-10C-Adapt*, Contours of time averaged intermittency, $\bar{\gamma}$

Figure 9.27: Computed surface streamlines on 3–1 spheroid using realisable k-ε with laminar regions, $Re_l = 2.0 \times 10^6$, $\alpha = -10.2°$. Comparison of the streamlines show that refining the grid has not resulted in any significant change in the calculated surface pattern in the region where a separation bubble was noted in the flow visualisation ($0° \geqslant \varphi \geqslant -45°$).

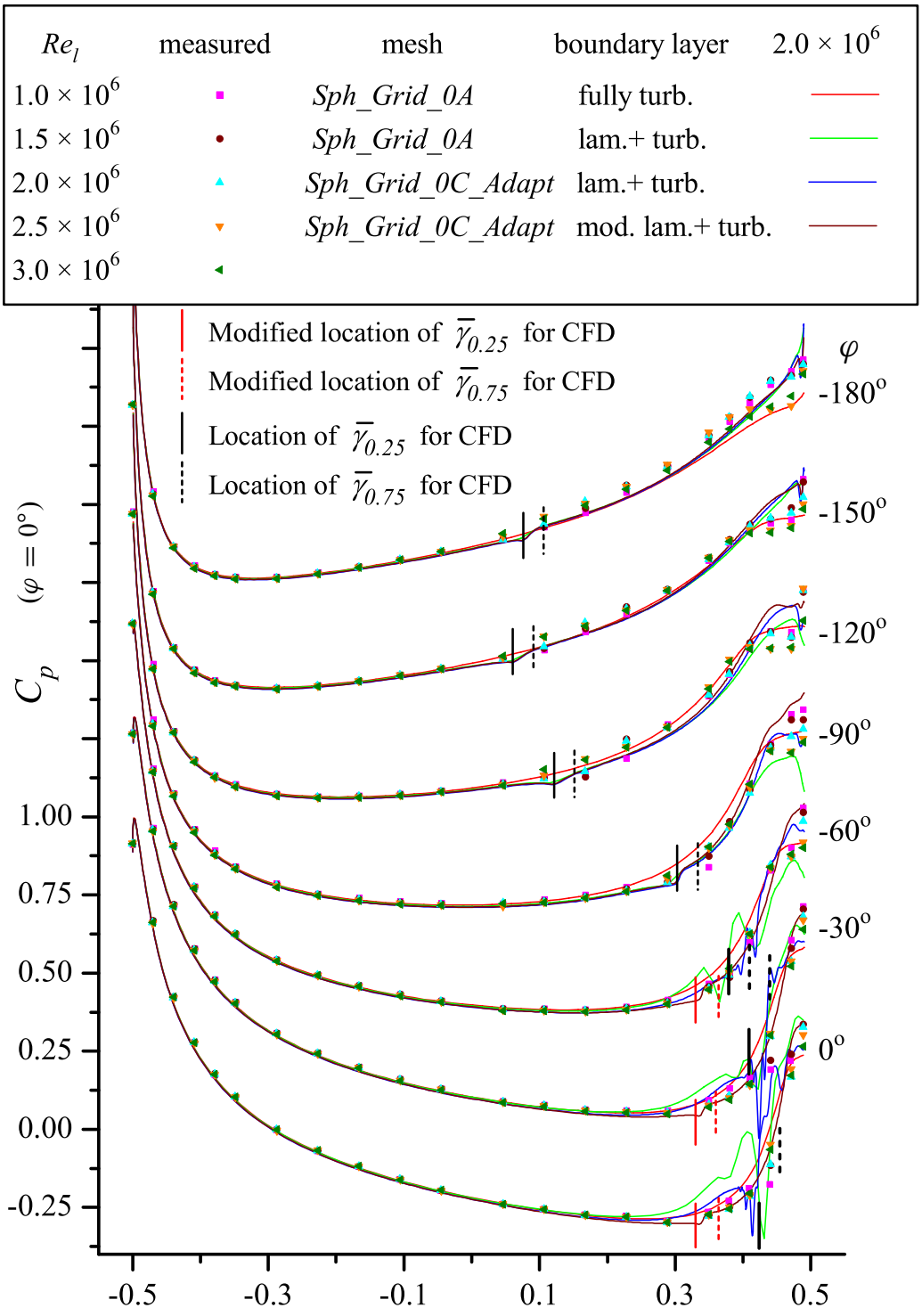

Figure 9.28: Computed and measured surface pressure distributions on the spheroid, $\alpha = -10.2°$, realisable k-ε turbulence model. C_p values for each azimuth progressively displaced by 0.35 for $\varphi < 0°$. Shifting the transition zone forward on the pressure side in order to avoid a laminar separation resulted in closer match to the measured data for these azimuths. On the suction side all but the fully turbulent case calculated an excess length of attached flow leading to a greater than measured pressure recovery.

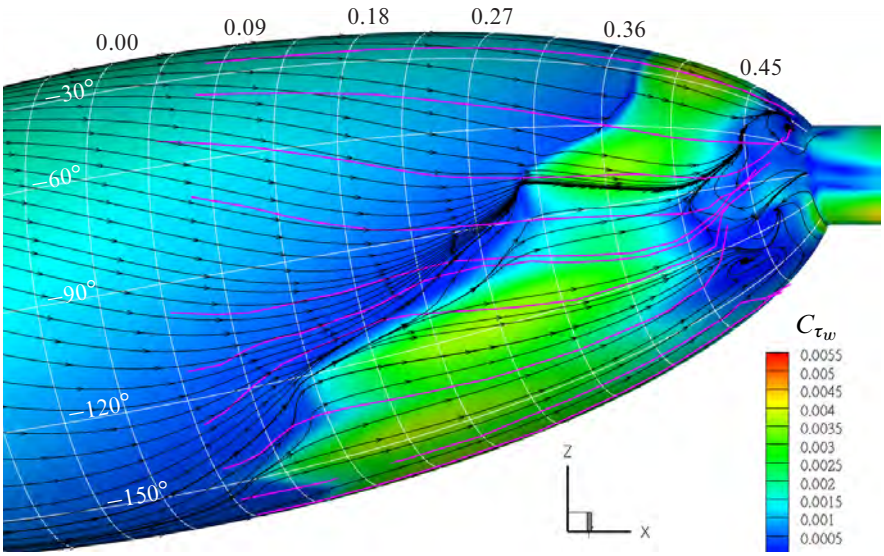

Figure 9.29: Computed and measured surface streamlines and contours of shear stress on the spheroid, $\alpha = -10.2°$, realisable k-ε turbulence model with laminar zone modified to prevent laminar flow separation on the suction side. Both measured and calculated surface streamlines show disturbances that are attributed to the increased surface shear stress associated with the start of the turbulent boundary layer.

than predicted by the SST model. A rapid rise in wall shear stress for both turbulence models is observed near the front of the model. It occurs within the first 5% of the model length on the suction side and within the first 15% on the pressure side. As noted in Subsection 9.2.2 the increase in surface shear is more rapid and greater with the realisable model. This surface shear increase due to the turbulence model may play a significant role by directly contributing to the viscous drag and/or indirectly by thickening the boundary layer and influencing the boundary layer separation.

The surface streamlines calculated using the realisable k-ε turbulence model, with the measured laminar region implemented are shown in Fig. 9.31(a). They indicate attached flow further downstream on the pressure side than that predicted without allowing for the laminar region of the boundary layer, Fig. 9.30(a). A delay in separation is consistent with the thinner boundary layer expected due to the reduced length of turbulent boundary layer flow. The separated region on the flank and suction side of the model is of a similar area to that seen in the flow visualisation but located closer to the suction side of the symmetry plane. (The saddle of this separation is calculated at $x_{bc}/l \approx 0.42$, $\varphi \approx -145°$; the flow visualisation shows this saddle to be at $x_{bc}/l \approx 0.40$, $\varphi \approx -120°$.) The tongue of attached flow on the suction side still reaches almost to the sting, but is now narrower than that seen in the flow visualisation.

The results for the SST model with the modification for boundary layer state appeared worse, with boundary layer separation being predicted on the pressure side near the start

of the boundary layer transition. This premature separation on the pressure side is again explained by the slower switching on of the turbulence in the SST model, even though separation occurs before the transition region due to the strong coupling between the boundary layer state, separation and pressure. The slow switch on and subsequent separation in this case is exacerbated by the increasingly adverse pressure gradient at the rear of the model for $0° \geqslant \varphi \geqslant -30°$. On the flank and suction side the surface streamlines calculated using the SST turbulence model without any laminar regions shows minimal separation on the rear.

While the attachment of the flow near the pressure side of the symmetry plane is not correctly calculated it is difficult to draw any conclusion as the relatively high momentum of the attached flow may have a significant influence on the low energy separated region on the flank. The flow leaving the model at the body-sting junction will also influence the base pressure. In this case there is not an appreciable improvement in the calculation of the surface streamlines when using the predefined laminar regions. However, from Figs. 9.30 and 9.31 the surface shear stress is significantly less with the laminar region implemented.

The deviations in the surface streamlines when approaching the region of boundary layer transition in these calculations appears less than that at this incidence when $Re_l = 2.0 \times 10^6$. The thinner boundary layers and the upstream shift in the location of transition[5] will result in greater momentum in the wall layer, so the direction of the surface streamlines is less influenced by the increase in shear stress due to boundary layer transition.

9.3.3 Surface Pressure at $Re_l = 4.0 \times 10^6$

The calculated surface pressure distributions for $Re_l = 4.0 \times 10^6$ along with the measured distributions for $Re_l = 1.5 \times 10^6$ to 3.5×10^6 are compared in Fig. 9.32. There is minimal differences over the front half of the model between the computed C_p with either laminar or turbulent boundary layer cases. The computed C_p values in this region closely match those measured for $Re_l = 1.5 \times 10^6$ to 3.5×10^6 with a laminar boundary layer. (Note that for the measured data at $\varphi = -180°$, $Re_l = 3.5 \times 10^6$ the boundary layer has transitioned near the nose.) For $-120° \geqslant \varphi \geqslant -180°$ the results computed with the boundary layer transition display a perturbation in the vicinity of the transition region, but then return to a pressure distribution almost identical to that of the fully turbulent calculation. The positive shift observed in the measured surface pressure distribution near the location of boundary layer transition for this incidence and azimuthal angles (Figs. 4.9(b), 4.11(b), and 9.32) is not observed in these calculations with the implemented laminar and transitional regions. Due to the sensitive nature of boundary layer transition, its locations determined from the boundary layer survey and estimated from

[5] Upstream the boundary layer is thinner as the pressure gradient due to surface curvature is less adverse and the boundary layer has less distance to thicken.

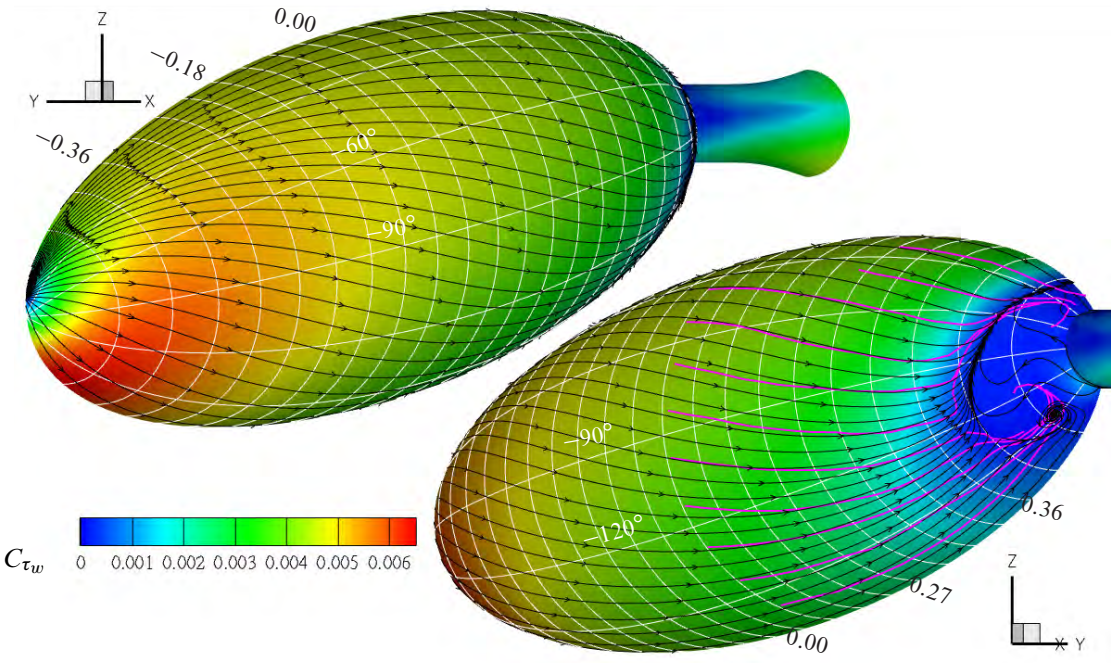

(a) realisable k-ε turbulence model

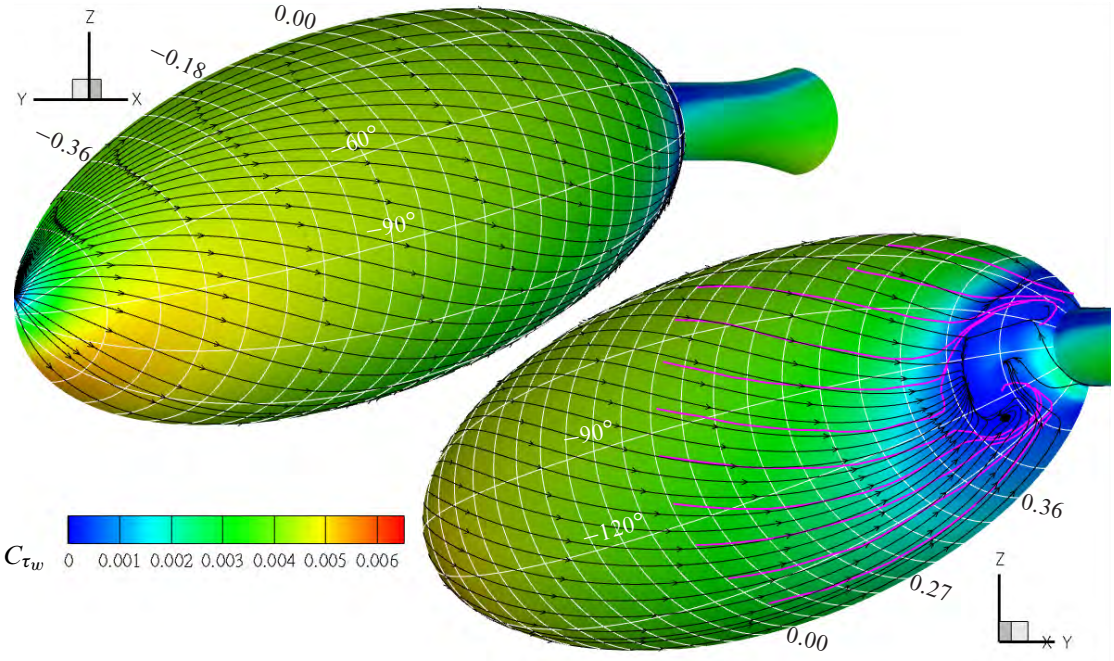

(b) SST turbulence model

Figure 9.30: Computed surface streamlines and contours of C_{τ_w} on the 3–1 spheroid using turbulence models without laminar regions, $Re_l = 4.0 \times 10^6$, $\alpha = -10.2°$, *Sph_Grid-10A*. Greater surface shear stress is apparent with realisable k-ε turbulence model. Both turbulence models show boundary layer separation near $x_{bc}/l = 0.45$ on the pressure side. On the flank and suction side both turbulence models under predict the size of the separation near the base; but the realisable k-ε turbulence model only marginally. Magenta lines show surface streamlines determined from the flow visualisation for the corresponding incidence and Reynolds number.

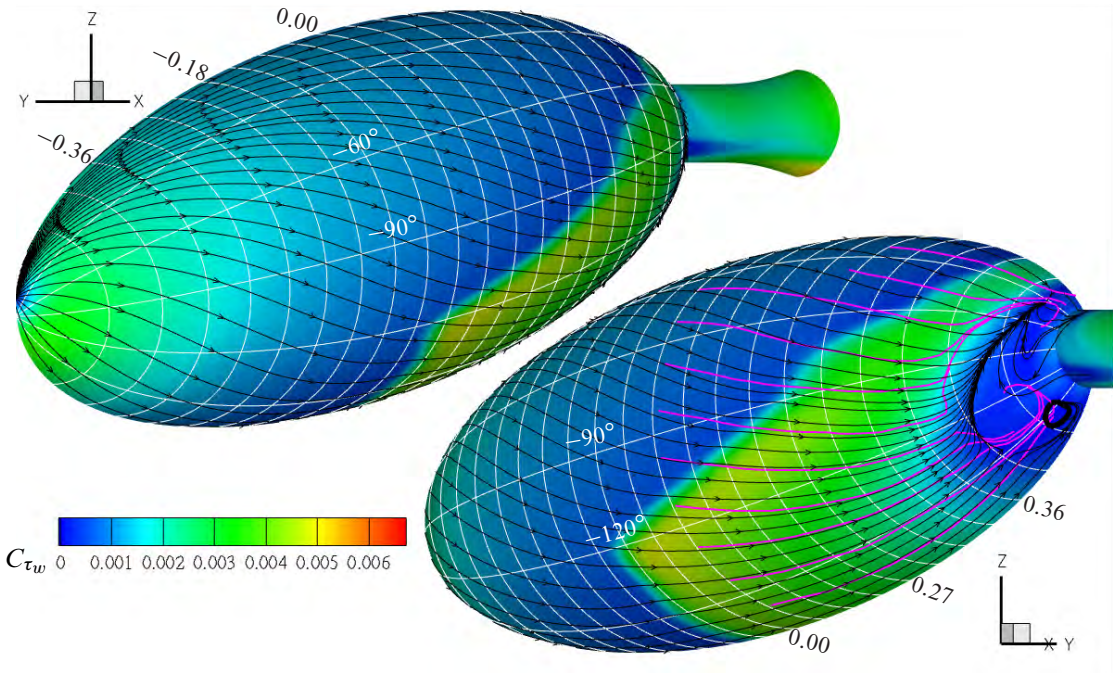

(a) realisable k-ε turbulence model.

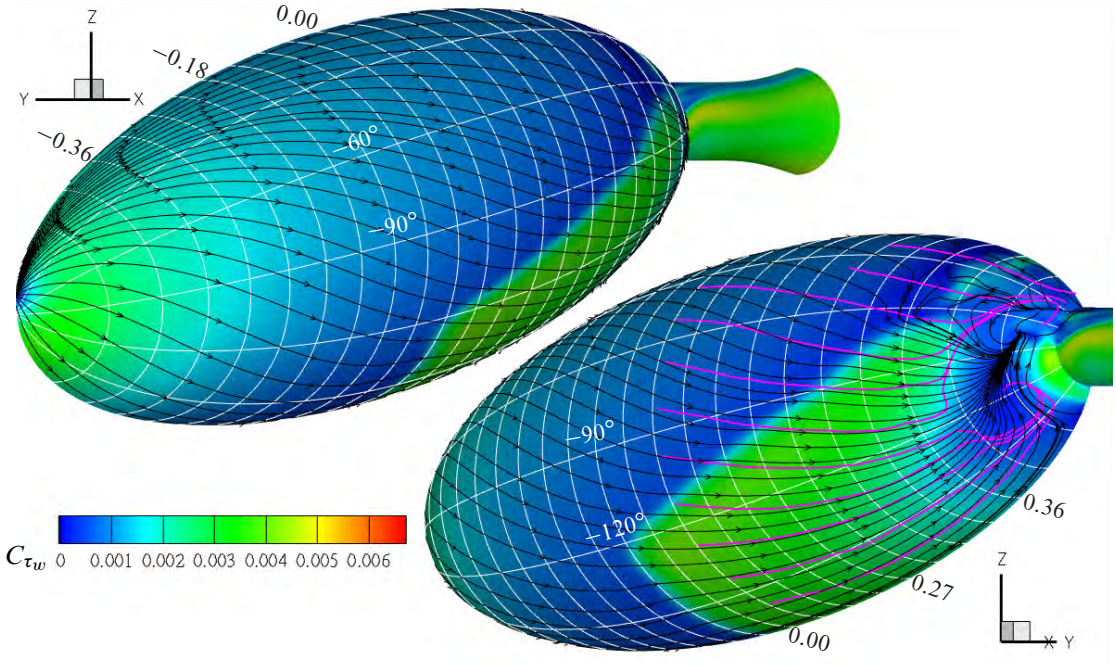

(b) SST turbulence model

Figure 9.31: Computed surface streamlines on spheroid using turbulence models with laminar regions, contours of C_{τ_w} when $Re_l = 4.0 \times 10^6$, $\alpha = -10.2°$. The magnitude and area of high surface shear stress is considerably reduced from that seen in Fig. 9.30 where no laminar region was implemented. Magenta lines show surface streamlines determined from the flow visualisation for the corresponding incidence and Reynolds number.

the surface pressure measurements may not always coincide as these tests were performed during different setups (Fig. 9.32). It should also be recalled that the most downstream surface pressure measurement is from the annular tap formed by the gap between the model and sting, and thus is not expected to match the calculated values at this location but should be close to an average across all the azimuths.

Allowing for the laminar region in the calculations at $Re_l = 4.0 \times 10^6$ does not appear to result in an overall closer match with the measured surface pressure distributions at $Re_l = 3.0 \times 10^6$ and 3.5×10^6. The calculations with the laminar region result in an improved prediction on the pressure side but a poorer prediction on the suction side. The later separation of the turbulent boundary layer and the associated increase in base pressure when the laminar region is implemented is expected due to the thinner boundary layers. The failure of the calculations using the laminar region to accurately determine the location of separation near $\varphi = -90°$ is of significance as this alters the base pressure and thus influences the calculated surface pressure at all the other azimuths. Given the calculations using the SST turbulence model with the laminar region implemented displayed boundary layer separation without reattachment prior to the transition region on the suction side, the surface pressure measurements for this instance are not discussed.

9.3.4 Cross Flow Influence on the Boundary Layer

The ratio of crossflow displacement thickness, $\delta^*_{y_\Lambda}$, (second term in Eq. 9.9) to streamwise displacement thickness, $\delta^*_{x_\Lambda}$, (first term in Eq. 9.9) is shown in Fig. 9.33. This figure also shows the surface streamlines calculated from the surface shear stress and pseudo streamlines showing the flow direction 30 μm off the surface. Caution is warranted in drawing conclusions solely from these results, as the calculation of the contribution due to crossflow is subject to errors. The calculation of crossflow through the two planes aligned with external streamlines initially a small distance apart involves a large number of calculations; it terminates with the subtraction of one crossflow volume from the other. This process results in a number often two orders of magnitudes less than the original crossflow volume. Hence an error along either of the planes parallel to the external streamlines may significantly influence the computed magnitude of crossflow displacement thickness. In contrast, the component of displacement thickness due to flow parallel to the streamlines at the boundary layer edge is a function of the boundary layer velocity distribution at that location, and can be computed much more accurately.

Fig. 9.33 shows that the crossflow generally results in an accumulation of fluid between adjacent azimuthal positions where the surface streamlines are converging, and a dispersion of fluid in such regions where they diverge. The dispersion of fluid due to crossflow at the

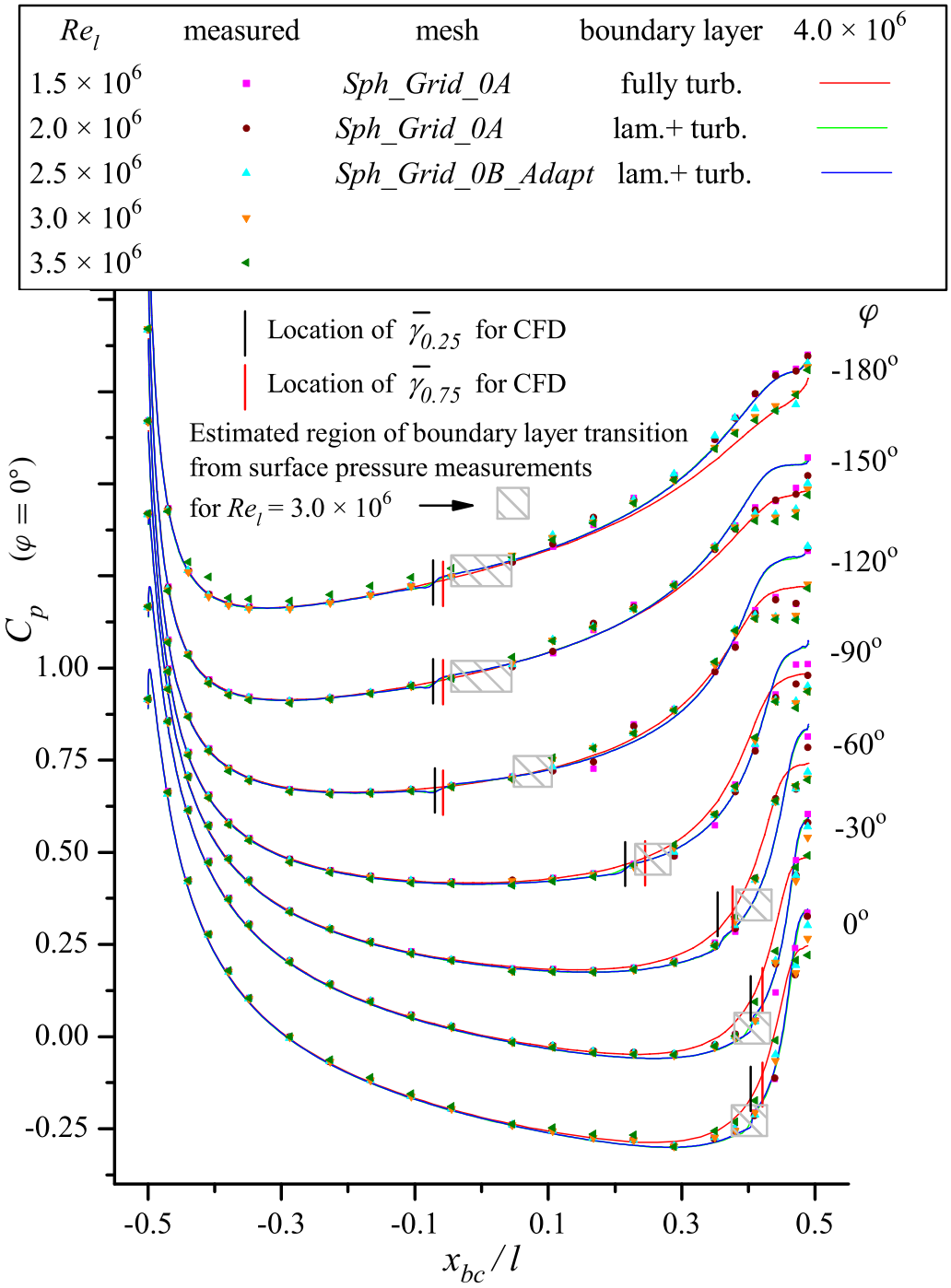

Figure 9.32: Computed and measured surface pressure distribution on spheroid, $\alpha = -10.2°$, realisable k-ε turbulence model. C_p values for each azimuth progressively displaced by 0.25 for $\varphi < 0°$. Implementation of the laminar region has not improved the calculation of the boundary layer separation on the flank and suction side.

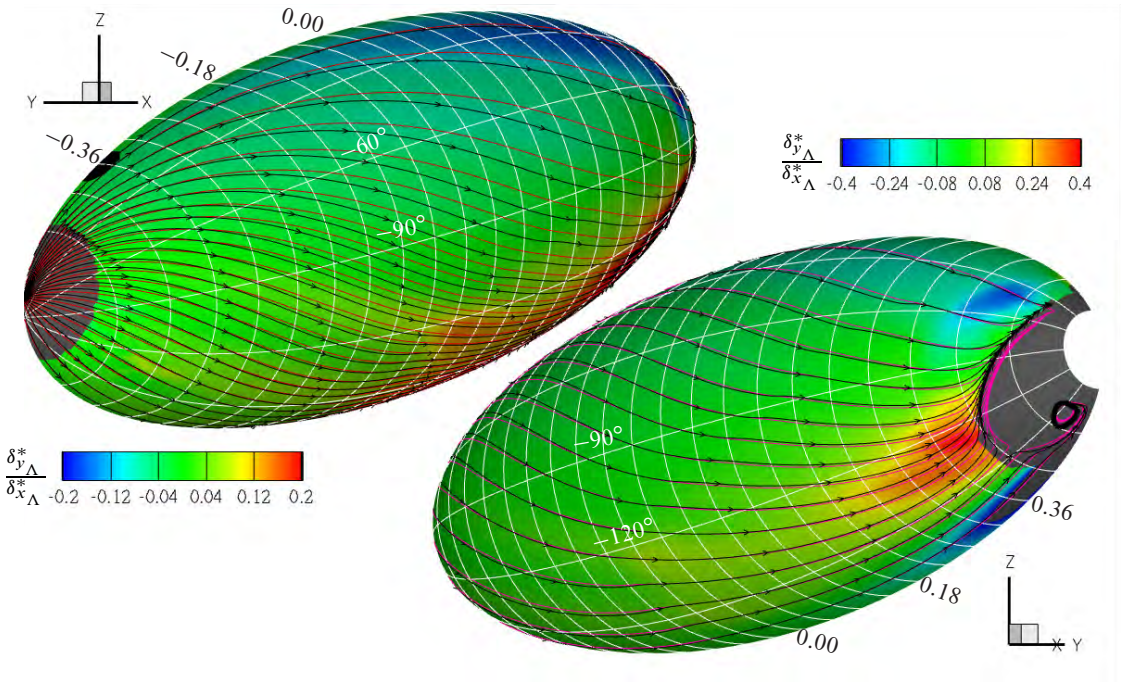

Figure 9.33: Contours of the ratio of crossflow displacement thickness to streamwise displacement thickness, $\alpha = -10.2°$, $Re_l = 4.0 \times 10^6$, realisable k-ε turbulence model with measured laminar region implemented. The contours have been limited in order to show greater resolution over the majority of the model. The crossflow generally results in increased displacement thickness in the region where the surface streamlines (black) are converging and a thinning boundary layer in regions where they diverge. Pseudo streamlines (magenta) show the flow direction 30 μm off the surface. The streamlines on the figure to the upper left and lower right coincide at $x_{bc}/l = -0.36$ and 0.0 respectively.

rear of the model near the suction side of the symmetry plane was initially regarded with suspicion, as large pressure gradients normal to the direction of the external streamlines are not expected near the symmetry plane. This region is, however, subject to a rapidly increasing boundary layer thickness due to an adverse pressure gradient in the streamwise direction caused by the combination of model incidence and surface curvature. The increasing thickness of the boundary layer is shown by the departure of the streamlines at the boundary layer edge from the surface in Fig. 9.34(a). The relatively thick layer of low momentum fluid results in significant crossflow, even though the region has a relatively small pressure gradient in the crossflow direction. Fig. 9.34(b) shows the rapid change in the crossflow vector between the two adjacent planes aligned with the external streamline. The contours of $\partial C_p/\partial(y/l)$ in this figure show a pressure gradient on the surface retarding flow towards the symmetry plane. The range of $\partial C_p/\partial(y/l)$ shown, from 0 to 0.3, is approximately 5% of the full range of ΔC_p calculated on the surface. The thinning of the boundary layer near the symmetry plane on the suction side due to crossflow will prolong boundary layer attachment, particularly as the pressure gradient

has the greatest influence on the direction of the lower momentum flow. This observation, at least in part, provides an explanation for the attachment of the boundary layer close to the base near $\varphi = -180°$. This boundary layer attachment was observed in both the measured and computed results despite the extended length of adverse streamwise pressure gradient. On the suction side near the symmetry plane further downstream ($x_{bc}/l \approx 0.32$), leading up to where the boundary layer separates, the flow has a visible component normal to the surface when examining the velocity vector. This makes the calculation of the displacement thickness in this region unreliable.

The pseudo streamlines in Fig. 9.33 show the flow direction 30 μm off the surface, these pseudo streamlines show notably less disturbance in the vicinity of the boundary layer transition region than seen with the surface streamlines. Disturbances that were observed in the surface flow visualisation (Figs. 7.9(b) and 7.12(b)) appeared to coincide with the region where boundary layer transition was located. These disturbances observed in the flow visualisation are a function of the flow in the vicinity of the surface, due to the finite thickness of the oil mixture. As such they are expected to show less of a disturbance than those seen on the computed surface streamlines that are a function solely of the surface shear stress. It is also worth noting that the disturbances in the flow visualisation were observed in the thicker boundary layer at $Re_l = 2.0 \times 10^6$, rather than in the thinner boundary layer at $Re_l = 4.0 \times 10^6$.

The calculation of momentum thickness in three-dimensional flow is more difficult than that of displacement thickness as momentum is a vector quantity. Should the momentum thickness be based on the absolute momentum in the boundary layer or divided into two components, one parallel to the external streamline, the other normal? Another question is whether the momentum thickness or shape factor are of practical use once calculated? Stock [106] when examining the calculated flow on a 6-1 spheroid uses a momentum thickness based on the external streamline.

Although Menter et al. [92] state that the momentum thickness is strictly a two-dimensional concept there may still be some value in attempting to apply it to three-dimensional flow. If crossflow stability and crossflow separation are neglected and we are interested in an empirical relation between a three-dimensional momentum thickness and both the stability and separation of the boundary layer it may be argued that the momentum in the direction of the flow at the boundary layer edge is relevant. The crossflow transports this streamwise momentum perpendicular to the velocity at the boundary layer edge; a gradient in this crossflow results in an accumulation or dispersion of the low momentum fluid. The streamwise momentum thickness based on the conventional two-dimensional definition is

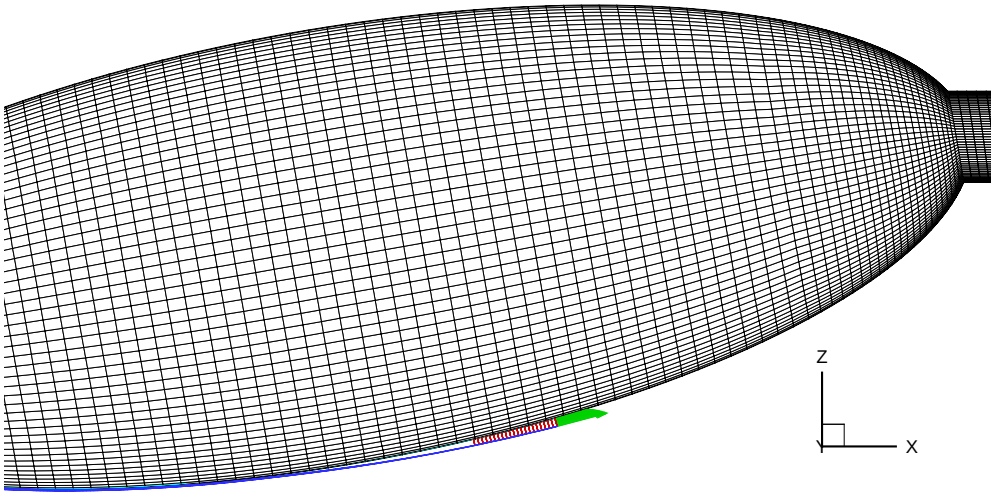

(a) The streamline(s) at the boundary layer edge (blue) close to the symmetry plane on the suction side shows a rapid increase in boundary layer thickness.

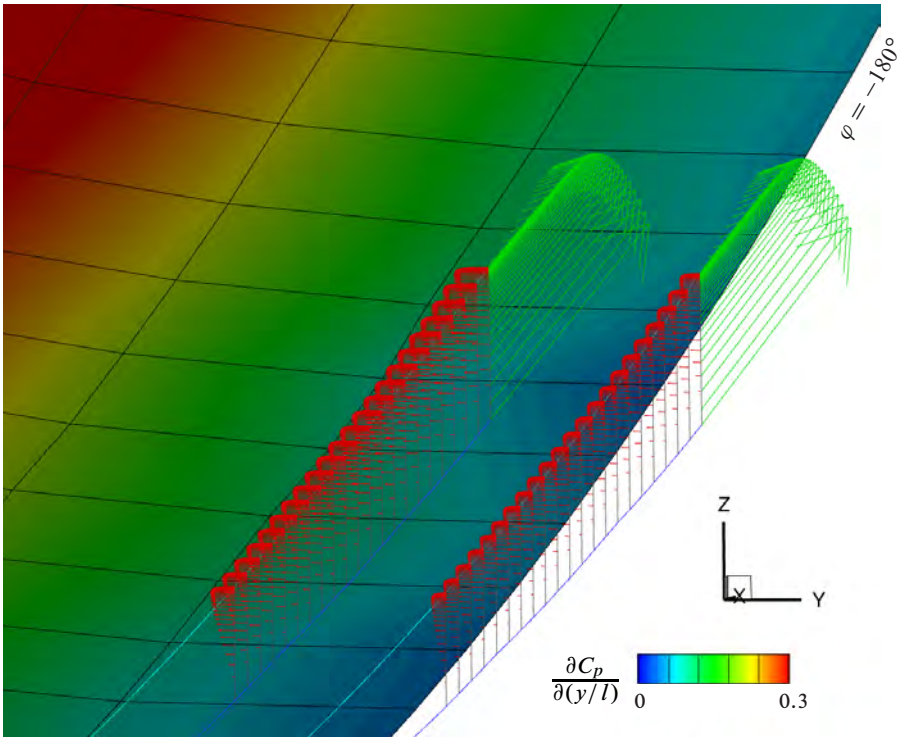

(b) Close up of streamlines in (a), with contours of $\partial C_p/\partial(y/l)$. The crossflow vectors (red) are shown on planes formed by projecting the streamline at the boundary layer edge onto the surface, the projection is normal to the surface. The crossflow vectors are larger on the plane further away from the symmetry plane. On the symmetry plane the crossflow vectors and $\partial C_p/\partial(y/l)$ will be zero. This gradient in the crossflow results in a reduction of the boundary layer thickness in this region. In this figure the crossflow vectors and the vectors parallel to the streamline at the boundary layer edge are of the same scale, in Fig. 9.9 the crossflow vectors were scaled up by a factor of ten.

Figure 9.34: Calculated crossflow on the spheroid at $\alpha = -10.2°$, $Re_l = 4.0 \times 10^6$ on mesh *Sph_Grid-10A*, using the realisable k-ε turbulence model with laminar regions implemented from boundary layer survey.

$$\theta^*_{x_\Lambda} = \frac{1}{U^2_\Lambda} \int_0^\infty u_\Lambda \left(U_\Lambda - u_\Lambda\right) dz \tag{9.12}$$

and the crossflow influence on the streamwise momentum thickness, according to this argument, is

$$\theta^*_{xy_\Lambda} = \frac{1}{U^2_\Lambda h_{y_\Lambda}} \frac{\partial}{\partial y_\Lambda} \int_0^x \int_0^\infty h_{x_\Lambda} u_\Lambda v_\Lambda \, dz_\Lambda dx_\Lambda \tag{9.13}$$

Fig. 9.35 shows contours of $\theta^*_{xy_\Lambda}/\theta^*_{y_\Lambda}$. As seen with the displacement thickness, the crossflow generally increases the momentum thickness in regions where the surface streamlines converge, and decreases it in regions where the surface streamlines diverge. The range in the ratio of the momentum thickness is slightly greater than with the displacement thickness. As noted with the displacement thickness, the calculation of the momentum thickness is unreliable on the suction side near the symmetry plane at the rear of the model.

Given the significant influence of the crossflow on the displacement thickness, any attempt to calculate the shape factor requires the consideration of the crossflow influence. Fig. 9.36 shows contours of a shape factor calculated from

$$H_\Lambda = \frac{\delta^*_{x_\Lambda} + \delta^*_{y_\Lambda}}{\theta^*_{x_\Lambda} + \theta^*_{xy_\Lambda}} \tag{9.14}$$

The shape factor H_Λ is around 2.4 near the front of the body ($x_{bc}/l = -0.45$). On the pressure side H_Λ slowly increases to around 2.5 at $x_{bc}/l = 0$; it continues to increase in the area where the surface streamlines diverge until shortly before the transition region where it has a value of around 2.9. On the suction side H_Λ increases more rapidly to about 2.6 before the start of the transition region. H_Λ drops to around 1.5 shortly after transition and gradually increases to approximately 1.7 just upstream of where the boundary layer separates. The increase in H_Λ seen on the suction side near the symmetry plane just prior to boundary layer separation is due to the difficulty in calculating the displacement and momentum thickness in this region.

One of the advantages of the correlation-based transition prediction method used by Menter et al. [92] is that it uses the vorticity or strain rate Reynolds number and does not require the calculation of a momentum thickness. The momentum thickness is not readily available in finite volume codes but the vorticity and strain rate Reynolds number may be calculated from local variables. The present study does not examine the prediction of boundary layer transition; but given that calculation of the boundary layer parameters has already been performed, the opportunity is taken to compare the calculated momentum thickness with the maximum vorticity and maximum strain rate Reynolds numbers, Re_Ω and Re_S respectively. These Reynolds numbers are determined from the maximum vorticity, Ω_{max}, and maximum stain rate, S_{max},

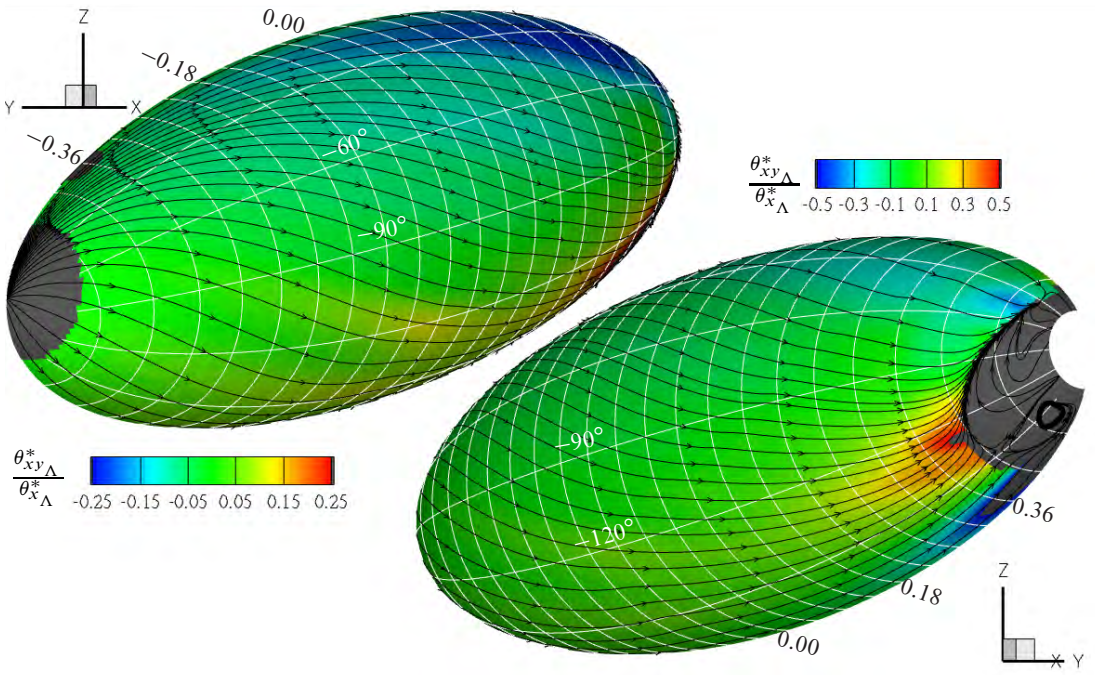

Figure 9.35: Contours of $\theta^*_{xy_\Lambda}/\theta^*_{x_\Lambda}$, $\alpha = -10.2°$, $Re_l = 4.0 \times 10^6$, realisable k-ε turbulence model with measured laminar region implemented. The contours have been limited in order to show greater resolution over the majority of the model. As seen with the ratio of crossflow and streamwise displacement thickness, the crossflow generally results in increased momentum thickness in the region where the surface streamlines (black) are converging and a dispersion of fluid from the boundary layer in regions where they diverge. The range in the ratio of the momentum thickness is slightly greater than with the displacement thickness.

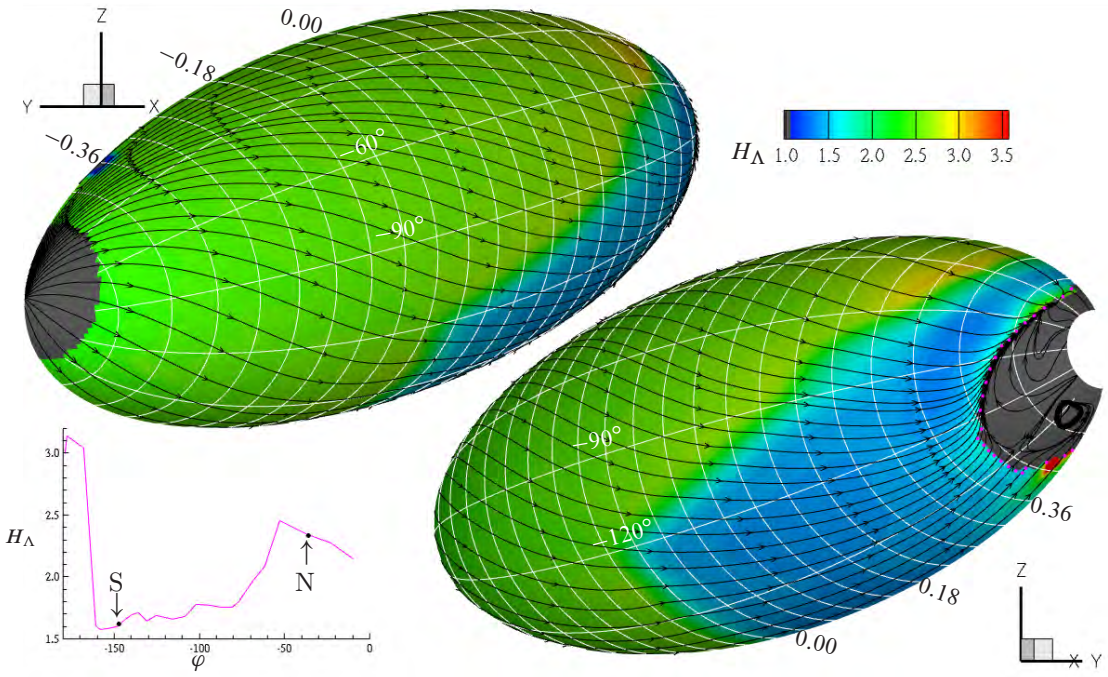

Figure 9.36: Contours of the streamwise shape factor, H_Λ, calculated allowing for the influence of crossflow on the displacement and momentum thickness for the spheroid at $\alpha = -10.2°$, $Re_l = 4.0 \times 10^6$ using the realisable k-ε turbulence model with measured laminar region implemented. The shape factor is around 2.4 at $x_{bc}/l = -0.45$ and increases to about 2.6 on the flank and suction side prior to boundary layer transition. The circumferential average value of H_Λ on the separation line is comparable to that of a two-dimensional turbulent boundary layer with significant excursions above and below this value. The insert x-y plot shows H_Λ as close as possible to the separation line (see magenta dots on contour plot). S denotes the saddle, N the node, with the foci not shown.

in the boundary layer normal to the surface.

$$Re_{\Omega} = \frac{y_P^2\ \Omega_{max}}{\nu} \qquad Re_S = \frac{y_P^2\ S_{max}}{\nu} \tag{9.15}$$

A comparison of these values is shown in Fig. 9.37 for the spheroid at $\alpha = -10.2°$, $Re_l = 4.0 \times 10^6$ using the realisable k-ε turbulence model with measured laminar region implemented. In Figs. 9.37 and 9.38 the values are compared with the streamwise components of the momentum thickness and the shape factor, H calculated from $\delta^*_{x_\Lambda}/\theta_{x_\Lambda}$. Values shown in Fig. 9.37 to 9.39 are restricted to regions with laminar flow.

The momentum thickness Reynolds number considering only streamwise components, $Re_{\theta x_\Lambda}$, and the one allowing for the influence of the crossflow, Re_{θ_Λ}, are given by

$$Re_{\theta x_\Lambda} = \frac{U_\infty\ \theta_{x_\Lambda}}{\nu} \qquad Re_{\theta_\Lambda} = \frac{U_\infty\ (\theta_{x_\Lambda} + \theta_{xy_\Lambda})}{\nu} \tag{9.16}$$

The curves of Re_Ω and Re_S in Fig. 9.37 are essentially identical. The relationship

$$Re_\theta = \frac{Re_\Omega}{2.193} \tag{9.17}$$

used in the correlation-based transition model [92] in this case appears to initially under-predict $Re_{\theta x_\Lambda}$ by around 100 near the start of the model and over-predict by a similar amount prior to boundary layer transition. As shown in Fig. 9.38(a) this results in the largest deviation from Eq. 9.17 near the front of the model. Given that the shape factor was around 2.4, this deviation appears in the scatter plot of $Re_\Omega/(2.193\ Re_\theta)$ against H (Fig. 9.38(b)) as a wedge of points less than 0.9 near $H = 2.4$. Given the favourable pressure gradient and the low values of Re_Ω in this region, this is probably of minimal concern to the correlation-based transition model. Fig. 9.39 shows Eq. 9.17 is less applicable if the momentum thickness allows for the influence of crossflow; however, there is a tighter correlation of $Re_\Omega/Re_{\theta x_\Lambda}$ and H_Λ. An approximately parabolic relationship exists between $Re_\Omega/Re_{\theta x_\Lambda}$ and H_Λ, a second-order polynomial was fitted to the data in Fig. 9.39 (b), giving

$$Re_\Omega/(2.193\ Re_{\theta_\Lambda}) = -10.51 + 7.679\ H_\Lambda - 1.222\ H_\Lambda^2 \tag{9.18}$$

9.3.5 Drag Components

Although no drag measurements are available for comparison, it is worth noting the computed breakdown between form and viscous drag. The calculated C_D based on the maximum cross-

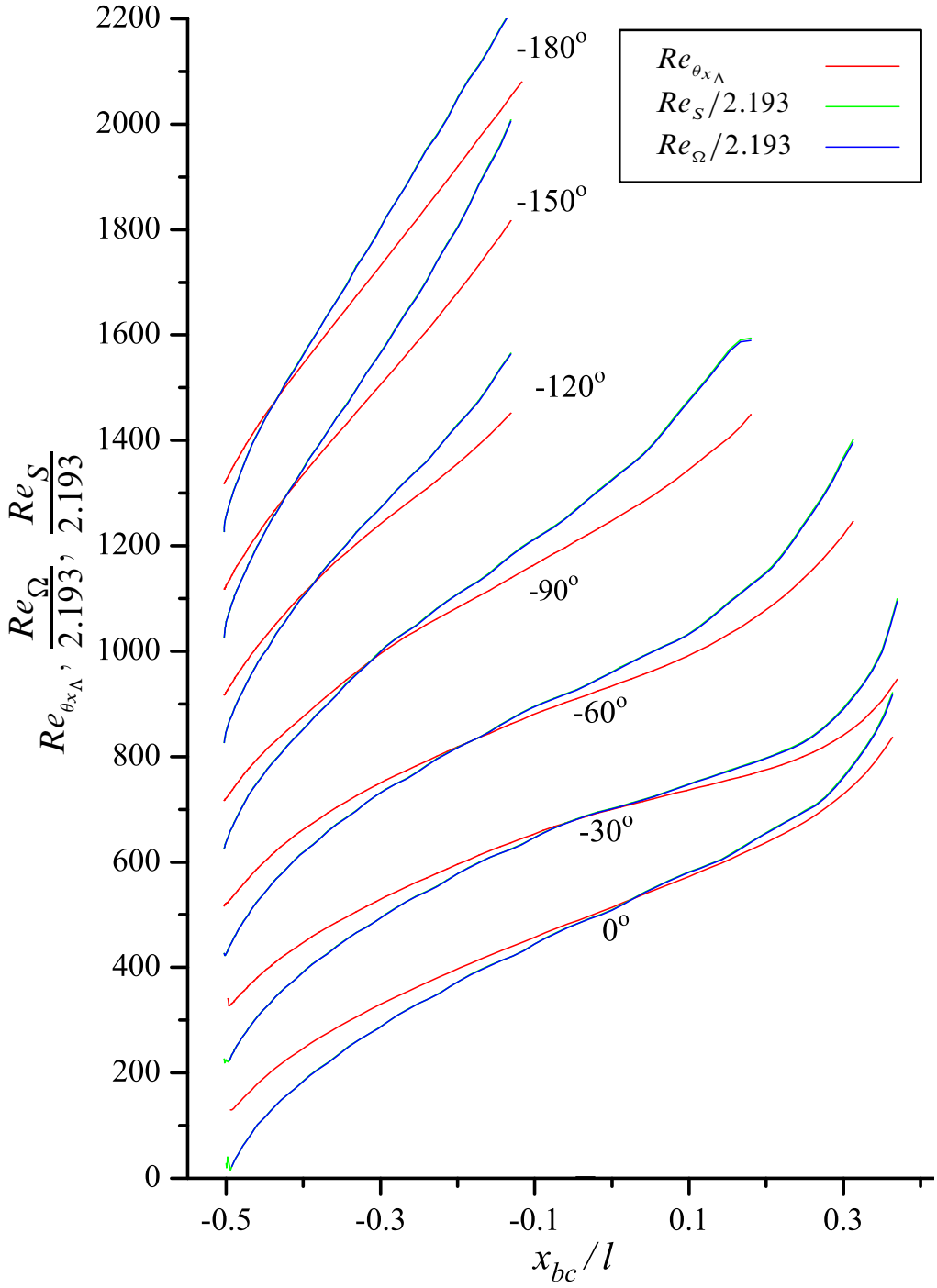

Figure 9.37: Comparison of calculated Reynolds numbers based on streamwise momentum thickness and, maximum vorticity and strain rate normal to the surface in the boundary layer on the spheroid, $\alpha = -10.2°$, realisable k-ε turbulence model with laminar boundary layer region implemented. Results for each azimuth progressively displaced by 200 for $\varphi < 0°$ and restricted to regions of laminar flow. Note the minimal difference between Re_Ω and Re_S curves.

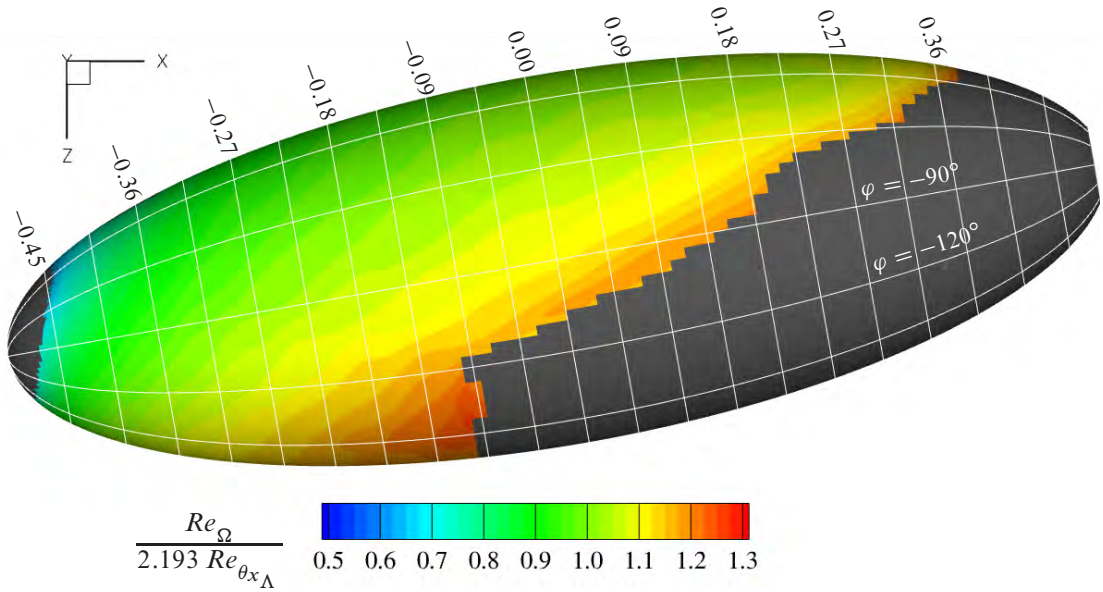

(a) Contours of $Re_\Omega/(2.193\ Re_{\theta x_\Lambda})$ showing the greatest deviation from Eq. 9.17 occurs on the pressure side near the front of the model.

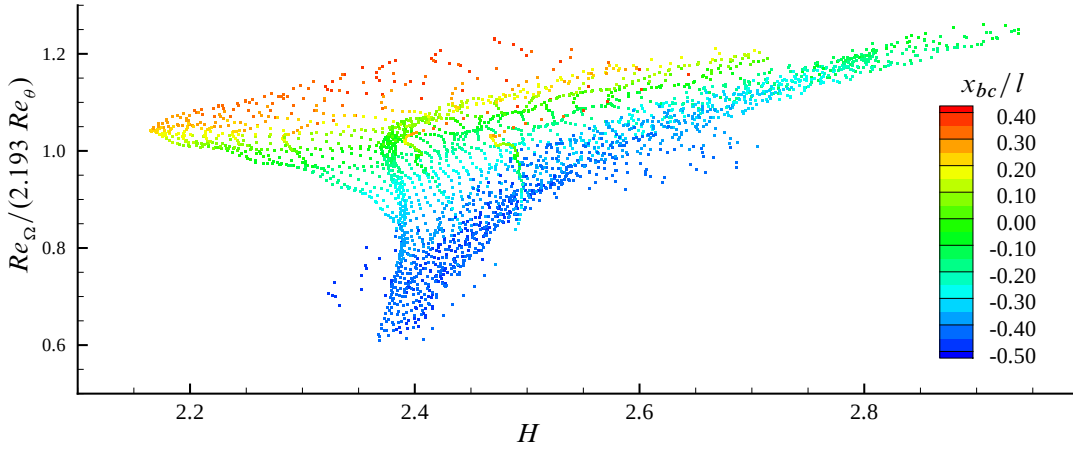

(b) $Re_\Omega/(2.193\ Re_{\theta x_\Lambda})$ against H showing the greatest deviation from Eq. 9.17 occurs when $H \approx 2.4$ near the front of the spheroid. Colour of points shows position in body coordinates.

Figure 9.38: Calculated boundary layer properties considering only the streamwise component for the spheroid at $\alpha = -10.2°$, $Re_l = 4.0 \times 10^6$, *Sph_Grid-10A*, using the realisable k-ε turbulence model with laminar regions implemented from boundary layer survey. Values shown restricted to regions of laminar flow

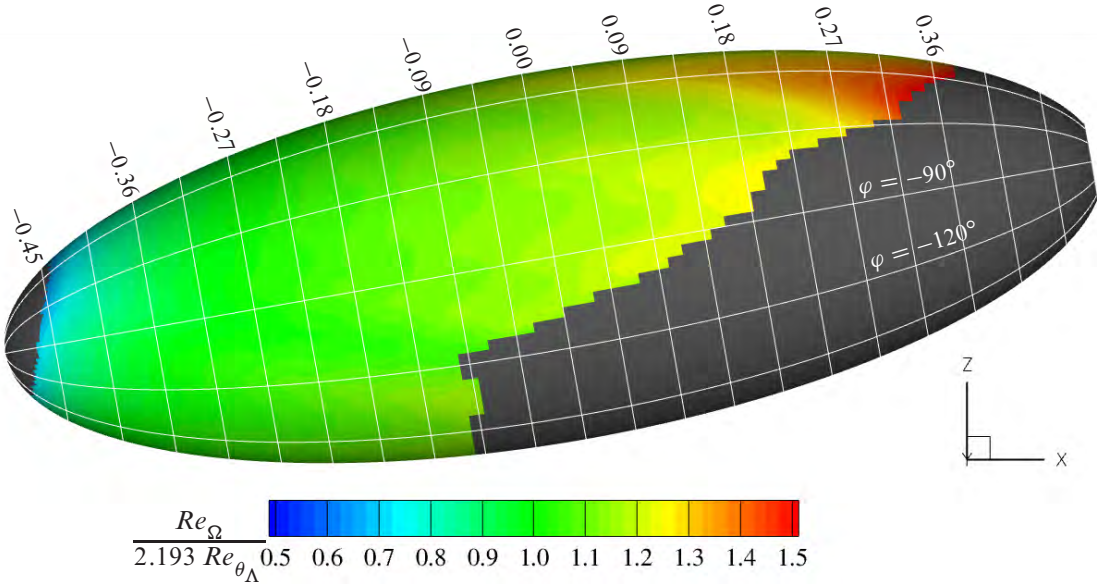

(a) Contours of $\boldsymbol{Re}_\Omega/(2.193\ \boldsymbol{Re}_{\theta_\Lambda})$ showing a greater deviation from Eq. 9.17 than that seen in Fig. 9.38

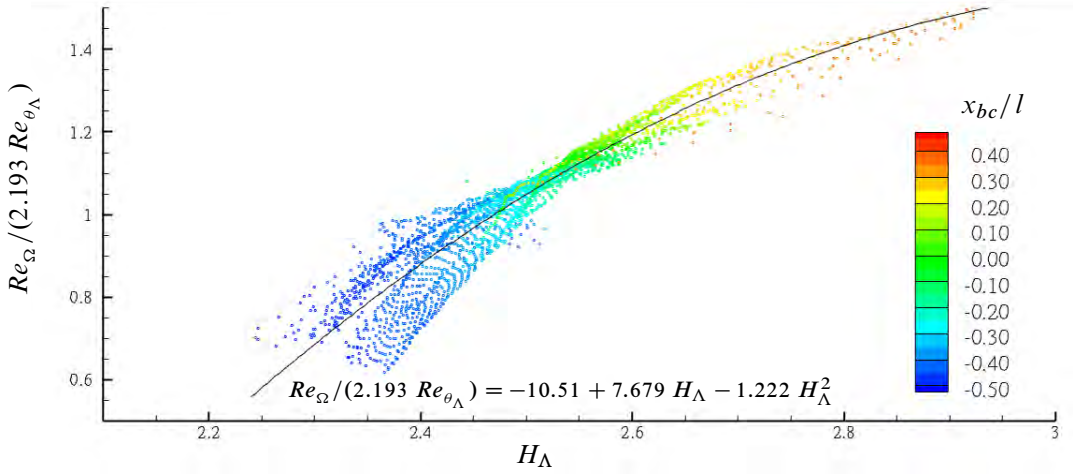

(b) An approximately parabolic relationship exists between $\boldsymbol{Re}_\Omega/\boldsymbol{Re}_{\theta_{x_\Lambda}}$ and $\boldsymbol{H}_\Lambda$, this relationship shows a dependency on x_{bc}/l. Colour of points shows position in body coordinates. A linear least squares fitting technique was used to fit a second order polynomial.

Figure 9.39: Calculated boundary layer properties allowing for crossflow on the spheroid at $\alpha = -10.2°$, $Re_l = 4.0 \times 10^6$, *Sph_Grid-10A*, using the realisable k-ε turbulence model with laminar regions implemented from boundary layer survey. Values shown restricted to regions of laminar flow

Turbulence Model	Form	Viscous	Total
realisable k-ε	0.0240	0.0361	0.0601
SST	0.0282	0.0340	0.0622
realisable k-ε with laminar region	0.0150	0.0155	0.0306
SST with laminar region	0.0298	0.0134	0.0434

Table 9.3: Calculated Drag Coefficients for $\alpha = -10.2°$, $Re_l = 4.0 \times 10^6$.

section perpendicular to x_{bc} is given in Table 9.3. The values in this table demonstrate the necessity of implementing the correct boundary layer regime if the drag is to be accurately calculated on a body where no one boundary layer type dominates. An artificially long region of turbulent flow will increase the viscous drag, due to the greater skin friction associated with turbulent flow, and also increase the form drag as the faster boundary layer growth results in a thicker boundary layer that will separate earlier. The premature separation of the boundary layer on the suction side when using the SST turbulence model with the laminar region implemented results in a larger form drag compared with the equivalent case with the realisable k-ε model. Even though only a small decrease in the area of separated flow near the rear of the model was noted when the laminar region was implemented using the realisable k-ε model, the predicted form drag is reduced by 40% in this case. The total drag predicted by the realisable k-ε model is roughly doubled if the observed transition behaviour is not prescribed.

9.4 Results and Discussions $\alpha = -10.2°$, Boundary Layer Tripped

The laminar region was implemented over the upstream 20% of the model, corresponding to the placement of the trip strip at $x_{bc}/l = -0.3$. The computed results, as expected, are similar to those observed at this incidence with no laminar region implemented as seen by comparing the surface streamlines in Figs. 9.30 and 9.40. As seen throughout these computations the realisable k-ε turbulence model predicts a greater surface shear stress than the SST turbulence model. In previous cases where boundary layer transition was determined from the measured transition without a boundary layer trip the slower switch on of the SST model resulted in laminar boundary layer separation, without reattachment, on some portions of the surface. In this case the slower switch on of the SST model should have minimal impact on the result as the turbulent boundary layer is established well before the laminar boundary layer would separate. Fig. 9.40 shows that on the pressure side both models predict a similar location for

turbulent boundary layer separation, which matches that obtained from the flow visualisation. On the flank, however, both models under predict the size of the separation. Kreplin and Stäger [23] caution that isotropic turbulence models will not faithfully replicate flow conditions around a inclined 6-1 spheroid. Mindful of this caution a case was solved using the Reynolds Stress Model (RSM). This turbulence model solves the six Reynolds stress transport equations, but requires modelling of the turbulent diffusion, pressure strain and dissipation terms. The dissipation was modelled using the same equation as used with the realisable k-ε turbulence model. The laminar region was implemented by setting the Reynolds stresses to zero in the laminar regions. The surface shear stress calculated using this RSM was close to that seen with the realisable k-ε model; the surface streamlines showed a similar under prediction in the size of the separated region.

The comparison of measured and predicted C_p distributions in Fig. 9.41 shows minimal difference between the calculated distributions for any of the turbulence models over the upstream 80% of the spheroid length. Prior to transition there is a close match between the measured and calculated surface C_p distributions, with the exception of some measured points for $Re_l = 4.0 \times 10^6$ when $\varphi = 0°$ and $-180°$ where the boundary layer has transitioned prior to the trip strip. For 60% of the spheroid's length after boundary layer transition, the measured C_p is consistently slightly greater than the calculated values.

For all the calculations presented, the increase in C_p seen in the measurements after boundary layer transition has not been apparent, with one possible exception; at $\alpha = -10.2°$, $Re_l = 2.0 \times 10^6$ where the axisymmetric boundary layer was implemented. (It is difficult to determine here if C_p has had a positive shift downstream of the boundary layer transition due to the surface curvature and the short length of turbulent boundary layer before the end of the model.) This case with the tripped boundary layer provides the clearest observation of this phenomenon, as the location of transition is constant for all azimuths and there is a significant length of surface downstream of the transition region with minimal surface curvature. It is difficult to see how the start of a turbulent boundary layer could cause any systematic error in the measurements of the (average) surface C_p distribution, but the following possibilities were considered:

- For the same Reynolds number a turbulent boundary layer has greater velocity flow close to the surface than a laminar boundary layer. Hence static pressure measurement errors are likely to be greater for a turbulent boundary layer than for a laminar boundary layer (ignoring the possibility that the pressure tapping hole may trip the boundary layer). If this were the case, however, a variation in the magnitude of this influence would be expected with Reynolds number and boundary layer thickness; such variation is not seen

in the measurements.

- Surface pressure fluctuations will be greater in a turbulent boundary layer. Willmarth [107] suggests the RMS surface pressure fluctuations should be in the order of six times greater than the mean wall shear stress; this gives $C_{\sqrt{\overline{p'^2}}} \approx 0.02$ for turbulent regions from Fig. 9.31. Much of the energy associated with these pressure fluctuations is dissipated due the elasticity of the tubing connecting the tapping and the transducer. This loss in energy results in less movement of the diaphragm in the transducer used to measure the pressure, but it should not change its average position and thus not the mean pressure measurement.

- The pressure normal to the wall in a turbulent plane flow at high Reynolds numbers, assuming negligible turbulence in the freestream, is approximated by [108]

$$\overline{p} + \rho\overline{v'^2} = \overline{p}_w = p_e \tag{9.19}$$

  where $\overline{p}_w$ is the average static pressure at the wall and p_e is the static pressure at the edge of the boundary layer. From Eq. 9.19 it is apparent that the pressure across a turbulent boundary layer with plane flow is not constant. However, as long as $\overline{v'^2} = 0$ at the tapping the normal component of the turbulent velocity should not influence the mean static pressure there.

- If hysteresis in the sensor were a problem, the extra movement of the diaphragm when measuring a turbulent boundary layer may result in a difference between the pressures measured in a laminar or turbulent boundary layer. This possibility is considered unlikely as the pressure ranges, mean and unsteady, vary considerably across the range of position and Reynolds number yet the shift in the measured values between laminar and turbulent boundary layer appears consistent.

Another factor to recall is that a positive shift in the C_p distribution was observed downstream of boundary layer transition in calculations of the flow modelled about a two-dimensional elliptical cylinder using X-foil and Fluent (Fig. 9.12).

The turbulence models shown in Fig. 9.41 over predict the base pressure. However the SST model does so to a lesser extent for some azimuths. When this occurs there appears to be a slightly closer correlation with the measured surface C_p distribution over the last 20% of the spheroid's length. One possibility is that incorrect calculation of the base pressure is influencing the pressure upstream, so that downstream of the perturbation caused by boundary layer transition the curves for the turbulent boundary layer do not display the shift in C_p seen in the measurements and the two-dimensional calculations.

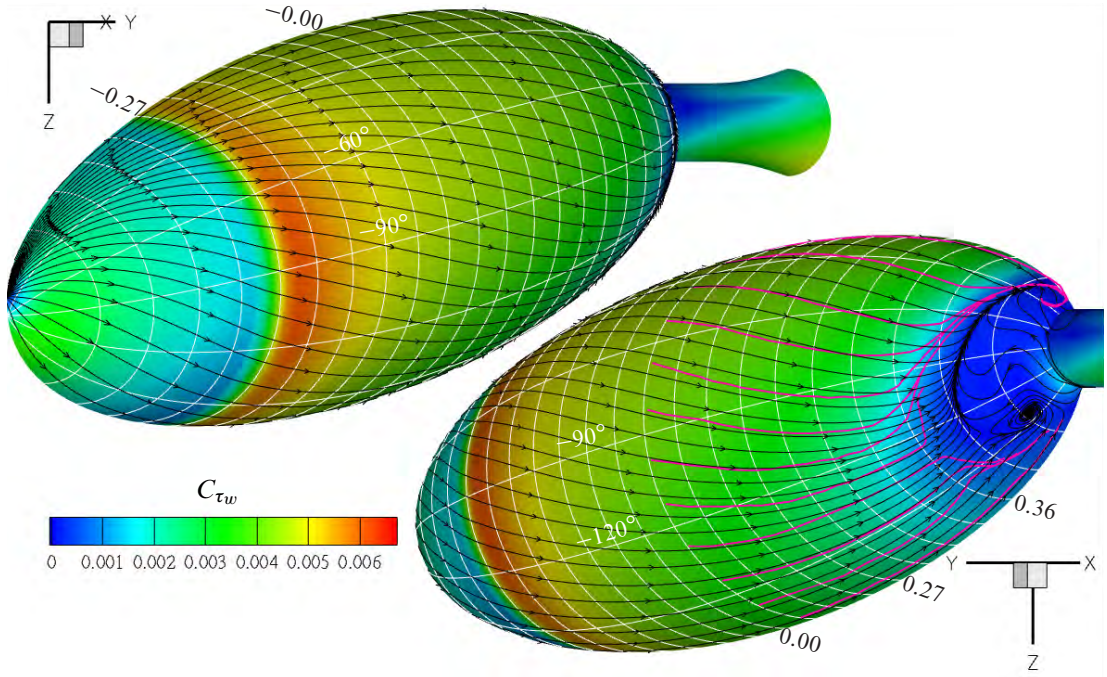

(a) Calculations with realisable k-ε turbulence model underpredict the region of separated flow, though the surface streamlines have a similar pattern.

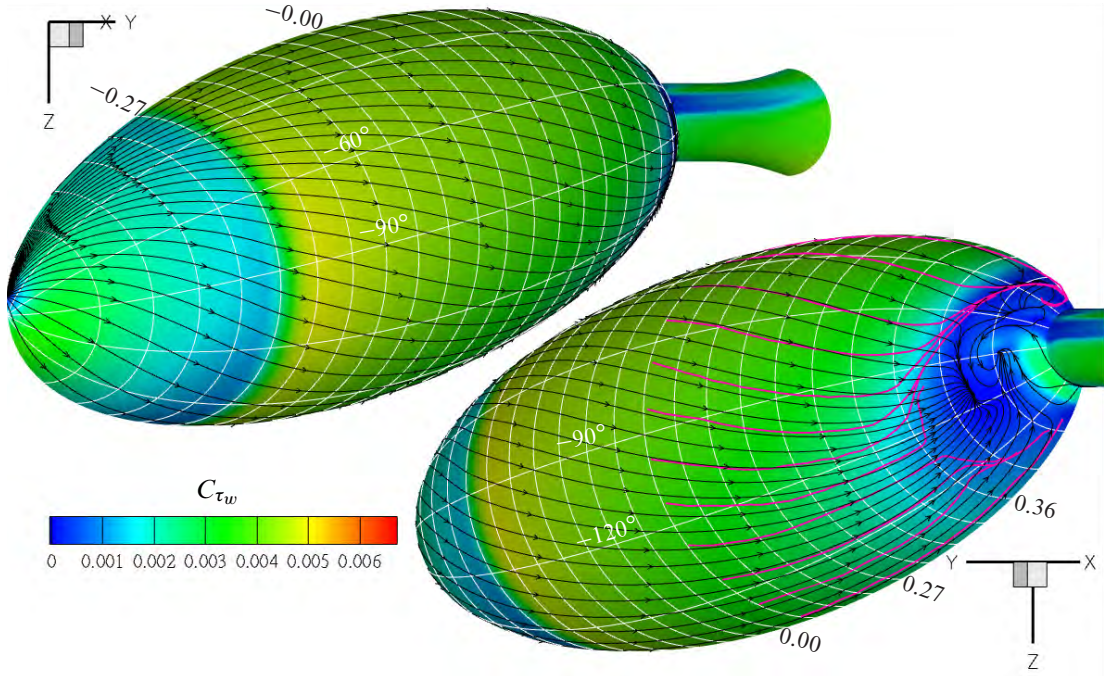

(b) Calculations with SST turbulence model underpredict the region of separated flow.

Figure 9.40: Surface streamlines and contours of C_{τ_w} for spheroid at $-10°$ incidence with tripped boundary layer at $x_{bc}/l = -0.3$. Surface streamlines from flow visualisation shown in magenta; calculated surface streamlines in black.

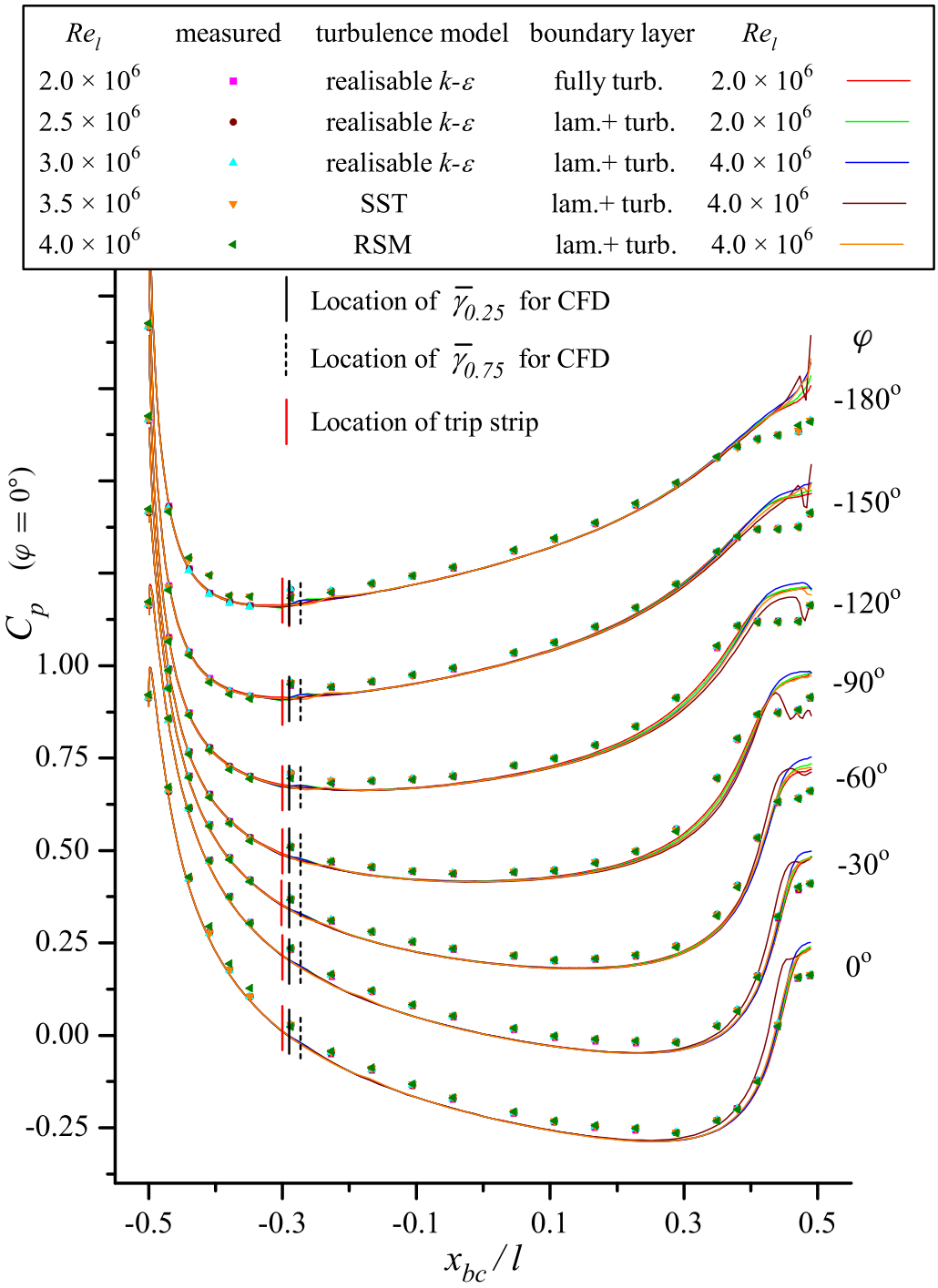

Figure 9.41: Computed and measured surface pressure distribution on spheroid with trip strip at $x_{bc}/l = -0.3$, $\alpha = -10.2°$. C_p values for each azimuth progressively displaced by 0.25 for $\varphi < 0°$. There is little difference between the calculated surface C_p distribution for any of the turbulence models, all models over predicting the base pressure. Prior to transition there is generally a close match between the measured and calculated surface C_p distribution with the exception of some measured points for $Re_l = 4.0 \times 10^6$. For 60% of the spheroid's length after boundary layer transition the measured C_p is consistently slightly greater than the calculated values.

A comparison of measured and calculated force and moment coefficients is shown in Fig. 9.42. The drag coefficient, C_D, calculated using the two-equation turbulence models shows the same trend with Reynolds number as the measured data. The values of C_D determined using the realisable k-ε and SST turbulence model were respectively 20% and 25% greater than the measured values. The region of separated flow observed in the flow visualisation was greater than that in the computed results; this observation is supported by lower pressure recovery in the surface pressure measurements than in the computed results. These factors indicate that the form drag will be under estimated by these calculations; this will in all likelihood create a greater disparity between the calculated and measured drag. In calculations with the tripped boundary layer, the form drag contributes approximately 40% of the total drag. The component of lift and moment directly due to the surface shear stress is negligible.

The magnitude of the lift coefficient, C_L, calculated using the realisable k-ε model was about 25% smaller than measured, while the results from the SST model were within the range of measured values. The measured and calculated values of moment coefficient, $C_{T_{y_{bc}}}$, from the two-equation turbulence models were close to the measured values. The calculated and measured values of this moment coefficient are expected to be close, as this load is dominated by the Munk moment. The values calculated for all coefficients using the RSM model at $Re_l = 4.0 \times 10^6$ were between the values calculated from realisable k-ε and SST models.

9.5 Summary

The method used to implement the laminar regions had limited success with the SST turbulence model when using the location of boundary layer transition determined from the measurements without artificial tripping. The increased surface shear associated with the development of the turbulent boundary layer did not occur until some distance downstream of the predefined boundary layer transition zone. Fig. 9.24(a) shows the SST model switching on approximately 5% of the spheroid's length later than the realisable k-ε turbulence model. In many instances this resulted in a laminar separation on some part of the body. The studies with the SST model demonstrated the importance of correctly modelling the position and length of the transition region. At $Re_l = 2.0 \times 10^6$ using the realisable k-ε turbulence model the direct application of the measured transition region also had problems with laminar separation. It was, however, possible to get apparently more reasonable results with some minor modifications to the transition region and increased mesh resolution in the regions of laminar separation. In the case of the spheroid at:

- $\alpha = -0.2°$ this involved modifying the transition zone so it was axisymmetric, where the measured location of transition showed some variation (up to 4% of the spheroid's length) in the streamwise location of boundary layer transition.

- $\alpha = -10.2°$ this involved shifting the transition zone upstream by approximately $x_{bc}/l = 0.05$ for φ between 0° and −30° in order to avoid a laminar separation.

This tailoring is far from ideal and shows a lack of robustness when dealing with separation of the laminar boundary layer. The calculated separation bubble apparent at $\alpha = -0.2°$, $Re_l = 2.0 \times 10^6$ in Fig. 9.19 occurs at the start of the transition zone, $\bar{\gamma} \lessapprox 0.4$. Perturbations in the surface streamlines were observed during on-body flow visualisation at the lower Reynolds numbers, these were believed to be associated with boundary layer transition. Similar, though sharper, perturbations were also apparent in the surface streamlines calculated from the surface shear stress in the region where boundary layer transition was implemented for $Re_l = 2.0 \times 10^6$. Both the calculated separation bubble at the start of the transition region and the perturbations in the calculated surface streamlines show a very strong redirection of the flow in the normal and azmiuthal direction respectively near the start of transition zone. This may be exaggerated due to: too short a length of boundary layer transition; neglecting the temporal aspect of the transition process; and/or errors in the predicted surface shear stress at the start of the transition zone. The first of these factors is not believed to be the cause, because as noted in Subsection 9.3.1 increasing the length of the transition zone made minimal change in the calculated surface streamlines; additionally, the length of the transition zone used in the calculations corresponded to that measured (except when noted). The second factor may play a role as the time averaged implementation of the transition region does not model the coherent structures that exist in intermittently and fully turbulent shear layer regions. The last of these factors may be an issue, as the realisable k-ε turbulence model showed a greater surface shear stress at the start of the transition region than the SST model. However, as noted in the previous paragraph, the slower establishment of the turbulent boundary layer with the SST model resulted in it being less suitable to this method of implementing the laminar regions as the boundary layer tended to separate without reattachment.

With and without the implementation of laminar boundary layer regions, the realisable k-ε turbulence model at $\alpha = -10.2°$, $Re_l = 4.0 \times 10^6$ resulted in good agreement between the surface flow visualisation and the calculated surface streamlines over the majority of the spheroid; the exception was the size of the separation on the rear flank being smaller than that observed in the flow visualisation. For $\alpha = -10.2°$, $Re_l = 2.0 \times 10^6$ the measured and calculated surface streamlines showed perturbations in the region of boundary layer transition that were not observed at $Re_l = 4.0 \times 10^6$.

Both turbulence models predict an attached turbulent boundary layer on the suction side near the symmetry plane extending almost the full length of the spheroid. Numerical investigation of this feature revealed that the small component of adverse pressure gradient parallel to the surface but perpendicular to the direction of flow at the boundary layer edge was removing the lower inertia fluid of this thickening boundary layer. The extended length of flow in this region was observed in the measured data, although the length of attachment was slightly less.

The change in measured C_p when the boundary layer was tripped showed a clear distinction between the measured and calculated surface pressure coefficient in the presence of a turbulent boundary layer. This difference was not apparent in the calculated surface C_p, as discussed in Subsection 9.4.

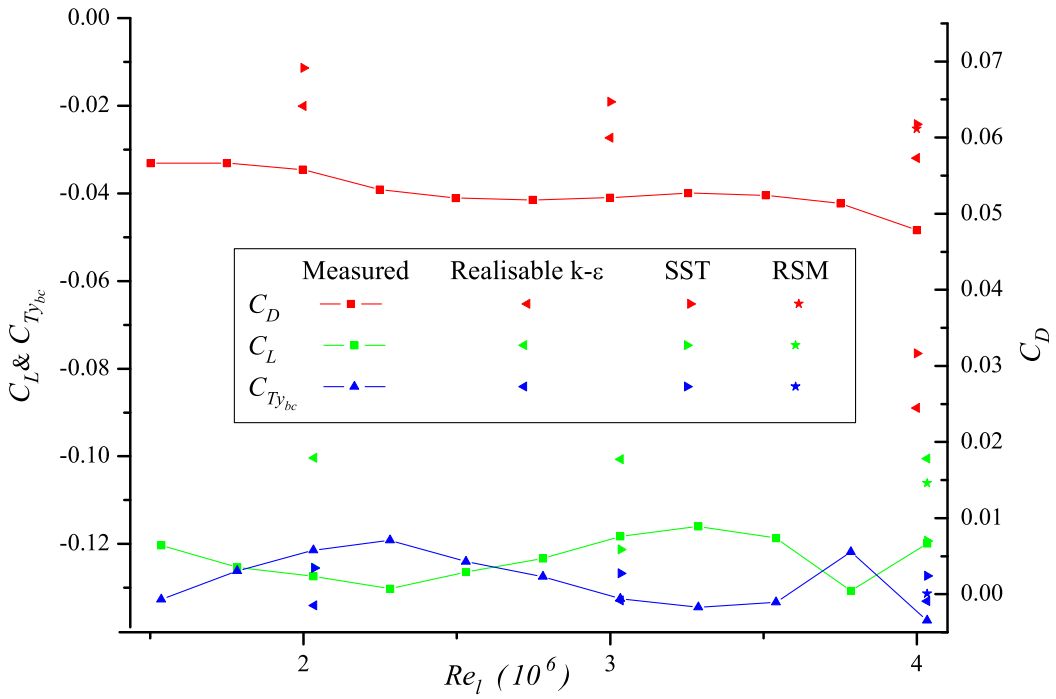

Figure 9.42: Computed and measured loads on spheroid with trip strip at $x_{bc}/l = -0.3$, $\alpha = -10.2°$. A similar trend in the measured and calculated C_D is observed.